UNIVERSITY OF CALIFORNIA,
IRVINE

Mechanical Properties of Architected Materials with Spinodal Topologies: An Experimental Investigation

DISSERTATION

submitted in partial satisfaction of the requirements
for the degree of

DOCTOR OF PHILOSOPHY

in Materials Science and Engineering

by

Yunfei Zhang

Dissertation Committee:
Professor Lorenzo Valdevit, Chair
Professor Timothy J. Rupert
Associate Professor Daniel R. Mumm

2021

DEDICATION

To

My family and friends

who have always supported me along the way no matter what happens

To

Richard Feynman and all the other great scientists in the 20th century

whose stories showed me the beauty in the pursuit of knowledge and scientific discovery

To

Wang Xiaobo

whose words I still live by:

我活在世上，无非想要明白些道理，遇见些有趣的事。倘能如我愿，我的一生就算成功。

TABLE OF CONTENTS

LIST OF FIGURES

ACKNOWLEDGEMENTS

I would like to first express my gratitude to my PhD advisor, Professor Lorenzo Valdevit, who has always guided and supported me during the past six years. His help has been essential for me to become an efficient researcher. I feel fortunate to have him as my advisor for his consistent encouragement, inspiration and patience.

I would also like to thank my committee members, Professor Tim Rupert and Professor Daniel Mumm. They have provided invaluable insight and practical suggestions to help me improve my thesis and presentation.

I would like to thank all the members of the Architected Materials Group for their help and friendship. I have learnt so much from them and it is my honor to have worked with such a wonderful group of people.

In addition, I would like to acknowledge the financial support from the Air Force Office of Scientific Research (program manager: Dr. Joycelyn Harrison, Contract No. FA9550-14-1-0352), and the Office of Naval Research (program manager: D. Shifler, Grant No. N00014-17-1-2874).

Special thanks to the Institute for Design and Manufacturing Innovation (IDMI) for additive manufacturing equipment support and the Irvine Materials Research Institute (IMRI) for material characterization resources. I'm grateful for Ben Dolan, the technical director of IDMI and Dr. Jianguo Zheng, the director of IMRI for their help which are essential in my experimental endeavors.

Finally, I would like to thank all my family and friends whose company and support made my PhD journey colorful and memorable.

CURRICULUM VITAE

Yunfei Zhang

Education

University of California, Irvine **Present**
Ph.D., Material Science and Engineering GPA: 3.7
University of California, Irvine **March 2015**
M.S., Material Science and Engineering GPA: 3.6
Zhengzhou University, China **June 2013**
B.S., Materials Science and Engineering GPA: 3.6

Research Experience

Graduate Research Assistant **January 2016- Present**
Professor Lorenzo Valdevit Lab, University of California, Irvine, CA

- Experimentally investigate mechanical properties of architected materials with spinodal topologies in the form of both composite and cellular materials
- Performed additive manufacturing and mechanical characterization in multiple research projects

Graduate Research Assistant **October 2013 - March 2015**
Professor Allon Hochbaum Lab, University of California, Irvine, CA

- Familiar with solution syntheses of Ge nanoparticles for the fabrication of high-performance thermoelectric materials and characterization of physical properties of nanoparticles
- Conducted research on surface chemistry of Ge nanoparticles for purpose of processing of thin films with good electronic properties

Undergraduate Research Assistant **September 2012 - June 2013**
Professor Guotian Ye Lab, Zhengzhou University, China

- Investigated the phase composition and microstructure of andalusite with different amounts of impurities after mechanical milling for different time and heat treatment with different temperatures
- Found the evidence of the effect of mechanical milling on lowering mullization temperature of andalusite

Publications

1. Y. Zhang, M.-T. Hsieh, B. Fields and L. Valdevit, "Topological Toughening of 3D Printed Interpenetrating Phase Composites with Shell Based Topologies," Advanced Engineering Materials (2021), in preparation.

2. Y. Zhang, M.-T. Hsieh, and L. Valdevit, "Mechanical performance of 3D printed interpenetrating phase composites with spinodal topologies," Composite Structures, vol. 263, p. 113693, May 2021, doi: 10.1016/j.compstruct.2021.113693..

3. M.-T. Hsieh, B. Endo, Y. Zhang, J. Bauer, and L. Valdevit, "The mechanical response of cellular materials with spinodal topologies," Journal of the Mechanics and Physics of Solids, vol. 125, pp. 401–419, Apr. 2019, doi: 10.1016/j.jmps.2019.01.002.

4. J. Bauer, A. G. Izard, Y. Zhang, T. Baldacchini, and L. Valdevit, "Programmable Mechanical Properties of Two-Photon Polymerized Materials: From Nanowires to Bulk," Advanced Materials Technologies, vol. 4, no. 9, p. 1900146, 2019, doi: 10.1002/admt.201900146.

5. A. E. Garcia et al., "Scalable synthesis of gyroid-inspired freestanding three-dimensional graphene architectures," Nanoscale Advances, vol. 1, no. 10, pp. 3870–3882, 2019, doi: 10.1039/C9NA00358D.

6. J. Bauer et al., “Thermal post-curing as an efficient strategy to eliminate process parameter sensitivity in the mechanical properties of two-photon polymerized materials,” Opt. Express, OE, vol. 28, no. 14, pp. 20362–20371, Jul. 2020, doi: 10.1364/OE.395986.

7. J. D. Trolinger, A. K. Dioumaev, A. K. Lal, L. Valdevit, and Y. Zhang, “In-situ monitoring and quality control for in-space additive manufacturing using laser acoustical resonance spectroscopy,” in Applied Optical Metrology III, Sep. 2019, vol. 11102, p. 1110217. doi: 10.1117/12.2529511.

ABSTRACT OF THE DISSERTATION

Mechanical Properties of Architected Materials with Spinodal Topologies: An Experimental Investigation

by

Yunfei Zhang

Doctor of Philosophy in Materials Science and Engineering

University of California, Irvine, 2021

Professor Lorenzo Valdevit, Chair

Architected materials (or metamaterials) are engineered multiphase (composite) or single-phase (cellular) materials with carefully controlled and optimized topological phase distributions, which can result in combinations of properties not normally found in nature. Over the past two decades, a wide variety of metamaterials have been developed for mechanical applications, achieving exceptional combinations of high strength and stiffness, high energy absorption and high fracture toughness. Optimal design of the topology plays an essential role in achieving exceptional mechanical properties of architected materials. Whereas traditionally the most heavily investigated designs have all been truss-based, the rapid development of additive manufacturing technologies over the past decade has spurred interest in more complex topologies, notably shell-based periodic architected materials based on triply periodic minimal surfaces (TPMS). While TPMS-based architected materials have been shown to possess combinations of high stiffness, strength, energy absorption and notably better mechanical properties than their truss-based counterparts, they are generally difficult to manufacture in a scalable fashion, thus limiting their potential applications in structural components. Shell-metamaterials with stochastic spinodal topologies (where the

smooth continuous shell is defined as the interface between two spinodally decomposed phases) have the potential of combining TPMS-like performance and exceptional scalability. In this thesis, we experimentally investigate the mechanical performance of shell-metamaterials with spinodal topologies, in the form of cellular materials, as well as in the form of reinforcement phase for composites, manufactured through both additive manufacturing and self-assembly techniques. We conclude that architected materials with spinodal shell topologies combine remarkable specific stiffness and strength, a long flat plateau after yielding, intriguing toughening mechanisms and potential for self-assembly. These results suggest that architected materials with spinodal shell topologies are excellent candidates for mechanical and multi-functional applications.

INTRODUCTION

Architected materials (or metamaterials) are engineered multiphase (composite) or single-phase (cellular) materials with carefully controlled and optimized topological phase distributions, which can result in combinations of properties not normally found in nature. For single phase cellular materials, their Young's modulus, E and yield strength σ_y, can be described as a function of the relative density, ρ (defined as the volume fraction of the solid phase), generally following a power-law behavior: $E \sim E_s \rho^n$ and $\sigma_y \sim \sigma_{ys} \rho^m$, with E_s and σ_{ys} the Young's modulus and yield strength of the constituent material, respectively. The values of the exponents n and m are strongly affected by the topology of the unit cell architecture and have a dramatic effect on the mechanical efficiency of the material [1]. For truss-based lattice cellular materials, a scaling $E \sim \bar{\rho}^1$ and $\sigma_y \sim \bar{\rho}^1$ denote mechanically efficient stretching-dominated behavior, with $E \sim \bar{\rho}^2$ and $\sigma_y \sim \bar{\rho}^{1.5}$ indicating less efficient bending-dominated behavior [1], [2].

As effective properties depend on both topology and constituent material properties, the ideal route to improve the mechanical performance of architected materials is to combine optimized topologies with excellent constituent material properties, which can be achieved through nano-manufacturing: by reducing the relevant topological dimensions to the nanoscale, we can take advantage of size effects on strength that both metallic and ceramic materials are known to exhibit [3]. Over the past decade, excellent combination of properties has been demonstrated in a wide range of nano-architected materials, including solid ceramic nanolattices [4], hollow metallic [5] and ceramic [6] micro and nano-lattices and nano-shell-based cellular materials [7], [8]. However, the scalability issues related to their manufacturing process greatly hindered their commercial

applications. One possible solution to this scalability issues is to utilize a mechanically efficient topology that can be manufactured through self-assembly. For example, spinodal shell topologies, defined as the interface between two spinodally decomposed phases, could be a potential candidate. To explore this opportunity, we first experimentally investigated the mechanical properties of microscale spinodal topologies manufactured through an additive manufacturing technique, two-photon polymerization direct laser writing (TPP-DLW), and demonstrated that metamaterials based on these topologies are exceptionally efficient in terms of mechanical properties. Initial findings on the mechanical properties of the acrylate-based resin, IP-Dip, used in TPP-DLW are expanded into a systematic study to establish the correlation between mechanical properties of the resin and processing parameters of the printing process. Subsequently, we mechanically investigated macroscopic samples with spinodal shell microstructure manufactured through self-assembly, showing the potential of spinodal shell topologies for self-assembly manufacturing.

For multiphase architected materials (composites), one class that has drawn great research interest is interpenetrating phase composites (IPCs). IPCs are bi-material solids composed of two phases that are topologically interconnected throughout the microstructure [9], in such a way that each phase is independently self-supporting and load-bearing. Multiple studies, both numerical [10]–[18] and experimental [19]–[26], have consistently demonstrated that the combination of reinforcement and matrix in such a way that both phases are independently self-supporting and load-bearing results in improved mechanical properties compared to traditional discontinuously reinforced composite materials as the topological interconnectivity allows each constituent phase to contribute its most desirable properties to the overall properties of the composite. The synergistic role of two phases can be engineered to result in intriguing combinations of properties.

As a few examples, (i) in Al_2O_3/Al IPCs, the stiffness of the composite was shown to be superior than that of Al, while its toughness and structural integrity were superior than that of monolithic Al_2O_3 [27]; (ii) while traditional aluminum foams undergo irrecoverable plastic deformation throughout their stress plateau, aluminum foam–polyurethane IPCs display extensive recoverable deformation under cyclic loadings, thanks to the stabilizing effect of the soft elastomeric phase [25]; (iii) metal-polymer interpenetrating phase nanocomposites based on Ti nanoporous can be tuned to match the elastic modulus of human bones, showing great potential for implant applications [26]; (iv) finally, molecular dynamics simulations have indicated that silicon carbide–aluminum IPCs display unique toughening mechanisms [18]. All these studies have consistently shown that IPCs are promising candidates for structural and multi-functional applications. It is worth noting that the vast majority of IPCs in these studies are manufactured through conventional methods, such as powder metallurgy [20] and infiltration processes [21], [28]. While efficient and generally scalable, these approaches randomly distribute controlled amounts of the two phases, and do not allow full topological control of the composite architecture.

Recent advancements in additive manufacturing have enabled fabrication of architected materials and structures with unprecedented topological complexity [29]–[31]. Notable examples that have been recently extensively investigated are shell-based periodic architected materials based on triply periodic minimal surfaces (TPMS). These cellular materials consist of the periodic repetition in three dimensions of a mathematically defined unit cell, where the constituent material is arranged as a curved smooth shell with approximately zero mean curvature everywhere. Examples of TPMS include the Schwarz P surface, the Schwarz D surface and the gyroid surface [32]. Architected materials based on TPMS have been shown to be mechanically efficient compared to truss-based architected materials, by virtue of their smooth and regular topology, resulting in low

local stress concentrations and hence efficient load transfer [26] ,[34]. Recent studies have shown that similar benefits in mechanical properties extend to TPMS-based IPCs, where either the interface between the two solid phases is a TPMS or the reinforcement phase is a thickened TPMS shell structure, embedded in a softer matrix. In particular, excellent combinations of high stiffness, strength and energy absorption have been demonstrated [35]–[38], and TPMS-based IPCs have been shown to possess better mechanical properties than their truss-based counterparts [37]. In addition, TPMS-based IPCs have been shown to possess multifunctional extrema [39], [40]. However, due to the periodic nature of TPMS, all TPMS-based IPCs are generally difficult to manufacture in a scalable fashion, thus limiting their potential applications. Far better scalability can be achieved by incorporating a stochastic reinforcement phase that can be self-assembled through spinodal decomposition of two materials followed by material conversion. Therefore, it is worth investigating mechanical properties IPCs with spinodal shell reinforcement.

In the subsequent three chapters, we will address the issues mentioned above, by presenting and discussing the results from our studies as follows:

- *Chapter 1. Mechanical performance of micro/nano-architected materials with spinodal topologies*. Experimentally investigating the mechanical performance of cellular materials with spinodal topologies, manufactured both by additive manufacturing and self-assembly.
- *Chapter 2. Mechanical performance of interpenetrating phase composites (IPCs) with spinodal topologies.* Experimentally investigating the mechanical performance of IPCs with spinodal reinforcement topologies and comparing it with that of other well-known regular reinforcement topologies.

- *Chapter 3. Fracture toughness of IPCs based on spinodal shell topologies*. Experimentally investigating the fracture toughness of IPCs with spinodal shell reinforcement topologies and comparing it with other periodic shell-based topologies.

Chapter 1 Mechanical performance of micro/nano-architected materials with spinodal topologies

1.1 Introduction

Spinodal decomposition is a thermodynamic transformation where a homogeneous (solid or liquid) solution separates spontaneously into two coexisting phases [41]. The result is an interpenetrating phase composite with very large interfacial area between the phases, and hence a characteristic length scale (domain size) much smaller than the sample size; while thermodynamics tends to reduce the interfacial area between the two phases (hence increasing the characteristic length scale), this growth can be arrested by reducing the temperature of the system (in the case of solid phases) [42] or by jamming the interface with particles that are immiscible in both phases (in the case of liquid phases) [43], [44]. A number of materials conversion techniques can be subsequently used to (i) eliminate one of the phases and converting the remaining phase to the desired material (hence producing a cellular material with spinodal solid topology) [45], (ii) converting both phases to the desired materials (resulting in an IPC with spinodal solid topology) [46], [47], or (iii) eliminating one phase, coating the other phase with the desired material and finally eliminate the second phase as well (resulting in a cellular material with spinodal shell topology) [44]. In all cases, the inherent self-assembly of spinodal topologies provides a route to fabricate micro- or nano-architected materials with macroscopic dimensions, with a level of scalability unmatched by any additive manufacturing technique [48], [49]. However, the stochastic nature of the spinodal shell topology might raise question about its mechanical performance.

Two-photon polymerization direct laser writing (TPP-DLW) is the most promising technology for additive manufacturing of geometrically complex parts with nanoscale features [50]–[52]. This makes it the ideal manufacturing technique for producing micro-scale spinodal topologies with

complex and well-defined thin shell structures which is essential in understanding the mechanical response of spinodal-shell metamaterials. As an effort to verify the simulation results in a largely computational study [53], we fabricated cellular structure samples with solid and shell spinodal topologies using TPP-DLW and tested them in uniaxial compression. Initial findings of the mechanical properties of the acrylate-based resin IP-Dip used in TPP-DLW are expanded into a systematic study to establish the correlation between mechanical properties of the resin and processing parameters of the printing process [54], [55].

Finally, as part of a recent collaboration, we investigated the mechanical properties of macroscopic samples with spinodal shell microstructure manufactured through the scalable bicontinuous interfacially jammed emulsion gels (bijels) method [49]. The results further highlight the great potential for mechanical and multifunction application of spinodal shell topologies manufactured via self-assembly.

1.2 Two-photon polymerization Direct Laser Writing (TPP-DLW)

Two-photon polymerization direct laser writing (TPP-DLW) is one of the most relevant additive manufacturing technologies to synthesize three-dimensional (3D) parts with sub-micrometer resolution [50]–[52]. TPP locally cures a photosensitive material by simultaneous absorption of two or multiple photons, using a focused ultrafast pulsed laser beam [51]. Polymerization is confined to only the ellipsoid-shaped focal point volume of the laser beam. Dimensions of this volume element, or voxel, can be below 100 nm, while typical widths and heights are in the range of ≥200 nm and ≥600 nm, respectively. Most TPP-printed structures are patterned from voxel-lines, i.e. continua of voxels, using galvanometric mirror scanning, 3-axis stage motion, or a combination of both.

With the ability to manufacture complex samples with nanoscale resolution, TPP-DLW is getting increasing research interest. Some of the most prominent research fields accelerated by TPP are photonic and mechanical metamaterials [56]–[58], micro-actuators [59], [60], microrobots [61], [62], bioscience [63]–[65], and biomimetics [66]–[68]. Micro-optical elements on fiber-tips [69]–[71], and chip-to-chip interconnects [72], [73], may soon become the first industrial applications.

1.3 Mechanical characterization of acrylate resins for TPP-DLW

While TPP technology is rapidly progressing, fabrication is still largely empirical, hindered by the lack of systematic data on material properties (e.g., strength and stiffness), and limited knowledge on their dependence on the process parameters. A small number of studies have reported certain properties of two-photon polymerized materials [74]–[78]. However, most studies were specific to particular, application-relevant specimen geometries and sizes, with limited general implication on the establishment of TPP processing-structure–properties relations. This includes the preliminary study we performed on the mechanical properties of acrylate-based resin IP-Dip, used in the TPP-DLW system Nanoscribe Photonics GT Professional to manufacture microscale spinodal topologies [53]. The results are shown in Fig 1. The preliminary results seem to suggest a size effect, with stiffness and strength increasing with decreasing pillar diameter. This size effect stops once the pillar diameter falls below a certain threshold. This interesting preliminary finding inspired us to perform a systematic characterization of the mechanical properties of the two-photon polymerized acrylate-based resin IP-Dip.

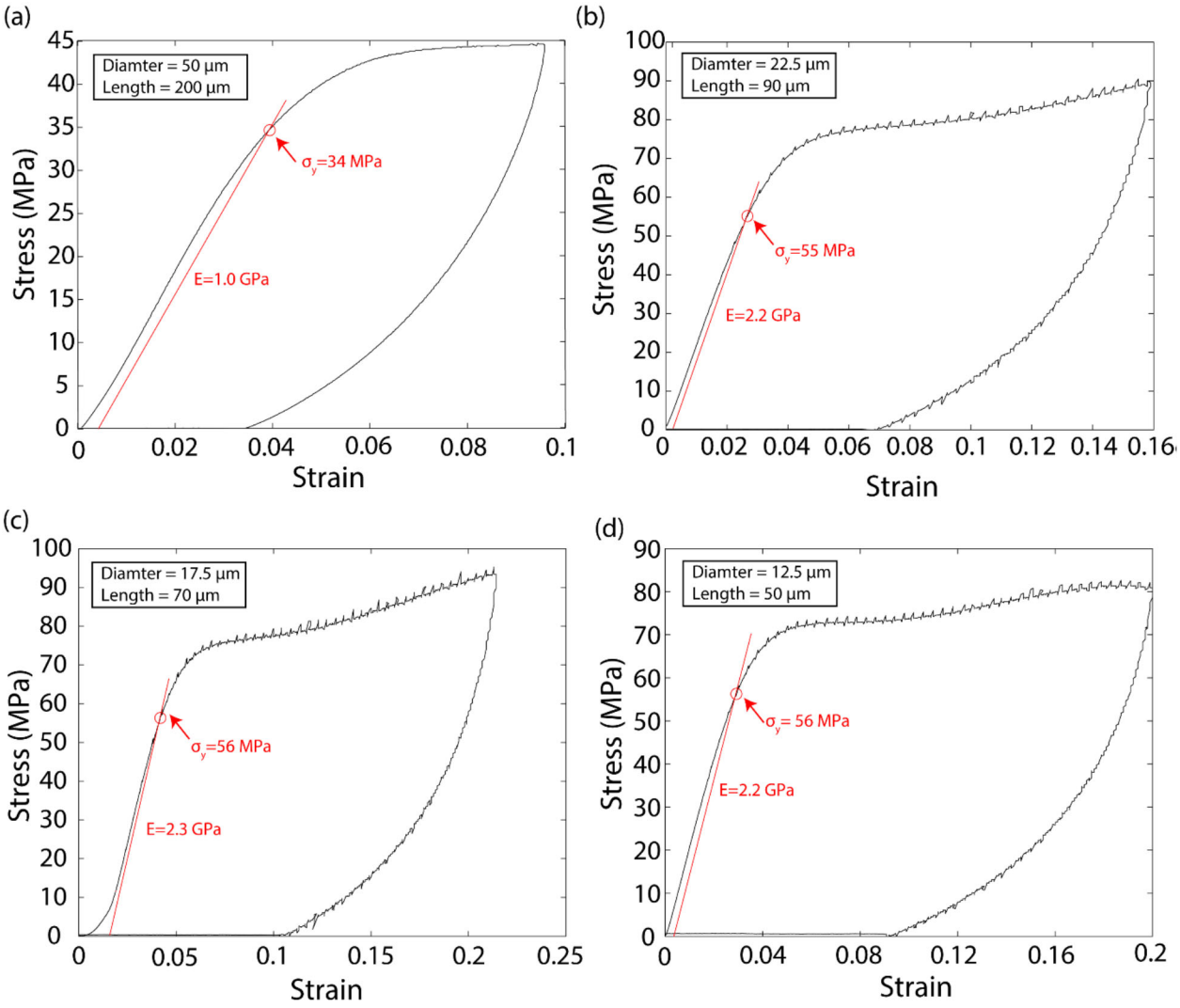

Fig. 1*. Uniaxial response of the material IP-Dip, measured by compression experiments on micro-pillars of aspect ratio of 4 and different diameters, manufactured by two-photon polymerization Direct Laser Writing with a Nanoscribe Photonics GT Professional.*

The most common TPP materials are negative-tone acrylate based resins [74], [79], due to their processing ease and the wide assortment of functionalities and monomer sizes [80]. Other successfully employed materials include epoxies, most notably SU-8 [81], hydrogels [82], organic–inorganic hybrids [83], proteins [84], and elastomers like PDMS [85]. In the simplest

case, acrylate resins consist of a monomer, which will be cross-linked, and a photo-initiator, which absorbs light and cleaves into free radicals which then start the polymerization reaction. During polymerization via radical chain growth, several initiation, propagation, and termination reactions, each with their own different rates, occur simultaneously. Monomers react only with the propagating reactive center, not with other monomers, and chain addition ceases when the concentration of radicals is depleted by a number of termination reactions.

The mechanical properties of acrylate-based resins [79], [86], the most commonly used TPP materials, are related to the degree of conversion (*DC*), a measure of the cross-linking density between polymer chains, which is determined by the light exposure dose during printing. The TPP exposure dose, as well as the print quality and speed, mainly correlate with three process parameters: the laser average power (*P*), the writing speed (*v*) and the writing density. The latter one can be quantified by the hatching (*dh*) and the slicing (*ds*) distances between neighboring voxel-lines.

In this study, we systematically characterize the mechanical properties of the two-photon polymerized acrylate-based resin IP-Dip. We report the direct measurement of the mechanical properties of individual voxel-line features and derive the mechanisms controlling the effective mechanical properties of TPP-derived hatched parts. Specimens spanned multiple length scales, from 190 nm to centimeters (Fig. 2a), including nanowires consisting of individual voxel-lines, multi-voxel-line bars and conventionally cured bulk samples. We measure Young's modulus (E), yield strength (σ_y), ultimate tensile strength (σ_{UTS}), and degree of conversion by uniaxial compression and tension experiments and Raman micro-spectroscopy, respectively (Fig. 2b–d). We find that the mechanical properties of solitary voxel-lines are largely independent on their size

and the applied TPP process parameters, suggesting the existence of a mobility threshold which counterbalances the expected process parameter-sensitivity.

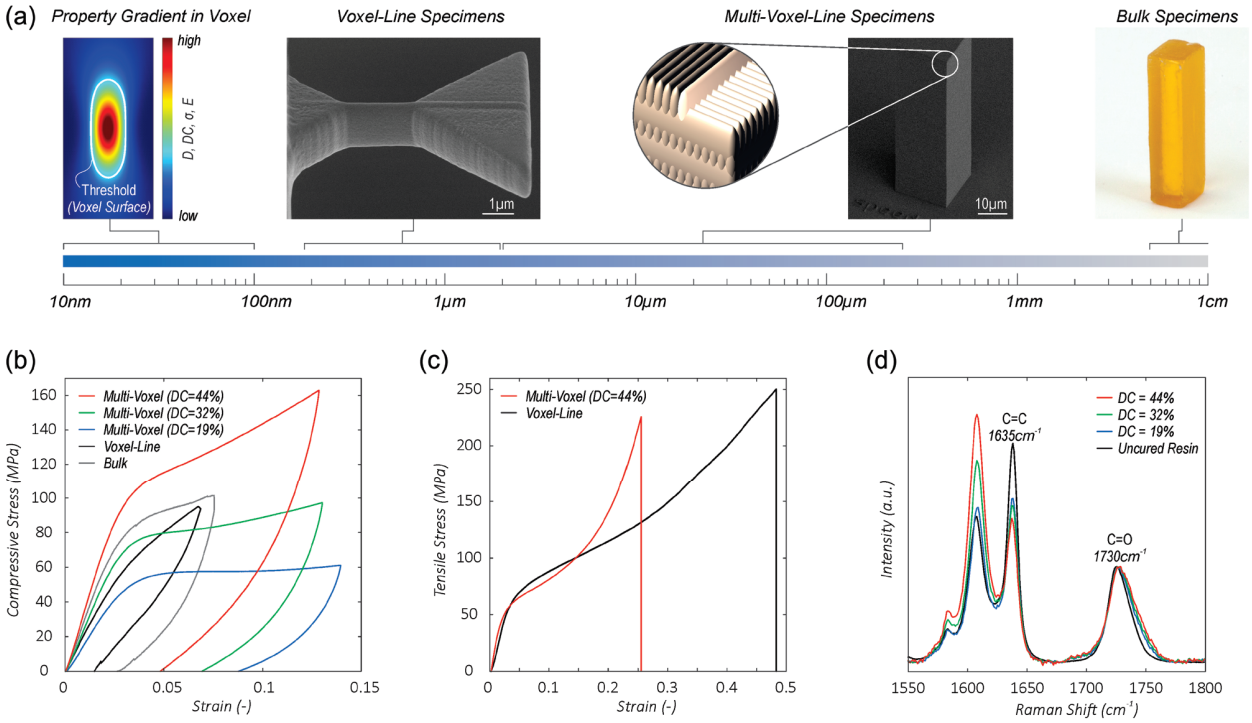

Fig. 2. *Mechanical characterization of the triacrylate TPP resin IP-Dip from nanowires to bulk, from polymerization to damage threshold. a) The investigated length scale ranges from sub-voxel gradients over individual voxel-lines and multi-voxel-line hatched specimens to conventionally cured bulk material. Representative b) compressive and c) tensile stress–strain curves and d) Raman spectra show the large tailorability of strength, stiffness and degree of conversion (DC) of multi-voxel-line hatched specimens compared to solitary voxel-lines and bulk specimens.*

For the single voxel-lines, keeping printing speed constant at 10 µm s^{-1}, we manufacture and test two sets of samples, one with varying width from 190nm to 640 nm and the other with varying laser power across the entire dynamic range of the photoresist. The mechanical properties of voxel-lines are found to be largely insensitive to their size and applied TPP process parameters. In

contrast to individual voxel-lines, the mechanical properties of hatched multi-voxel-line specimens show a pronounced dependency on the TPP process parameters (Fig. 3), consistent with previously reported data[75], [77]. We examine the impact of different combinations of laser average power, writing speed and writing density. E, σ_y, and DC are measured by uniaxial compression and by Raman spectroscopy of bars with nominal dimensions of 20 × 20 × 65 μm, with a constant hatching-to-slicing-distance ratio (d_s/d_h = 2). Combining all experimental results from Fig. 3, shows a linear dependency of E and σ_y with the DC. Independent from specific process parameters, specimens with the same DC roughly have the same mechanical properties. E and σ_y approximately increase with the DC as

$$E = (9.52DC - 0.56)GPa$$

$$\sigma_y = (170.36DC - 0.84)MPa$$

The pronounced tailorability of the mechanical properties of hatched two-photon-polymerized material compared to solitary voxel-lines may primarily be caused by the "memory effect." Depending on the combination of P, ν, d_h, and d_s, the dose distributions of neighboring exposures overlap to different extents. Simply speaking, neighboring voxel-lines increasingly overlap as they become "larger" (with increasing P and decreasing ν) and as d_h and d_s are reduced, thus creating a bandwidth of effective properties even if those of corresponding solitary voxel-lines would be identical. Thereby, existing insoluble material with relatively low DC, like the surface region of previously solitary voxel-lines, is further cross-linked, producing an increase in the effective properties relative to those of solitary voxel-lines.

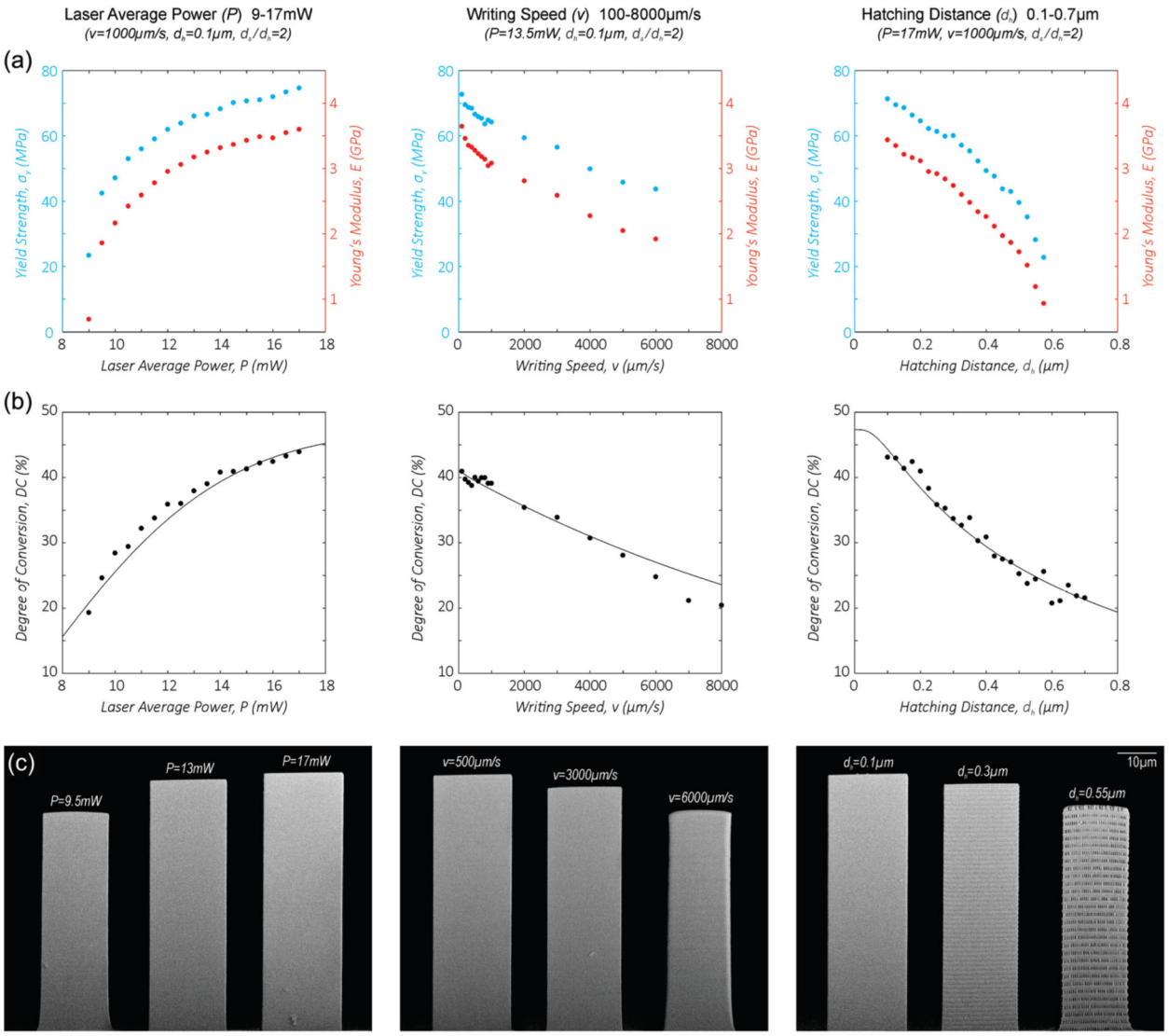

Fig. 3. *TPP process parameters tailor the mechanical properties of hatched multi-voxel-line specimens. Laser average power (P), writing speed (v) and hatching distance (d_h) (left to right column) have a characteristic impact on a) compressive yield strength (σ_y), Young's modulus (E) and b) degree of conversion (DC). Measured DC values are complemented by analytical prediction. c) SEM images of selected specimens.*

In a follow up study [55], we investigated the thermal post-curing route as an effective and simple method to increase the mechanical properties of acrylate-based TPP-DLW-derived parts by 20-

250% and to largely eliminate the characteristic coupling of processing parameters, material properties and part functionality (Fig. 4). We examined the impact of a one-hour thermal treatment, at 200°C in vacuum, on the mechanical properties of TPP-printed IP-DIP. The effect of the post-curing treatment was characterized for a wide range of the TPP-parameters, which covered the entire dynamic range of the material, from the solubility to the damage exposure dose threshold. The DC values were calculated from Raman micro-spectroscopy measurements.

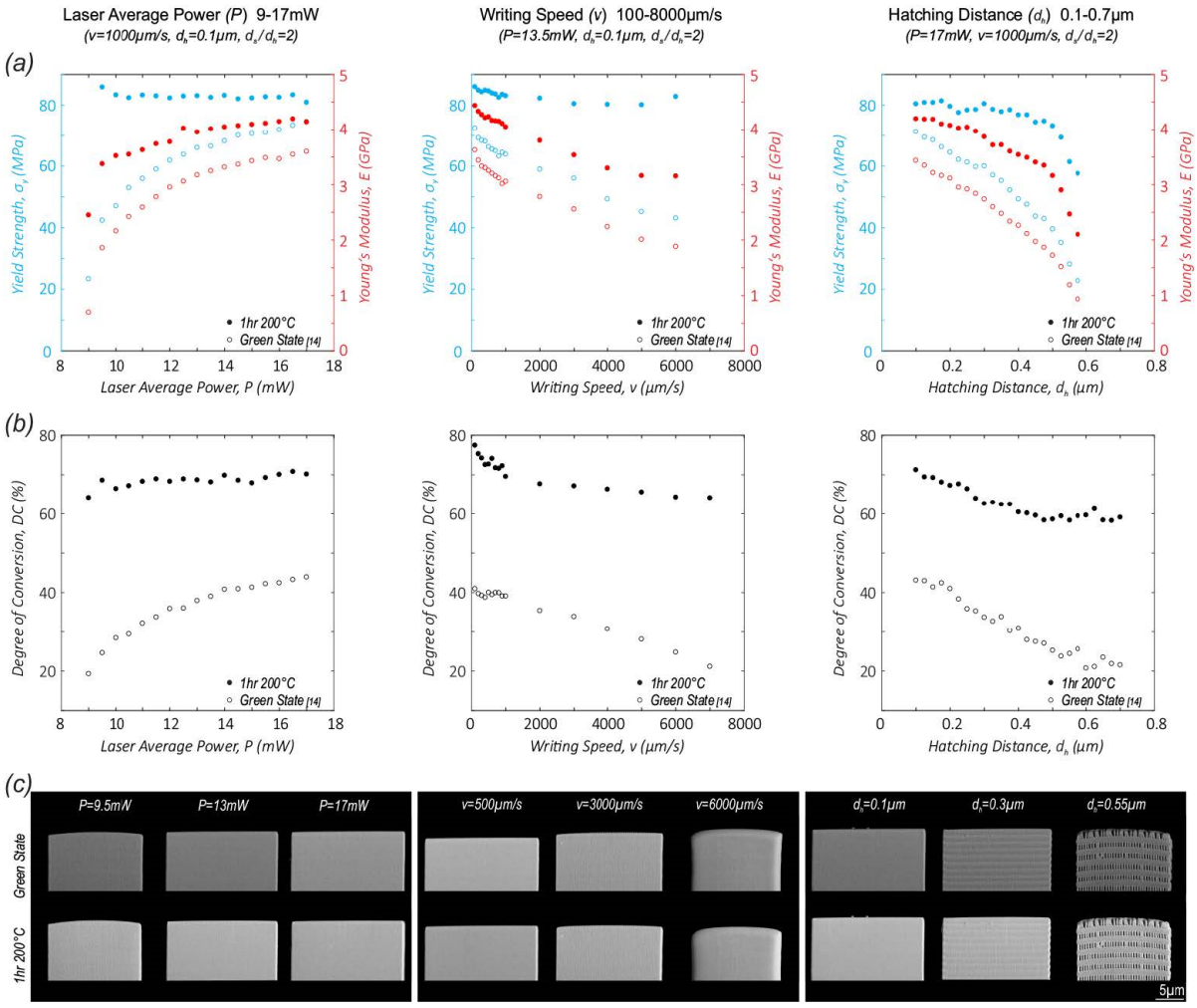

Fig. 4. *Thermal post-curing nearly eliminates the characteristic process parameter sensitivity in the mechanical properties of TPP-derived micro-bars. (a) Compressive yield strength (σ_y), blue data points, Young's modulus (E), red data points, and (b) degree of conversion (DC) with and*

without thermal post-curing, depending on laser average power (P), writing speed (v) and hatching distance (d_h) (left to right column). (c) Close-up SEM images of selected specimens before and after thermal post-curing.

Thermal post-curing drastically reduced the pronounced characteristic process-parameter dependencies in the mechanical properties of TPP-derived parts (Fig. 4). Degree of conversion, yield strength and Young's modulus after thermal post-curing were fairly tightly distributed, with only minor process parameter dependency remaining. The treatment thereby drastically increased strength and stiffness of the weakest green specimens by up to 250% and 100%, respectively. Specimens with the highest achievable green properties, printed with TPP-doses approaching the damage threshold of the material, had increased average strength and stiffnesses of 15% and 21%, respectively. Independent from the TPP process-parameter combination, the thermal post-curing treatment did not affect the surface quality and shape of the specimens.

Thermal post-curing of acrylate based-resins is achieved via thermal self-initiation reactions, which do not depend on an initiator diffusing inwards and hence are not part-geometry sensitive. At temperatures above 120°C, acrylic monomers and oligomers can polymerize in absence of any known thermal initiator[87]–[89]. In addition to self-initiation, the elevated temperature increases the mobility of trapped photo-initiated radicals, accelerating reactions which were at room temperature halted by steric hindrance [90].

Contribution statement

The work about the mechanical properties and thermal post-curing of the resin IP-DIP discussed in this subsection has been published [54], [55]. In both studies, the author of this thesis performed and analyzed the majority of the compression tests and contributed to the interpretation of the results.

1.4 Fabrication and mechanical characterization of nano-architected materials with spinodal topologies produced by TPP-DLW

In a largely computational study from our research group [53], spinodal microstructures were generated by the numerical solution of the Cahn-Hilliard equation. We investigated two different topologies: 'solid models' (Fig. 5), where one of the two phases is modeled as a solid material and the remaining volume is void space; and 'shell models' (Fig. 6), where the interface between the two phases is assumed to be a solid shell, with the rest of the volume modeled as void space. Finite element meshes were generated for each model, and the uniaxial compressive stiffness and strength were extracted. We showed that the shell spinodal topologies are remarkably efficient, displaying stretching dominated behavior over a very wide range of relative densities (Fig. 7). The exceptional mechanical efficiency of shell spinodal topologies is attributed to its uniform surface curvature, which results in a very uniform local stress distribution upon loading, avoiding areas of substantial stress intensification.

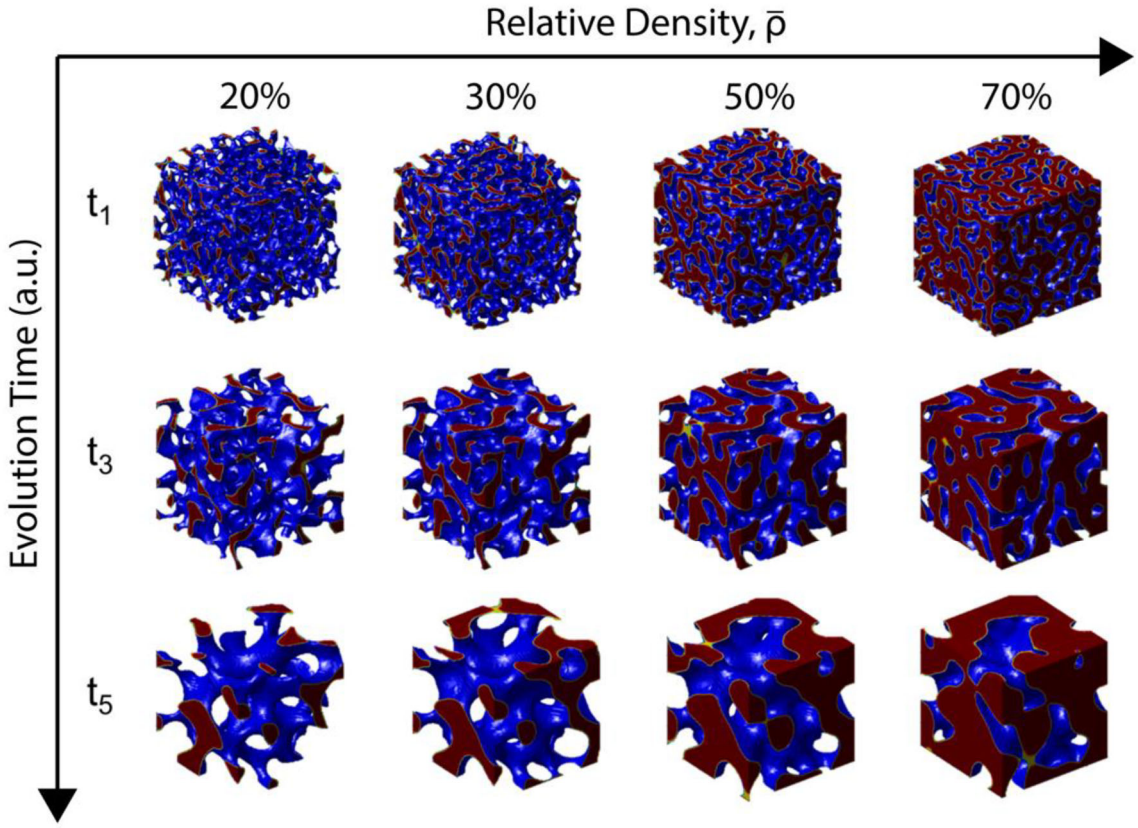

Fig. 5. *3D spinodal solid models with different relative densities, ρ = 0.2, 0.3, 0.5, and 0.7, extracted at different evolution times, t1, t3, and t5.*

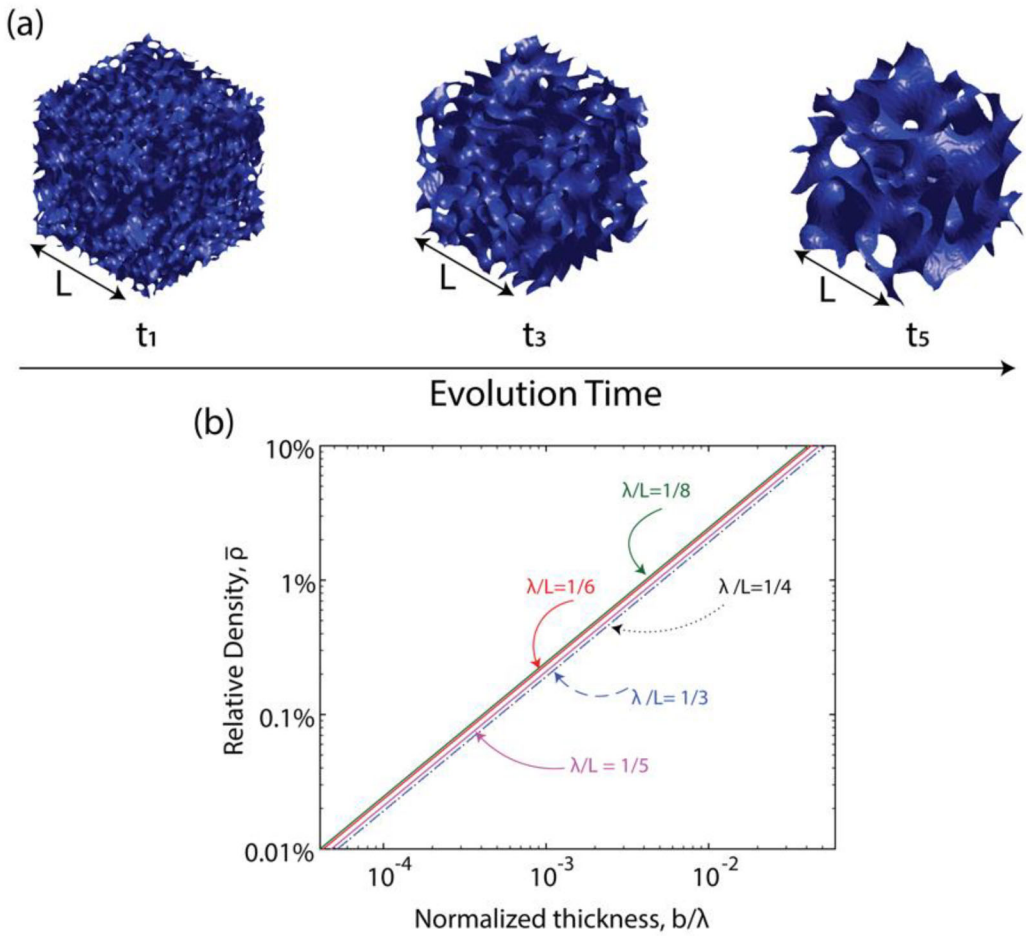

Fig. 6. *(a) 3D spinodal shell models corresponding to the interfaces of spinodal solid models of ρ = 0.5, extracted at three different evolution times (t1, t3, and t5). (b) Relative density of shell spinodal cellular materials, as a function of the shell thickness, b, normalized by the characteristic feature size, λ. L denotes the cubic domain size.*

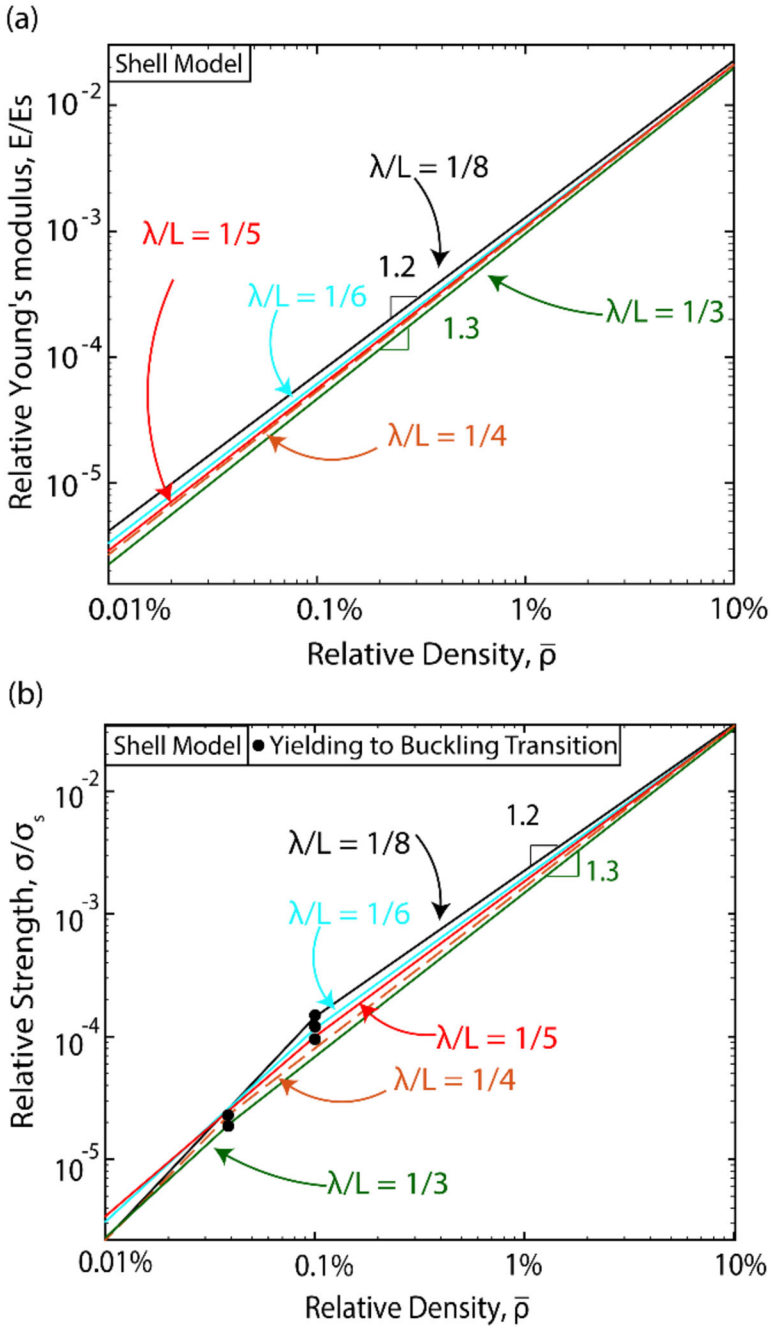

Fig. 7. *Numerical predictions of (a) Relative Young's modulus and (b) relative yield strength of spinodal shell models, as a function of their relative density, ρ. The constituent material has Young's modulus, E_s= 210 GPa and yield strength, σ_{ys}=235 MPa. Different curves refer to models with different characteristic feature size, λ. L denotes the domain size. The black dots mark the transition from yielding to buckling failure.*

Thin shells (and by extension thin shell-based architected materials) are known to be stiff and strong but significantly sensitive to geometric imperfections [91], a characteristic that significantly limits their load carrying potential in practical applications. To quantify this effect in spinodal shell models, an imperfection sensitivity analysis was performed (Fig. 8). A very notable conclusion emerges: the topology with 8 x 8 x 8 'unit cells' in the domain (Fig. 8a) is absolutely imperfection insensitive, with imperfection magnitudes as large as 20 times the shell thickness showing no effect on the mechanical response. Even for very coarse topologies, with only 3 x 3 x 3 'unit cells' in the domain (Fig. 8b), the imperfection sensitivity becomes appreciable only when ψ~10. Overall, the remarkable conclusion is that, unlike regular shell-based architected materials, spinodal shell based architected materials are remarkably imperfection insensitive; this important characteristic is attributed to the stochastic nature of the spinodal shell topologies.

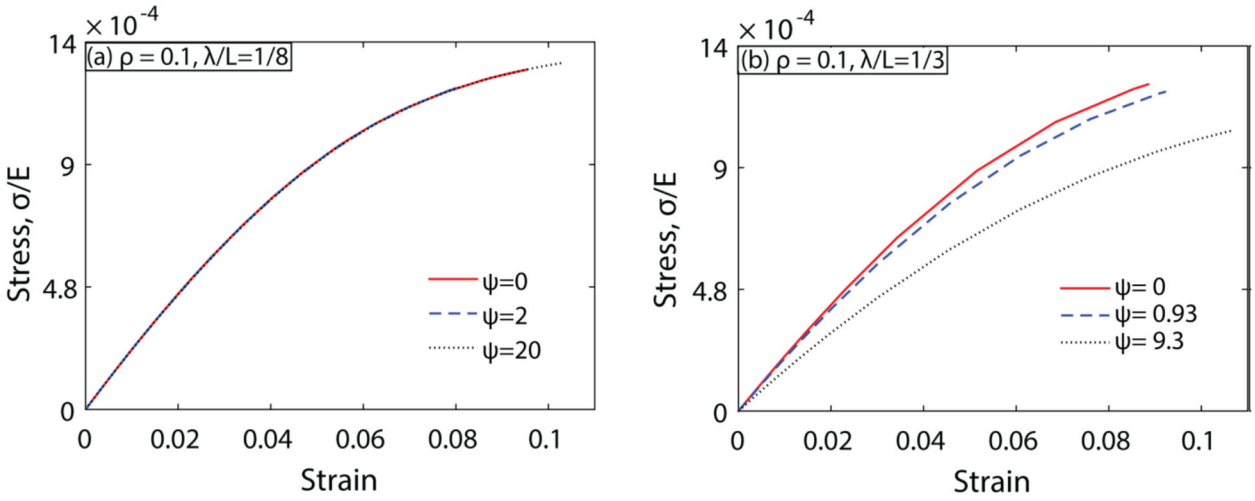

Fig. 8. *Imperfection insensitivity of shell spinodal models. The non-dimensional imperfection magnitude, ψ, is defined as the largest displacement from a perfect mesh normalized by the shell thickness. Comparison of post-buckling stress-strain curves of 10% dense spinodal shells with characteristic feature size, $\lambda/L=1/8$ (a) and for $\lambda/L=1/3$ (b), with three different magnitudes of*

imperfection. The constituent material has Young's modulus, $E_s = 210\ GPa$ *and yield strength,* $\sigma_{ys} = 235\ MPa$.

As an effort to verify the accuracy of the finite element simulations, a selective set of cellular material samples with solid and shell spinodal topologies were fabricated and tested in uniaxial compression. All samples were fabricated at the micro-scale via two-photon polymerization Direct Laser Writing (DLW), using a Nanoscribe Photonic Professional GT and a negative tone photoresist (IP-Dip, produced by Nanoscribe GmbH). All samples were fabricated using the Galvo mode with the 63X, N.A. 1.4 objective lens. Printing parameters were 35 mW and 17,000 μm/s for laser power and scan speed, respectively. Cubic samples with edge length, L=140 μm, are generated, using the solid and shell spinodal geometries. A characteristic feature size, λ/L=1/5, is used for all samples. Solid spinodal samples with relative densities of 20%, 30% and 50%, and shell spinodal samples with relative densities of 5%, 7% and 10% were fabricated, respectively (all shell spinodal topologies were extracted from a 50% dense solid spinodal). After DLW, samples were first immersed in propylene glycol monomethyl ether acetate (PGMEA) for 20 minutes to dissolve the remaining liquid resin, and subsequently in isopropanol for 2 minutes for final cleaning. See Fig 10 for SEM images of all samples.

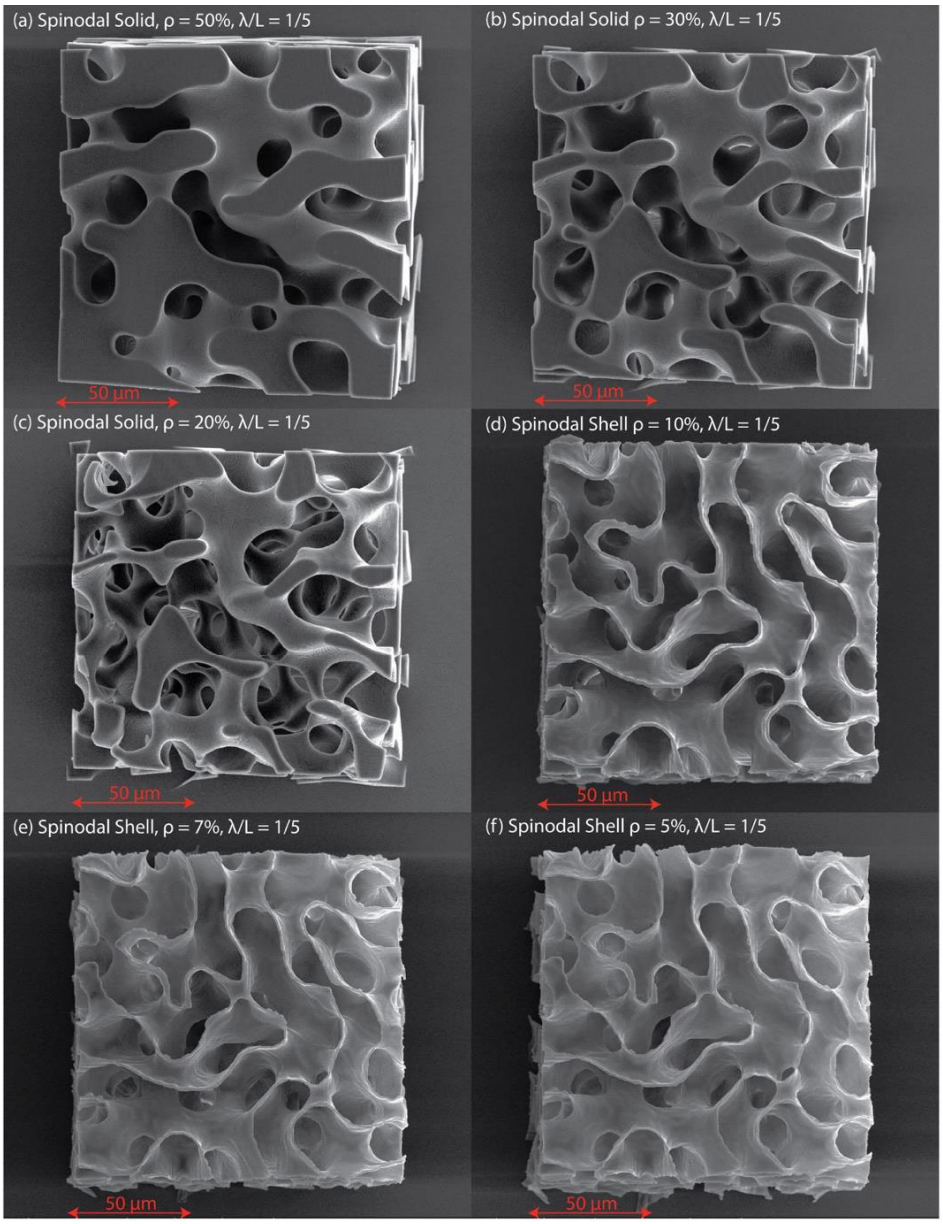

Fig. 9. *SEM images of spinodal samples fabricated in IP-Dip by two-photon polymerization Direct Laser Writing. All samples have characteristic feature size, $\lambda/L=1/5$, with L the domain size. (a) Spinodal solid model, $\rho = 50\%$. (b) Spinodal solid model, $\rho = 30\%$. (c) Spinodal solid model, $\rho = 20\%$. (d) Spinodal shell model, $\rho = 10\%$. (e) Spinodal shell model, $\rho = 7\%$. (f) Spinodal shell model, $\rho = 5\%$.*

The mechanical response of all spinodal structures was characterized by displacement-controlled uniaxial compression tests with a maximum strain of 15%, performed at a constant strain rate of $0.005/s$. All tests were performed with an Alemnis Nanoindenter. Load-displacement curves were recorded and extracted, and converted to stress-strain curves. To compare experimental results with numerical predictions, finite element models of the same topologies were generated and loaded in uniaxial compression. In order to extract the base material properties for the numerical analyses, a number of IP-Dip cylinders with diameters between 12.5 and 50μm and aspect ratios of four were DLW printed with the same parameters as the spinodal samples and tested in uniaxial compression. The stress-strain curves of each pillar under compression are shown in Fig 1. Although the size effect exists, the convergence is reached for pillar diameters that are less than 2.5 μm. Corresponding to the experimental results, the base material was modeled as elastic-perfectly plastic, with Young's modulus, E_s=2 GPa, and yield strength σ_{ys}=60 MPa.

Experimental and numerical stress-strain curves are compared in Fig. 10 a-b, for solid and shell spinodal models, respectively. Despite the difference in boundary conditions between simulation (constrained side faces) and experiments (free side faces), the agreement is excellent throughout. The stress-strain curves of spinodal solid and shell models under compression were validated against those of the experiments as shown in Fig. 10.

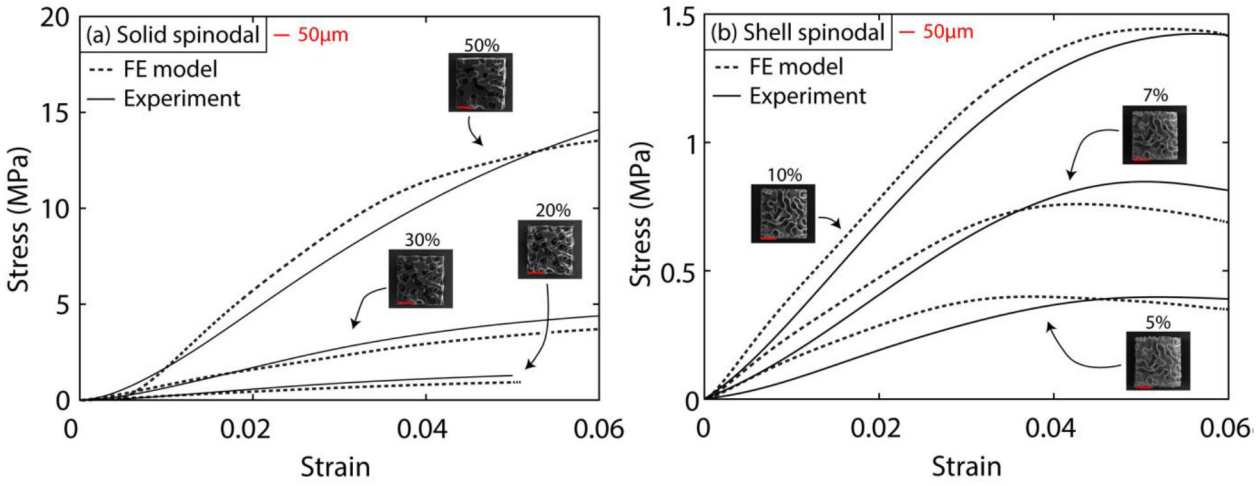

Fig. 10. *Comparison of numerical and experimental stress-strain curves for (a) solid and (b) shell spinodal topologies at different relative densities, loaded in uniaxial compression. The characteristic feature size, $\lambda/L=1/5$ is used for all models. The insets depict SEM images of the samples, fabricated by two-photon polymerization Direct Laser Write in IP-Dip, with a Nanoscribe GT Photonics Professional, and tested with an Alemnis Nanoindenter. Higher resolution SEM images of all samples are shown in Fig. 9. The properties of IP-Dip were measured by micropillar compression tests, and input in the simulations as an elastic-perfectly plastic solid with $E_s=2$ GPa, and yield strength $\sigma_{ys}=60$ MPa.*

It is instructive to compare the mechanical efficiency of solid and shell spinodal topologies to that of a wide range of strut-based and shell-based architected materials, in particular solid strut metallic nanolattices [8], solid strut carbon nanolattices [4], hollow strut metallic micro-lattices [5], [92], hollow strut ceramic nanolattices [6], and two mechanically efficient metallic shell-based architected materials, the P-surface material [93] and the D-surface material [94]. These comparisons are presented in Fig. 11 in terms of relative Young's modulus, E/E_s, and relative yield strength, σ_y/σ_{ys}, versus relative density, ρ. It's clear that in the low-relative density regime (ρ<1%)

porous materials with shell spinodal topologies outperform most strut and shell-based porous materials in terms of specific stiffness and strength.

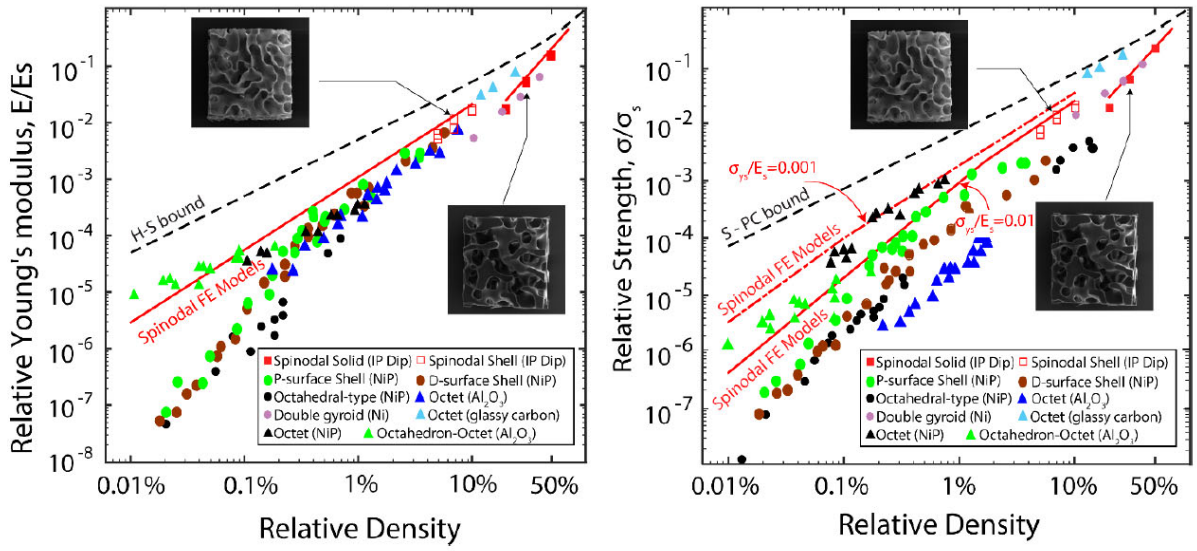

***Fig. 11**. – Comparison of the mechanical performance of solid and shell spinodal topologies and well-established strut-based and shell-based architected materials: solid strut metallic nanolattices*[8]*, solid strut carbon nanolattices*[4]*, hollow strut metallic micro-lattices* [5], [92]*, hollow strut ceramic nanolattices*[6]*, and two mechanically efficient metallic shell-based architected materials, the P-surface material*[93] *and the D-surface material*[94].

Contribution statement

The work about mechanical properties of spinodal topologies discussed in this subsection has been published [95]. The author of this thesis manufactured and tested all the micro-scale spinodal topologies through TPP-DLW, validating the results of numerical simulations.

1.5 Mechanical characterization of micro-architected materials with spinodal topologies produced by self-assembly routes

As shown in previous sections, cellular materials with spinodal shell topologies have been proven to possess excellent mechanical efficiency. However, the most promising characteristic of spinodal topologies is that they are amenable to scalable self-assembly.

In a recent collaborative study with the Ragan, Mohraz and Mumm labs at UCI, bicontinuous interfacially jammed emulsion gels (bijels) were formed and processed into sacrificial porous Ni scaffolds for chemical vapor deposition to produce freestanding three-dimensional turbostratic graphene (bi-3DG) monoliths with high specific surface area and spinodal shell topologies. The process schematic is shown in Fig. 12.

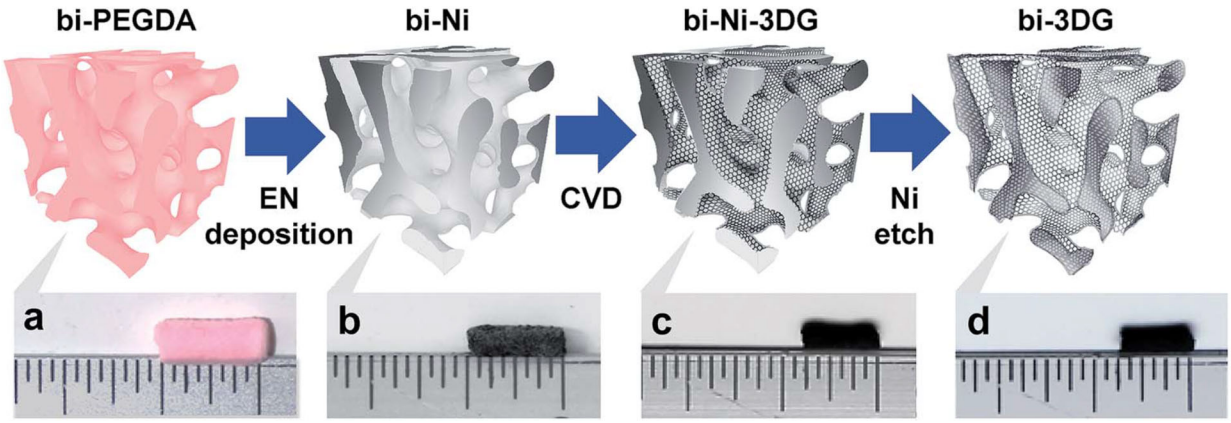

Fig. 12*. Schematic illustrating the bi-3DG synthesis process. (a) First, a bi-PEGDA template is made via a spinodal decomposition of a polymer infiltrated lutidine : water : silica mixture. (b) The bi-PEGDA is coated with Ni via electroless deposition and put through a 2-step thermal cycle to decompose the PEGDA and reduce Ni to create a bi-Ni scaffold. (c) CVD using methane on the Ni template is performed, resulting in bi-Ni-3DG. (d) Finally, the Ni backbone is etched, leaving behind a 3D graphene structure, bi-3DG. Below each schematic is an optical image of the*

macroscopic structure alongside a ruler. The bi-PEGDA has a length of approximately 0.25 inches.

Two types of graphene bijel-templated architectures were manufactured and tested mechanically, (i) bi-3DG (Fig. 13a), which is manufactured through the process shown in Fig. 12. (ii) bi-2-3DG (Fig. 13b), where extended H_2 annealing of the bi-Ni template is used to reduce the density of metal grain boundaries before CVD growth.

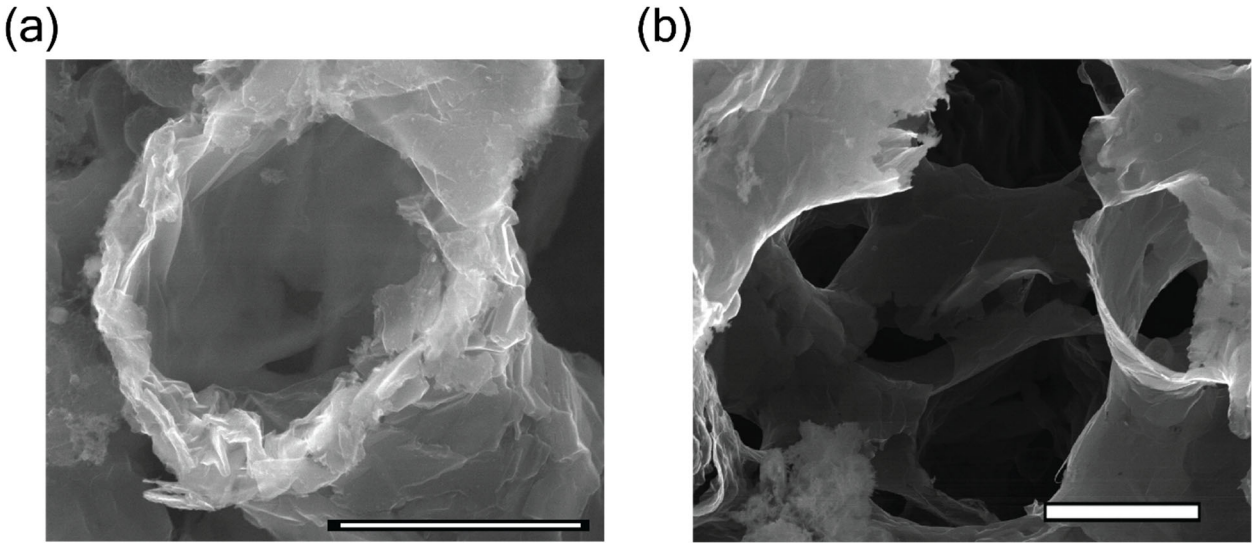

Fig. 13. *(a) Cross-sectional SEM image of a pore within 3D graphene structure bi-3DG grown on Ni architecture. The scale bar is 4 μm. (b) SEM images of graphene bijel-templated architectures bi-2-3DG architectures where the nickel was annealed at 900 °C in forming gas before CVD growth with scale bars of 10 μm.*

The mechanical properties of bi-3DG samples were evaluated via uniaxial compression with an Alemnis nanoindenter operated in displacement-control mode. A stress-strain curve obtained from a bi-3DG cylindrical sample with a diameter of 0.87 mm, a height of 1.24 mm, and a bulk density

of 42 mg/cm3 is shown in Fig. 14. A yield strength of approximately 130 kPa was measured, after which the sample displays a remarkably ductile and irreversible response upon compression. Notice that the response of bi-3DG pillars is significantly different from the classic compressive response of ceramic foams, which fail by progressive cracking of the base material, with visible stress drops [2], and much more similar to that of metallic systems. Intriguingly, the irreversible deformation beyond the linear elastic region is not characterized by a flat stress plateau, as commonly observed in elastic and plastic foams, but a region of continuous stress increase (akin to hardening in solid metals), accompanied by stiffening (see below). While this behavior has been observed multiple times in ultralight architected materials that deform reversibly by local buckling and/or localized fracture of the shell walls followed by extensive local rotations of ultra-thin ligaments with minimal local strains [5], [6], [96], it is not typically observed in architected materials that undergo irreversible deformations. While a full understanding of the internal deformation mechanisms that lead to this macroscopic behavior would require *in-situ* characterization upon loading that are beyond the scope of this work, we interpret that the irreversible hardening/stiffening response of the bi-3DG material is due to sequential cracking/sliding of the graphene layers at a scale of the order of the characteristic length of the spinodal microstructure, followed by local densification.

Multiple loading-unloading curves were extracted and plotted in Fig. 14a to enable calculation of the Young's modulus (measured upon unloading, as illustrated in Fig. 14b) as a function of the macroscopically applied strain. The modulus *versus* strain evolution is depicted in Fig. 14c. Notice that the modulus is initially very low, 4 ± 1.3 MPa, as averaged over three nominally identical samples; this is attributed to the well-documented challenge in collecting modulus data at very low applied strain in ultra-light architected materials [53]. At a strain of approximately 20%, the

modulus stabilizes to a plateau value of 20 MPa. This value is taken as a reasonable estimate for the modulus of bi-3DG materials. At a strain of approximately 50%, the modulus starts increasing again with applied strain. This rise should not be attributed to densification, for two reasons: (i) Densification in cellular materials occurs at compressive strains of the order of $1 - \alpha\rho$ with ρ the relative density of the materials and $\alpha = 1.5$. While the relative density of these samples is not easy to measure, a rough estimate of 0.02 can be estimated by dividing the bulk density of the sample (42 mg/cm3) by the mass density of graphite (2,260 mg/cm3). This value yields a calculated densification strain of approximately 97%, which is far higher than the approximately 50% strain at which the modulus starts increasing. (ii) The modulus at 70% strain is still orders of magnitude lower than that of solid graphene, or even graphite. As mentioned above, we tentatively attribute the rise in modulus with strain to localized fracture of the graphene layers and local rearrangement of the porous microstructure upon loading.

Mechanical tests are repeated on a bi-2-3DG pillar, and are shown in Figs. 16d-f. A plateau modulus of 30 MPa is extracted for this sample from Fig. 14f. This represents a 50% increase when compared to the bi-3DG sample, demonstrating the improvement in physical properties that occurs by increasing the grain size of the Ni scaffold. The increase in Young's modulus of bi-2-3DG over bi-3DG is tentatively attributed to increased interconnectivity of the graphene layers, as observed in the SEM image of Fig. 13b.

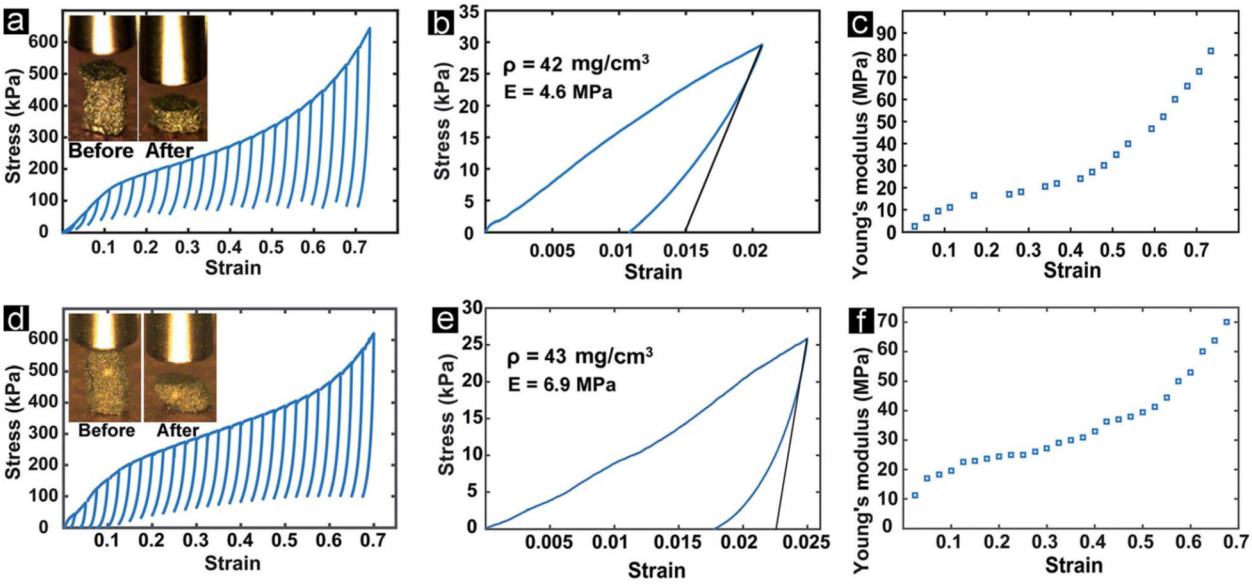

Fig. 14. *Nanoindentation measurements of a (a–c) graphene bijel-templated pillar with diameter 0.87 mm and height of 1.24 mm and of a (d–f) similar pillar, pre-annealed, with diameter 0.71 mm and height of 1.4 mm. (a and d) Stress–strain tests are performed on the same pillar with a strain rate of 1.2 mms^{-1}. Insets are before and after optical images of the graphene bijel-templated pillars. (b and e) Stress–strain curve acquired with a strain rate of 0.25 mm s^{-1}. (c and f) Young's modulus vs. strain from the tests.*

Compared with the cellular materials with spinodal shell topologies used in the computational model or the ones manufactured with additive manufacturing [53], spinodal shell topologies manufactured with self-assembly have much less defined topologies and more defects from the manufacturing process. This might partly explain the reason why the relative stiffness of self-assembled spinodal shell topologies is orders of magnitude lower than that predicted in the model at the same relative density. However, both the 3D bijel-template architectures are still between 20 and 4000 times stiffer than previously reported graphene-based materials with other topologies[97]–[100]. In addition, through improvement of the quality of the graphene layers, bi-

2-3DG pillar is 50% stiffer than bi-3DG pillar which demonstrate that the mechanical properties of the graphene structure can be further improved by optimizing the manufacturing process. This result further highlights the great potential for mechanical and multifunction application of spinodal shell topologies manufactured via self-assembly.

Contribution statement

The work about the mechanical properties of macroscopic graphene pillars with spinodal shell microstructures discussed in this subsection has been published [101]. The author of this thesis performed and analyzed all the mechanical tests of the pillars, and interpreted the experimental results.

1.6 Conclusions

In summary, we manufactured and tested micro-scale cellular materials with spinodal shell topologies manufactured through two-photon polymerization direct laser writing (TPP-DLW), experimentally verified the simulation results, and confirmed that architected materials with spinodal shell topologies possess excellent mechanical efficiency.

Initial findings of the mechanical properties of the acrylate-based resin IP-Dip used in TPP-DLW are expanded into a systematic study to establish the correlation between mechanical properties of the resin and processing parameters of the printing process. We also introduce a thermal post-curing route as an effective and simple method to increase the mechanical properties of TPP-DLW printed parts and to largely eliminate the characteristic coupling of processing parameters.

Finally, as part of a recent collaboration, we investigated the mechanical properties of macroscopic pillars with spinodal shell microstructure manufactured through the scalable bicontinuous interfacially jammed emulsion gels(bijels) method. The results further highlight the great potential for mechanical and multifunction application of spinodal shell topologies manufactured via self-assembly.

Chapter 2 Mechanical performance of interpenetrating phase composites (IPCs) with spinodal topologies

2.1 Introduction

As shown in chapter 1, cellular materials with spinodal shell topologies are exceptionally efficient from the perspective of specific stiffness and strength, when compared to both cellular materials with spinodal solid topologies and truss-based lattice materials [53], and perform on par with cellular materials with triply periodic minimal surface (TPMS) topologies [93], [94]. The similarity with TPMS topologies can be attributed to the very tight distribution of curvatures in spinodal topologies, with the vast majority of surface patches possessing near-zero mean curvature and negative Gaussian curvature, the signature feature of TPMSs. Remarkably, the intrinsically stochastic nature of spinodal shell topologies (and hence the deviation from minimal surface characteristics) not only does not significantly depress mechanical properties, but rather results in considerable imperfection insensitivity [53]. Whether the unique combination of scalable manufacturing and mechanical performance shown by cellular materials with spinodal topologies also translates to interpenetrating phase composites with spinodal topologies remains to be demonstrated.

In this chapter, we experimentally investigate the mechanical properties of interpenetrating phase composites with spinodal shell reinforcement, with emphasis on stiffness, yield strength and energy absorption under non-linear deformations. Spinodal shell-based IPCs are compared with composites with other reinforcement topologies, namely (1) spinodal solids, where both phase topologies are directly obtained by spinodal decomposition [46], [47]; (2) octet lattices, the most widely studied cellular architecture [102]–[104]; and (3) Schwarz P surfaces, one of the most

mechanically efficient TPMS topologies [36], [105]. While a wide range of truss lattice and TPMS topologies exist, and many have been characterized mechanically, the octet lattice and the Schwartz P surface approach upper bounds of performance for the two classes of periodic reinforcement topologies, respectively, and are thus ideal candidates for assessing the mechanical efficiency of spinodal shell reinforcements. In order to accurately control all topologies, all IPCs in this study are produced by multi-material jetting, a recently developed additive manufacturing technique. While the resulting materials are polymer/polymer composites, the significant difference in mechanical properties between the two constituents allows extraction of mechanistic understanding that can be readily extend to other classes of composite materials, including ceramic/metal composites.

2.2 Materials and methods

2.2.1. Numerical generation of the reinforcement topologies

2.2.1.1 Spinodal solid topology

The spinodal solid topology was generated numerically with the approach reported in [53] and Appendix A. A short synopsis of the procedure is presented here. A 50% dense spinodal solid cellular topology is generated by solving the Cahn–Hilliard evolution equation [41], one of the classic evolution models for spinodal decomposition. The Cahn–Hilliard equation can be written as:

$$\frac{\partial u}{\partial t} = \Delta\left[\frac{df(u)}{du} - \theta^2 \Delta u\right] \quad (1)$$

where $u(x,y,z,t)$ is the concentration of the material and void phases ($-1 \leq u \leq 1$, with $u = -1$ indicating solid material and $u = 1$ indicating void space) at a coordinate *(x,y,z,)*, *t* is the evolution time, $f(u) = \frac{1}{4}(u^2 - 1)^2$ is a double-well free energy function, θ is the width of the interface between the two phases and Δ is the Laplacian operator. The equation was solved in space and time over a cubic domain with edge length of *N*, via a finite difference algorithm. The evolution time controls the characteristic feature size (λ), a measure of the domain size of the topology. As time progresses, the features coarsen to reduce interfacial energy, thus increasing λ. We choose to extract our topologies at the evolution time corresponding to $\lambda = \frac{1}{5}$N (loosely corresponding to a sample with $5 \times 5 \times 5$ unit cells), as this number of unit cells was shown in previous studies to provide a homogenized response [53]. To produce spinodal solid topologies with volume fractions different from 50%, a thresholding technique is used. See appendix A for details.

2.2.1.2 Spinodal shell topology

The spinodal shell topology is extracted from the interface between the solid and void phases, produced as explained in sec. 2.2.1.1. The volume fraction of reinforcement, V_f, is chosen by assigning the appropriate thickness to the shell, t_s, so that $V_f = t_s A/V$, with *A* the surface area of the shell and *V* the sample volume. Spinodal shell topologies extracted from a 50% dense spinodal solid topology have negative Gaussian curvature throughout the shell, with mean curvature close to zero everywhere – thus approaching the geometrical characteristics of TPMSs. While spinodal shell topologies with non-zero mean curvature can be generated by extracting the surface of solid spinodal topologies with densities different from 50%, previous studies have demonstrated that their mechanical properties are inferior [53]. Hence in this work we will limit our attention to

spinodal shell topologies with near-zero mean curvature throughout. The procedure is schematically depicted in Fig. 15.

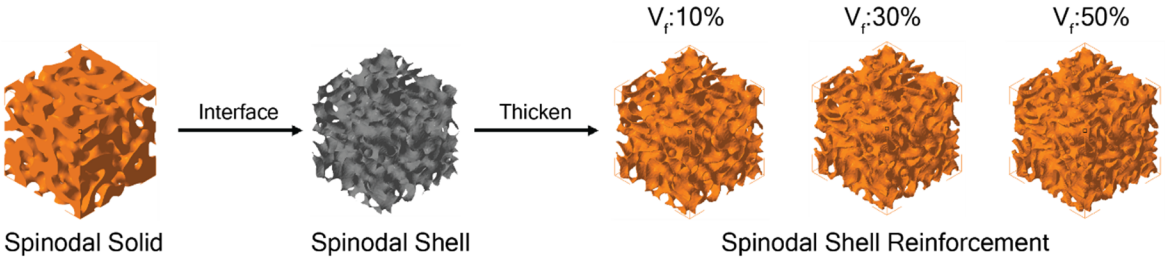

Fig. 15. *Method of creating spinodal shell reinforcement phase for IPCs.*

2.2.1.3 Schwarz P TPMS topology

The Schwarz P surface was created using the level set approximation technique from the implicit surface:

$$\cos(x) + \cos(y) + \cos(z) = 0 \tag{2}$$

where *(x,y,z)* is a coordinate point in three-dimensional Euclidean space. The minimal surface corresponding to the above equation is generated using *Minisurf*, a software used to generate minimal surface CAD files [106]. Cubic samples with $3 \times 3 \times 3$ unit cells were generated. As explained in sec. 2.2.1.2, the volume fraction of reinforcement, V_f, is chosen by assigning the appropriate thickness to the shell, t_s, so that $V_f = t_s A/V$, with A the surface area of the shell and V the sample volume.

2.2.1.4 Octet lattice topology

The octet lattice was built using the commercially available CAD modeling software package SolidWorks. Cubic samples with $3 \times 3 \times 3$ unit cells were generated. The volume fraction of reinforcement, V_f, is chosen by assigning the appropriate diameter to the bars, d, according to $V_f = 6\sqrt{2}\pi(\frac{d}{l})^2$ with l being the length of the strut [102].

2.2.2 Numerical generation of the IPC architectures

After the reinforcement phase topologies were generated, they were imported into Geomagic Design X, a reverse engineering software that can also be used to handle CAD files. After the appropriate shell thicknesses and bar diameters were generated to result in the desired volume fraction of reinforcement, each CAD model was subtracted from a cube of the same size with a Boolean cut operation to create the complementary matrix phase. Finally, the CAD files are converted into STL files and transferred to the GrabCAD software, the control software for the 3D printer. This process, along with the printed samples, is illustrated in Fig. 16.

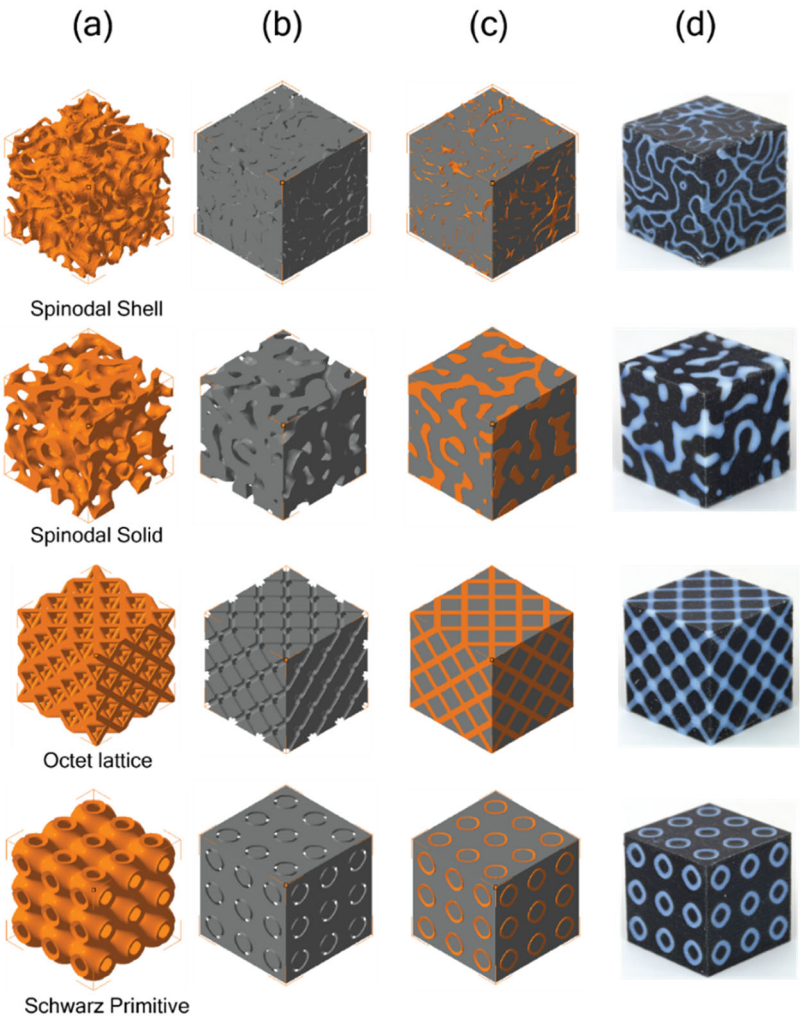

Fig. 16. *(a) Reinforcement phase, (b) matrix phase. (c) assembled interpenetrating phase composites, and (d) samples manufactured with 3D printing of spinodal shell, spinodal solid, octet lattice, Schwarz P shell IPCs.*

2.2.3 Fabrication approach

All samples were manufactured with a PolyJet 3D printer (Objet260 Connex3, Stratasys), which allows 3 different materials to be printed simultaneously, with intermediate (digital) formulations obtained by mixing appropriate amounts of the 3 constituent materials at any voxel location. The reinforcement phase in IPCs was printed with VeroWhitePlus, a glassy photopolymer, while the

soft matrix phase was printed with Agilus30, a rubbery polymer. All samples are 30x30x30 mm cubes. Selected reinforcement-only cellular materials were printed by replacing Agilus30 with support material, which was subsequently removed by water jetting. All 3D printed samples were left at room temperature for 4 days for curing.

2.2.4 Mechanical characterization

All mechanical tests were performed with an Instron 8800 mechanical test frame equipped with a 100kN load cell. The constituent materials were characterized under both uniaxial tensile and compression loading, using dog bone and cylindrical samples, respectively. Engineering stress and strain were extracted as $\sigma_0 = F/A_0$ and $\varepsilon_0 = \delta/\ell_0$, with F and δ the raw force and displacement measurements, and A_0 and ℓ_0 the original cross-section and length of the sample, respectively. True stress and true strains were obtained as $\sigma_t = \sigma_0(1 + \varepsilon_0)$ and $\varepsilon_t = \ln(1 + \varepsilon_0)$, respectively. The Young's modulus was extracted as the slope of the initial linear region.

All IPC composites and cellular materials were tested in compression only. ASTM 695-15 for compressive properties of rigid polymer was followed in all compression tests [107]. Engineering stress and strain were extracted as explained above. To minimize the influence of the anisotropic nature of 3D printing introduced by the layer-by-layer printing process, all compression tests were conducted in the direction parallel to the printing direction, which is known to be the strongest. A quasi-static strain rate of $0.001s^{-1}$ was used in all tests. All samples, except for those subjected to cyclic tests, were compressed to 50% strain to measure Young's modulus, 0.2% offset yield strength, and energy absorption. The latter was extracted as the area under the stress-strain curve

up to 50% strain. The cyclic test samples were compressed to 10% strain for three cycles using the same quasi-static strain rate as all in other tests.

2.3 Mechanical properties of constituent materials

Constituent materials were first tested in tension and compression as described in section 1.1.4. Stress-strain curves for the two materials are provided in Fig. 17. Notice that the reinforcement phase material is approximately three orders of magnitude stiffer than the matrix phase material; consequently, it is expected that the reinforcement phase will take the vast majority of the load in the composite samples. It is worth noting that both constituent materials show some tension-compression asymmetry, with the reinforcement phase material about 20% stiffer and 32% stronger in compression than in tension. In previous studies, VeroWhitePlus has been shown to exhibit significant size effects on strength [108]. While we observe similar size effects on the tensile properties of VeroWhitePlus dog bone specimen and the compressive properties of VeroWhitePlus cellular samples with spinodal topology, we did not observe any significant size effect in our experimental results on fully dense IPC samples. We attribute this lack of size effects to the fact that all samples experience similar degree of curing regardless of feature size, as the matrix and the reinforcement phases are printed at the same time in fully dense samples, and all samples are of the same size. The conclusion is that size effects on materials properties can be ignored in the following analysis of the mechanical performance of IPC composites.

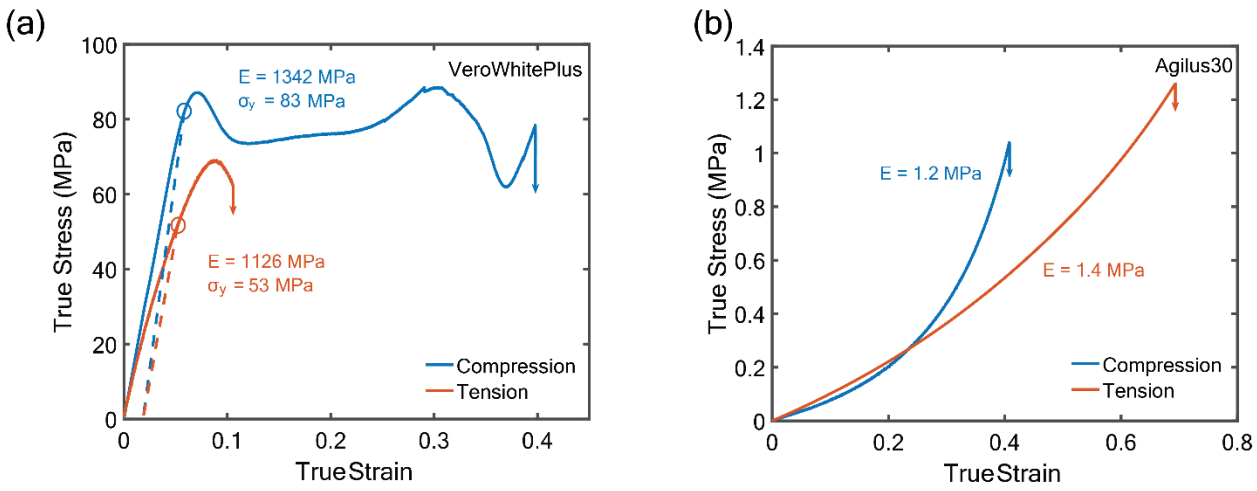

Fig. 17. *Tensile and compressive true stress – true strain curves for (a) VeroWhitePlus and (b) Agilus30.*

2.4 Spinodal IPCs: the difference between solid and shell reinforcement topologies

We start by comparing the mechanical response of IPCs with spinodal shell and spinodal solid reinforcement topologies, for volume fractions of reinforcement between 20 and 50%. Compressive stress-strain curves are obtained as explained in sec. 1.1.4, and depicted in Fig. 18a,b. While the response at low relative density is qualitatively similar, IPCs with spinodal shell topologies display a much more gradual failure as the relative density is increased, with much reduced load drops and softening at large strains. Young's modulus (E), yield strength (σ_y) and energy absorption (U) are presented as a function of the volume fraction of reinforcement in Figs. 4c,d. For IPCs with spinodal shell reinforcement, we extract the power laws $E \sim V_f^{1.4}$, $\sigma_y \sim V_f^{1.6}$ and $U \sim V_f^{1.1}$, whereas for IPCs with spinodal solid reinforcement we find $E \sim V_f^{2.2}$, $\sigma_y \sim V_f^{2.7}$ and $U \sim V_f^{1.8}$. As the hard reinforcement material is much stronger and stiffer than the rubbery matrix material (with more than three orders of magnitude difference in stiffness, see sec. 1.2), it is expected that the reinforcing phase will dominate the mechanical response of the composite;

therefore, the scaling laws obtained here can be compared to those of cellular materials, with the volume fraction of reinforcement representing the relative density, $\bar{\rho}$. For truss-based lattice materials, a scaling $E \sim \bar{\rho}^1$ and $\sigma_y \sim \bar{\rho}^1$ denote mechanically efficient stretching-dominated behavior, with $E \sim \bar{\rho}^2$ and $\sigma_y \sim \bar{\rho}^{1.5}$ indicating less efficient bending-dominated behavior [1], [2]. For spinodal cellular materials, $E \sim \bar{\rho}^{1.2}$ and $\sigma_y \sim \bar{\rho}^{1.2}$ for shell topologies and $E \sim \bar{\rho}^{2.3}$ and $\sigma_y \sim \bar{\rho}^2$ for solid topologies [53], in good agreement with the scalings found herein for composites, confirming that the reinforcement material dominates the mechanical response. The implication is that IPCs with spinodal shell reinforcement topologies are consistently superior in all metrics, with the advantage increasing significantly at lower volume fractions of reinforcement, where the thin shells with nearly zero mean curvature and negative Gaussian curvatures behave in a predominantly stretching dominated manner and deform uniformly, with little stress intensification. As V_f is increased, the topological difference between solid and shell spinodal reinforcement blurs, and the properties of the two IPCs converge. Given the consistent superior mechanical response of IPCs with spinodal shell reinforcement topology, IPCs with spinodal solid reinforcement topologies are not investigated further.

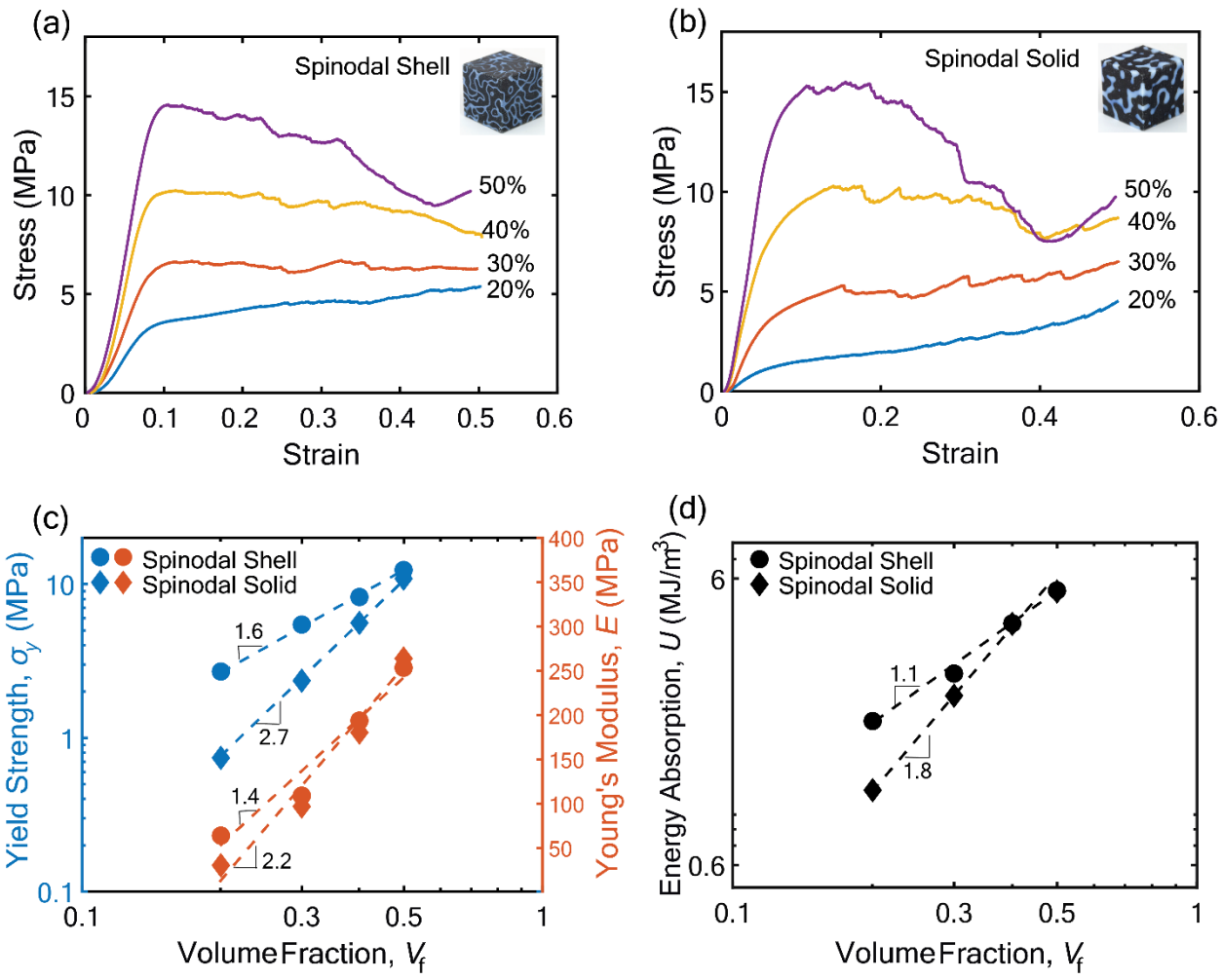

Fig. 18. *Comparison between the mechanical response of IPCs with spinodal shell reinforcement and spinodal solid reinforcement. (a, b) Compressive stress-strain curves. The volume fraction of reinforcement ranges from 20% to 50%. (a) IPCs with spinodal shell reinforcement; (b) IPCs with spinodal solid reinforcement. (c, d) Mechanical properties as a function of volume fraction of reinforcement phase: (c) Young's modulus and yield strength; (d) Energy absorption.*

2.5 The mechanical advantage of spinodal shell IPC compared to IPCs with regular reinforcement topologies

It is instructive to compare the mechanical response of IPCs with spinodal shell reinforcement topology, which is intrinsically stochastic, with that of IPCs with periodic reinforcement topologies, in particular the octet lattice topology and the Schwartz P shell topology (Fig. 16). Compressive stress-strain curves obtained over a wide range of volume fractions of reinforcement ($V_f = 5 - 50\%$) are presented in Fig. 21a,b,c. Young's modulus (E), yield strength (σ_y) and energy absorption (U) are presented as a function of V_f in Figs. 21d,e,f. While repeat tests at any single density were not conducted, the clear power-law behavior for all properties over the entire density range, with all data points narrowly banded around the average trend, confirms repeatability of the results (e.g., in the case of strength, all data fit within a 98% confidence interval). Two key results clearly emerge: (i) The mechanical properties of IPCs with these three very different reinforcement topologies (periodic truss and shell and stochastic shell) are nearly identical over the entire range of V_f, with the spinodal shell IPC performing slightly worse than the others in stiffness and strength (we attribute this to manufacturing defects, as the reinforcement shell of spinodal IPCs is thinner than that of the other two geometries at most volume fractions and is close to the resolution of the 3D printer at 5% volume fraction), and slightly better in energy absorption at high V_f; (ii) At $V_f > 35\%$, while the plastic and failure response of octet lattice and Schwartz P shell-based IPCs is qualitatively similar, and characterized by a sharp stress drop immediately after the ultimate strength, the stochastic spinodal shell-based IPC displays a much more gradual failure mechanism, characterized by a nearly flat stress plateau over the entire strain range.

The first result clearly reveals that the bicontinuous nature of the phases is more important than the specific reinforcement topology in determining stiffness, strength and failure initiation of the IPC composite. As many applications require materials to remain within the elastic regime, the implication is that the design space for stiff and strong IPCs is very broad: a wide range of topologies will result in very similar mechanical behavior. Conversely, the post-yielding deformation and failure behavior of the IPC composite (particularly at high volume fraction of reinforcement) is strongly affected by the topological arrangement of the reinforcement and matrix phases, suggesting that topology optimization would play a substantial role in design of IPCs for energy absorption and impact protection.

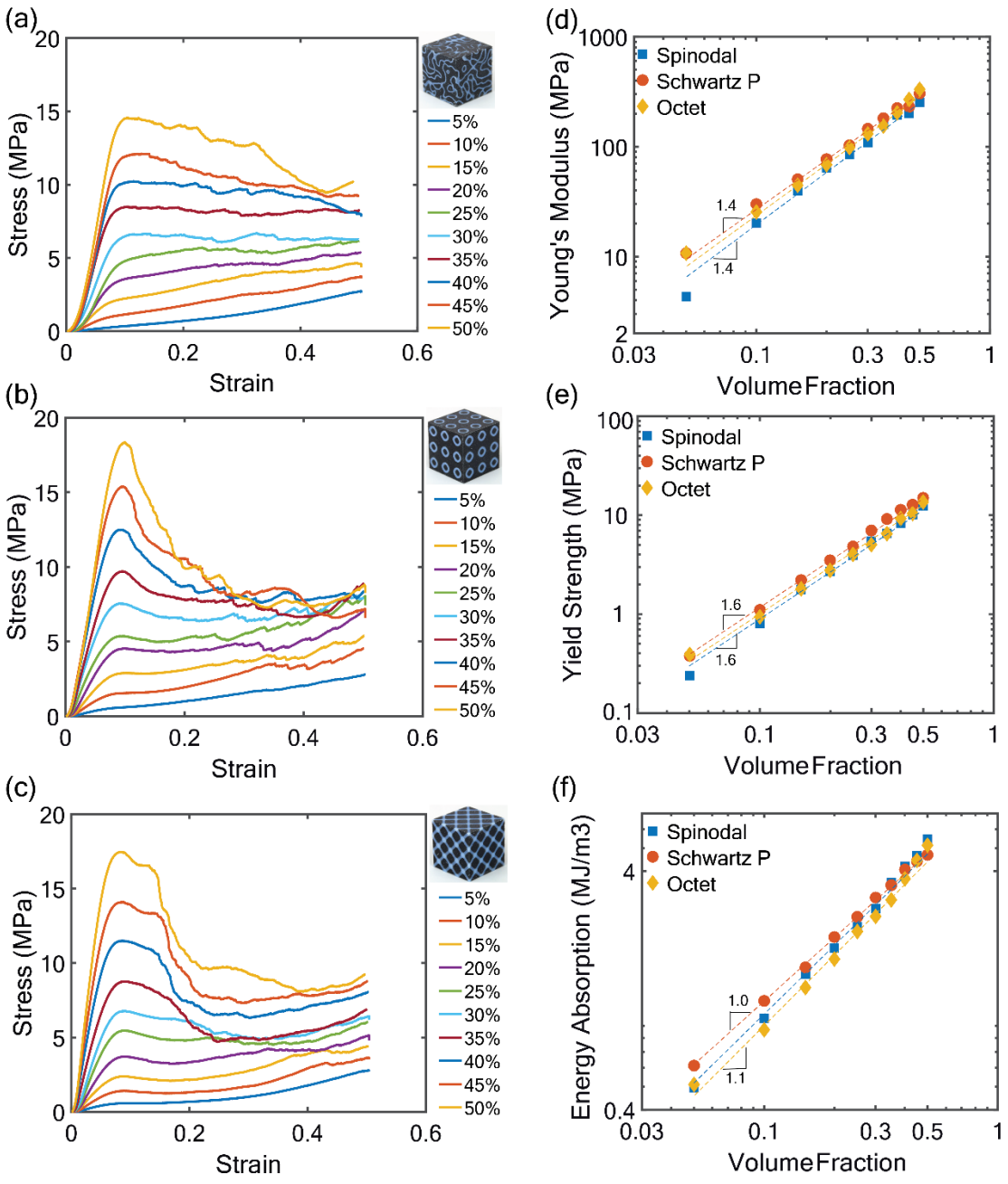

Fig. 19. *(a-c) Stress-strain curves of IPCs with different reinforcement at various volume fractions compressed to 50% strain. Spinodal shell IPCs don't have catastrophic load drop in high volume fraction. (d- f) Comparison of mechanical properties of IPCs at different reinforcement volume fraction. (d) Young's modulus; (e) yield strength; (f) energy absorption. Mechanical properties of*

spinodal IPC at 5% were excluded from the scaling as the thickness of the reinforcement shell is close to the resolution of the 3D printer and is susceptible to manufacturing defects.

To better understand this deformation and failure behavior, we compare both the stress-strain curve and deformation response of the IPCs with the three reinforcement topologies, at $V_f = 50\%$ (Fig. 20). Notice that IPCs with periodic reinforcements experience more catastrophic failure events than the spinodal shell IPC. Soon after the ultimate strength (at $\varepsilon{\sim}0.1$), cracks in the reinforcement are clearly visible in the Schwartz P shell IPC; at a strain as low as $\varepsilon{\sim}0.2$, these cracks have multiplied and aligned along a shear band, inducing catastrophic failure soon after. While cracks are not visible at the surface of the octet lattice IPC at strains as low as $\varepsilon{\sim}0.1$, presumably those cracks exist at the interior of the sample; at $\varepsilon{\sim}0.2$, alignment of cracks along a shear band is clearly visible, inducing the same catastrophic failure mechanism as in the Schwartz P shell IPC. In fact, the stress-strain curves of these two IPCs are essentially identical, throughout the entire strain range. By contrast, the stochastic spinodal shell IPC does not exhibit any visible reinforcement cracking until $\varepsilon{\sim}0.3$; even then, the cracks appear stochastically distributed across the microstructure, and not banded as for the periodic topologies. This substantial difference in the failure mechanism results in a nearly flat stress-strain curve up to $\varepsilon{\sim}0.3$, followed by a very gentle stress drop up to $\varepsilon{\sim}0.4$, when the test was interrupted.

To further investigate the damage resistance of the spinodal shell IPC, loading-unloading compression experiments were performed, whereby IPCs with the three reinforcement topologies, at $V_f = 50$, were compressed to 10% strain for three cycles (Fig. 21). As the number of cycles increases, all IPCs show increasingly visible cracks in the reinforcement phase. The Schwartz P shell IPC and the octet lattice IPC both experience decreasing load-bearing capacity as a result.

On the contrary, even with increasing visible fracture sites, the load-bearing capacity of the spinodal shell IPC is largely unaffected by the cyclic loading, demonstrating superior resistance to damage.

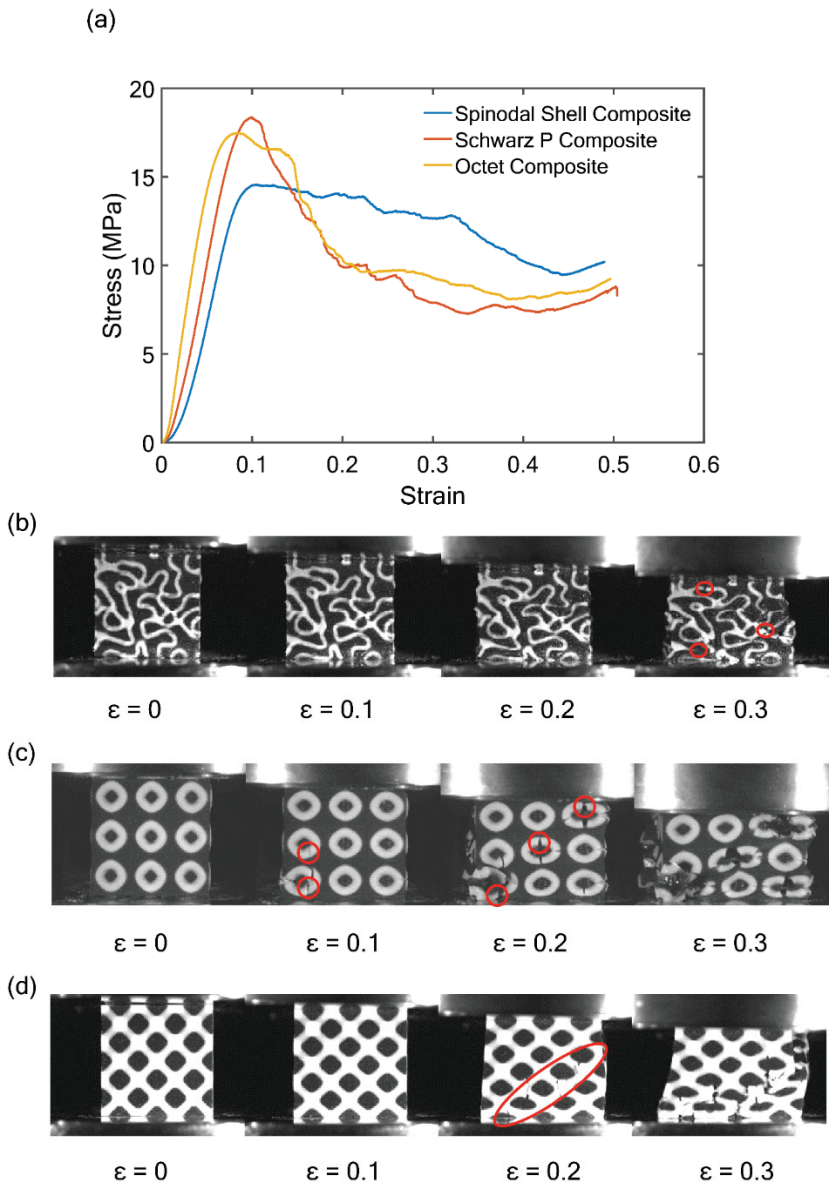

Fig. 20. *Deformation response of IPCs with different reinforcement at 50% volume fractions compressed to 50% strain. (a) Stress-strain curve. (b) Spinodal shell composites. (c) Schwartz P*

shell composites. (d) Octet lattice composites. Octet and Schwartz P IPCs at high volume fracture experience more catastrophic failures than spinodal shell IPCs.

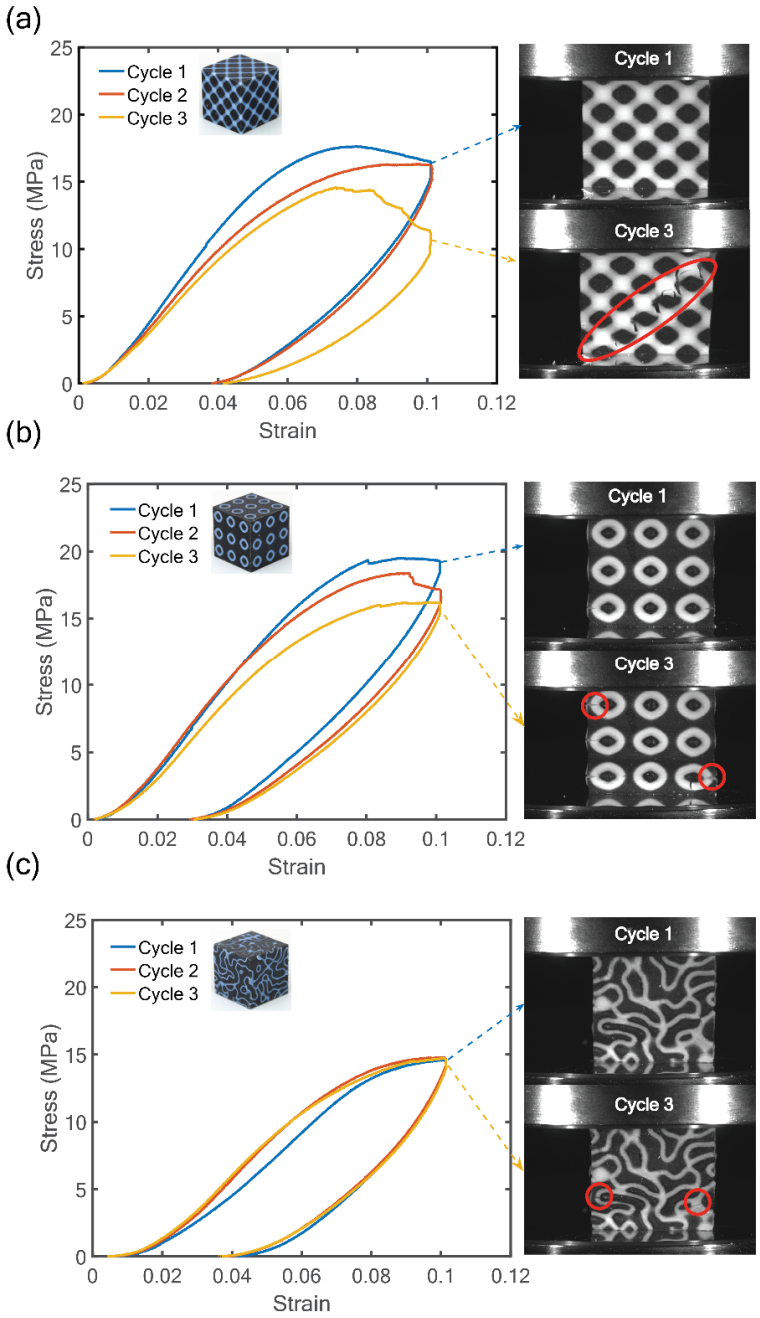

Fig. 21. *Cyclic compression experiments on IPCs with different reinforcement topologies, at 50% volume fraction of reinforcement. All samples have been compressed to 10% strain for 3 cycles.*

(a) Octet lattice composite. (b) Schwartz P shell composite. (c) Spinodal shell composite. All three topologies show increasingly visible fractures in the reinforcement phase as cycling loading progresses. Both periodic IPCs show decreasing load bearing capacity as a result, while the stress-strain curve of the spinodal shell composite is largely unaffected.

We attribute these dramatic differences in behavior to (i) the larger surface area and (ii) the stochastic nature of the spinodal shell topology. The larger surface area of the spinodal shell compared to the other two periodic geometries results in increased reinforcement/matrix interaction, with the matrix preventing/arresting crack propagation in the reinforcement phase. In addition, the stochastic nature and complex shape of the spinodal shell reinforcement distribute the loads more efficiently throughout the topology, maintaining load-bearing capacity after fracture initiation and prevents the formation of catastrophic failure-inducing crack bands. In periodic geometries like Schwartz P or octet truss, failures first occur around stress concentration locations, and subsequently band along specific directions, leading to catastrophic failure and loss of load bearing capacity. Conversely, for the stochastic spinodal shell topology, stress is more uniformly distributed across the entire structure. Even after fracture of some shell sections, the complex topology still allows the spinodal shell-reinforced composite to maintain nearly unchanged load bearing capacity.

The difference in failure response between the spinodal and the periodic reinforcement IPCs is less pronounced at low volume fractions of the reinforcement (Fig. 21), as the increased volume fraction of the matrix helps stabilize even periodic structures against crack banding the structure against banded cracking of the reinforcement.

To better understand and quantify the differences in deformation and failure behavior, finite element analyses were performed on the IPCs with the three reinforcement topologies, at a volume fraction of reinforcement $V_f = 30\%$. The results are presented in Fig. 24. Notice that the computational prediction of the stress-strain response is in good agreement with the experimental results, well capturing the initial stiffness, the yield and ultimate strength and the beginning of the post-failure behavior (Fig. 24 (a-c)). This agreement validates the computational model and provide confidence in its ability to capture the onset and early evolution of damage. As finite elements simulations involving post-failure behavior (including fracture) are very challenging because of stress singularity and loss of uniqueness, a full numerical description of the failure mechanisms all the way to densification is beyond the scope of this work. Nonetheless, several conclusions can be extracted from an analysis of the stress state at the early and intermediate phases of deformation. First, we compare the von Mises stress distribution in the reinforcement phase for all three IPCs at a strain of 0.1, roughly coinciding with the attainment of the maximum strength, in Fig 22 (d-f). It is apparent that the spinodal shell IPC shows small and randomly distributed stress concentrations throughout the sample, whereas the IPCs with the periodic reinforcement topologies exhibit very large and interconnected stress concentrations. This is consistent with the experimental findings in Fig. 22 and further supports the argument that the spinodal shell IPC is effective at avoiding catastrophic failure by preventing formation of reinforcement cracking bands. On the contrary, in IPCs with periodic reinforcement such as the octet and Schwartz P IPC, fracture of a member leads to a cascading crack propagation which results in an instant loss of load bearing capacity. We then compare the von Mises stress distribution in the reinforcement phase in the middle of the sample for all three IPCs at a strain of 0.15, when surface cracks start to appear in Fig. 24 g,h,i. It can be seen that the stress distribution of the spinodal shell IPC is still uniform and

largely unaffected by cracks, while the two periodic IPCs experience drop in load bearing capacity as a result of cracks at stress concentration points. These simulation results are also in good agreement with the cyclic experiments shown in Fig. 23 and demonstrate the excellent damage resistance of the spinodal shell IPC.

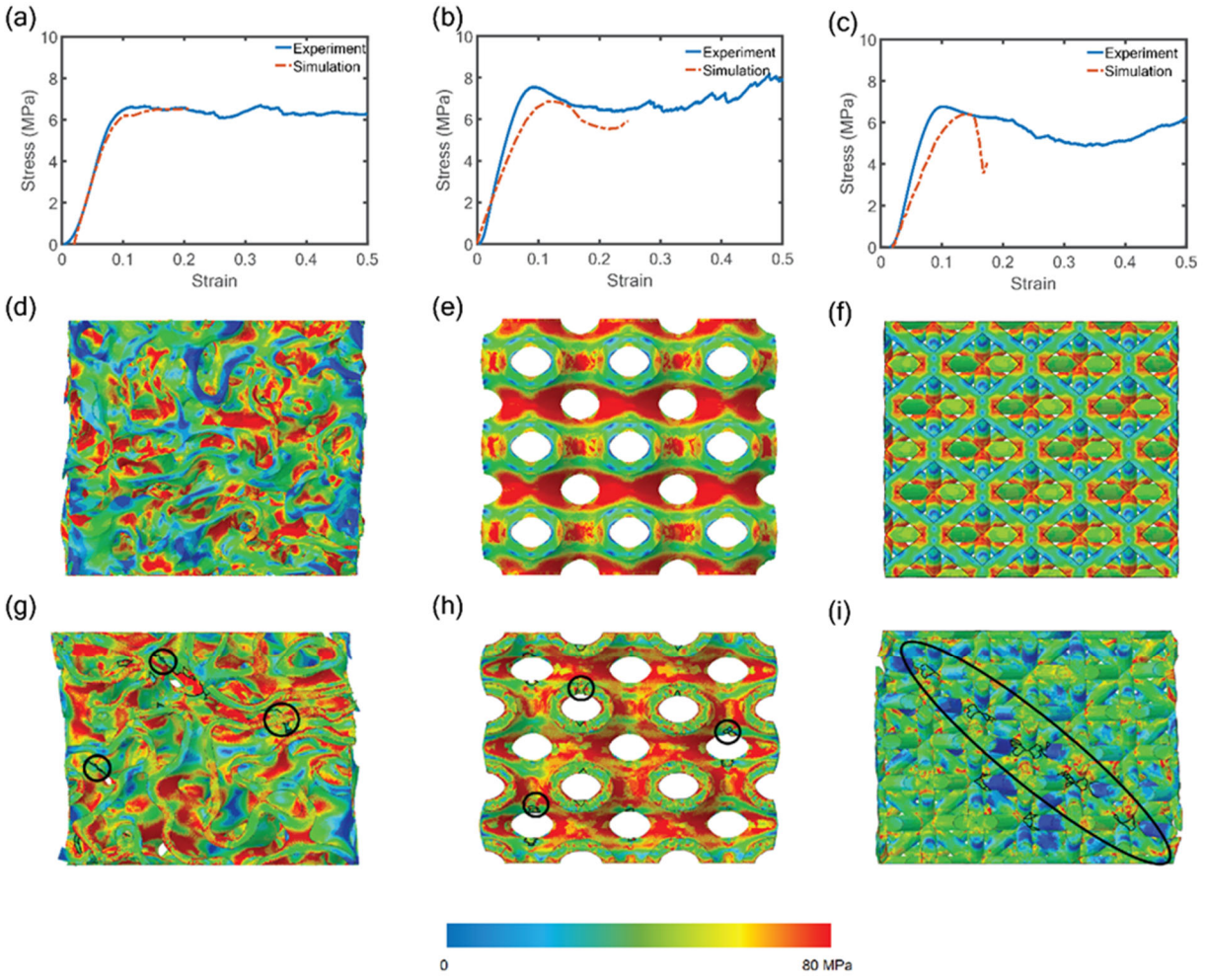

Fig. 22. *Comparison between experiment and simulation results. (a, b, c) Stress strain curve comparison between experiment and simulation at 30% volume fraction: (a) spinodal shell IPC; (b) Schwartz P IPC; (c) octet IPC. (d, e, f) von Mises stress map of the reinforcement phase extracted from the composite at 10% strain: (d) spinodal shell reinforcement; (e) Schwartz P*

reinforcement; (f) octet reinforcement. (g, h, i) von Mises stress map of the reinforcement phase at the half-way cross section, extracted from the composite at 15% strain: (g) spinodal shell reinforcement; (h) Schwartz P shell reinforcement; (i) octet lattice reinforcement. Cracks are highlighted in black.

Collectively, these experimental and numerical results clearly illustrate that the stochastic nature of spinodal shell topologies enables the establishment of a uniform stress field throughout the reinforcement, which persists even after the onset of reinforcement cracking. The lack of substantial stress intensifications promotes a stochastic distribution of initial cracking locations and prevents the catastrophic occurrence of crack banding, resulting in a flat stress plateau through very large strains. Combined with a very large interfacial area, which ensures intimate reinforcement/matrix interaction, this feature makes spinodal shell IPCs ideally suited for energy absorption and impact applications.

2.6 Influence of surface area of the reinforcement phase in IPCs

One possible reason for the unique properties of spinodal shell IPCs is the increased surface area of the spinodal shell relative to the other reinforcement topologies, which leads to increased interaction and support from the matrix. The surface area and curvature of spinodal geometry is affected by decomposition time *t*, with increasing *t* resulting in deceased surface area and curvature. The decomposition time *t* can be controlled to generate different ratio between the characteristic length over the cubic length, λ/L (Fig. 24). In all spinodal samples tested in the manuscript, $\lambda/L = 1/5$ was used as it has been shown to provide the best overall mechanical

properties to spinodal shell cellular materials [53]. The surface area of the 3D printing models for all three topologies was extracted in Netfabb, a 3D printing software, and plotted in Fig. 23. Notice that the spinodal shell topology has significantly more surface area than both Schwartz P and octet lattice topologies, especially at lower volume fractions of reinforcement. As seen in Fig. 19, even at high volume fraction, where the octet lattice has similar surface area, spinodal shell IPCs are still better at avoiding catastrophic failures and have better energy absorption as a result. This is attributed to the stochastic nature and complex shape of the spinodal shell topology.

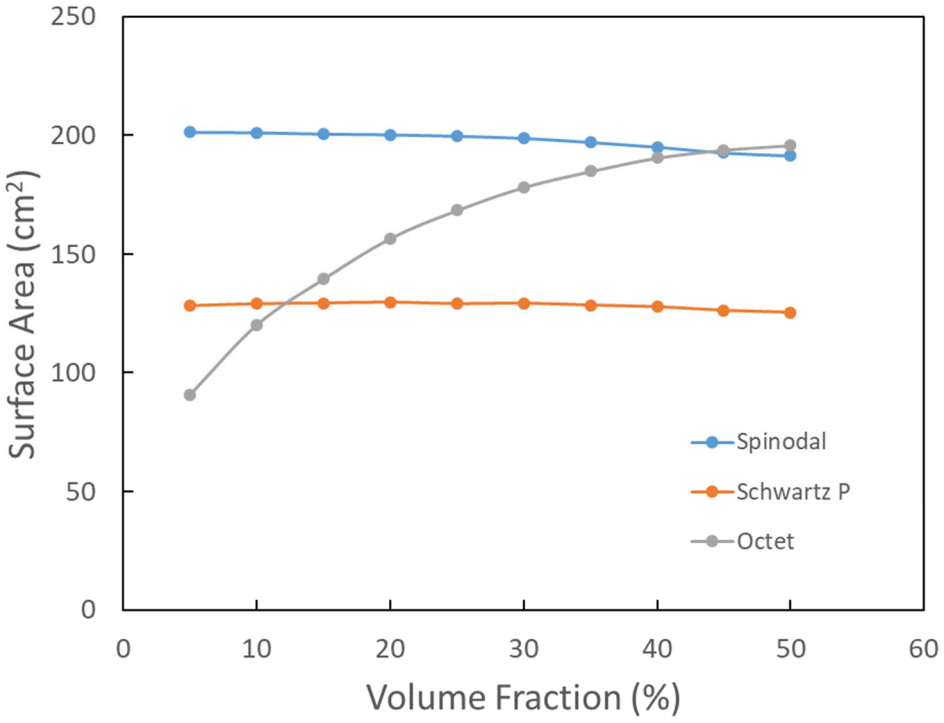

Fig. 23*. Surface area of the reinforcing phase for IPC samples with different reinforcement topologies.*

The influence of curvature and surface area on mechanical properties of spinodal shell IPCs deserves further investigation. Some preliminary results are shown in Fig. 25. Samples with $\lambda/L =$

$1/8$ have the highest surface area and curvature, while samples with $\lambda/L = 1/3$ have the lowest. It can be seen that samples with $\lambda/L = 1/8$ seem to perform slightly better mechanically than samples with $\lambda/L = 1/5$, and significantly better than samples $\lambda/L = 1/3$. One possible explanation is that samples with $\lambda/L = 1/3$ are more susceptible to defects from manufacturing. It has been found in our previous study that samples with $\lambda/L = 1/8$ are less sensitive to imperfection than samples with $\lambda/L = 1/3$ because of its increased surface area and more stochastic nature [53]. Further experiments and simulation are needed to better understand this phenomenon.

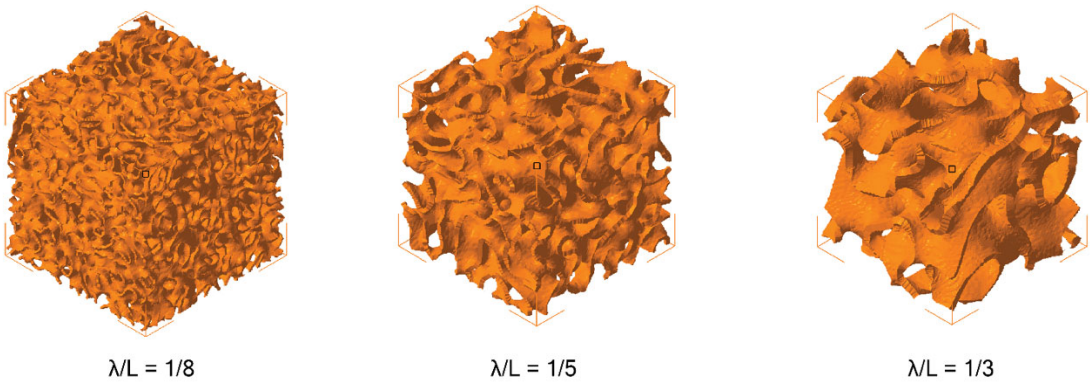

Fig. 24. *$\lambda/L = 1/8$, $\lambda/L = 1/5$ and $\lambda/L = 1/3$ spinodal shell at 30% volume fraction*

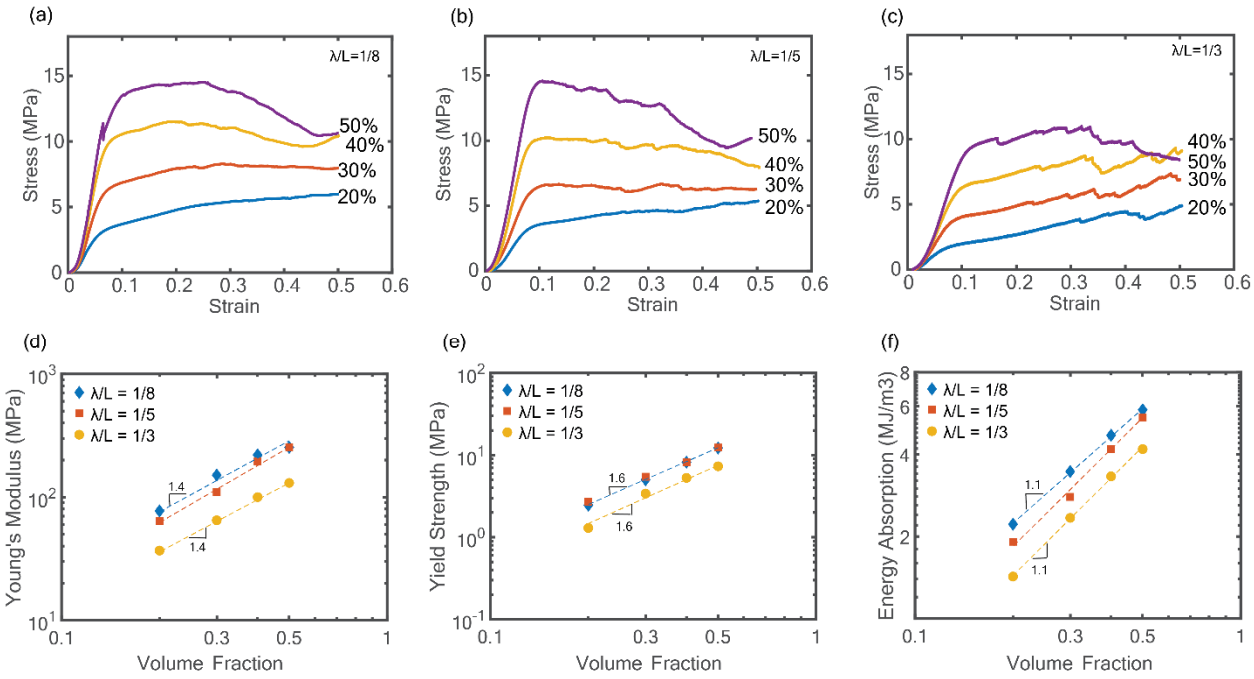

Fig. 25. *Mechanical properties of spinodal shell IPCs with different curvature/surface area. Stress-strain curves for (a)* $\lambda/L = 1/8$*; (b)* $\lambda/L = 1/5$*; (c)* $\lambda/L = 1/3$*. (d) Young's modulus. (e) Yield strength. (f) Energy absorption.*

2.7 Conclusions

In summary, we have fabricated and mechanically investigated a new type of interpenetrating phase composite (IPC) with spinodal shell reinforcement topology, comparing their mechanical response to that of well-established mechanically efficient periodic IPCs with octet lattice and Schwartz P shell reinforcement topologies. All samples were additively manufactured using multi-material jetting and tested in uniaxial compression to large deformations. Polymeric model systems were produced by Polyjet multi-material additive manufacturing; while the mechanical properties of the two polymeric phases (and hence the resulting composites) were inferior to those of any practical structural material, this technique allowed unbiased comparison of different topologies.

We have shown that while all IPCs perform nearly identically in terms of initial stiffness, yield strength and energy absorption, regardless of reinforcement topologies, over a wide range of volume fraction of reinforcement (5-50%), spinodal shell IPCs are far more robust than any other IPCs, exhibiting greater damage resistance as well as a much more uniform deformation and gradual failure. This unique feature is attributed to: (1) uniform distribution of stresses and strains in shell topologies, stemming from fairly uniform distribution of negative Gaussian curvature across the entire surface; (2) larger surface area at a given volume fraction of reinforcement, resulting in increased matrix support on the load bearing reinforcing phase; (3) the stochastic nature and complex shape of spinodal topologies, which act as crack barriers and locally inhibit crack propagation and banding, but also continue to provide load-bearing capacity even after fractures of some members occurs. The combination of excellent mechanical efficiency, on par with those of the best IPCs with periodic reinforcement, great damage resistance, gradual deformation and failure mechanisms and potential for scalable manufacturing makes spinodal shell IPCs exceptional candidates for damage tolerance and energy absorption applications where a prolonged compressive stress plateau after maximum stress is desired. While quantitative assessment of impact performance requires high-strain rate testing and are beyond the scope of this work, previous studies have demonstrated that impact performance ranking of cellular materials can be obtained by the quasi-static experiments performed in this work [109], [110]. This strongly suggests that spinodal shell IPCs would be excellent performers for impact protection.

Most importantly, unlike periodic IPCs, spinodal shell IPCs can in principle be scalably manufactured at various length scales, using self-assembly approaches followed by material conversion techniques. Possible self-assembly approaches include spinodal decomposition of block copolymers [48], interfacially jammed colloidal suspensions (bijels) [44], [49] and selective

etching of bimetallic alloys [45]. These approaches allow ready fabrication of polymeric, metallic or ceramic macro-scale samples with domain sizes at the micro or nano-scale, resulting in architected materials with enormous surface area and further improving mechanical properties by virtue of well-established size effects on the constituent materials [111]–[113]. As spinodal topologies are bicontinuous, such micro/nano-architected materials could be infiltrated with a second phase via deposition or infiltration processes, potentially providing a uniquely scalable fabrication process for shell-based IPCs.

The combination of excellent mechanical properties, on par with those of the best IPCs, gradual deformation and failure mechanisms and potential for scalable manufacturing makes spinodal shell IPCs exceptional candidates for damage tolerance and energy absorption applications.

Finally, we emphasize that, while the multi-material additive manufacturing approach used in this study resulted in polymer-polymer composites with absolute mechanical properties far inferior to those of any structural material, the self-assembly-based processes envisioned above could be used to produce ceramic-polymer, ceramic-metal, metal-polymer and metal-metal composites that can in principle outperform most existing structural materials. Demonstration and characterization of such advanced spinodal shell-based IPCs will be the subject of future studies.

Contribution statement

The work about mechanical properties of IPCs with spinodal topologies discussed in this subsection has been published [114]. The author of this thesis designed, performed and analyzed all the experiments as well as wrote the manuscript.

Chapter 3 Fracture toughness of interpenetrating phase composites (IPCs) with spinodal shell topologies

3.1 Introduction

Chapter 1 has demonstrated the remarkable mechanical efficiency of cellular materials with spinodal shell topologies, which can be attributed to the uniform stress distribution deriving from their uniform near-zero mean curvature and negative Gaussian curvature on all surfaces [95]. Chapter 2 further showed that these benefits in mechanical properties extend to spinodal shell-based IPCs, which display specific stiffness and strength on par with those of the best IPCs with periodic reinforcement, as well as very gradual deformation and failure mechanisms [114]. While one might surmise that the superior damage tolerance is related to topological mechanisms of crack deflection upon damage evolution, the fracture toughness of IPCs with shell topologies (either periodic or spinodal) has not been studied.

In this chapter, we investigate the fracture toughness of 3D printed IPCs with shell-based reinforcement topologies, including spinodal shell, Schwarz P and Gyroid (Fig. 26). Materials and manufacturing methods are identical to those used in chapter 2. The reinforcement phase in IPCs was printed in a glassy photopolymer, which is about three orders of magnitude stiffer than the matrix phase material, a rubbery polymer [114]. Singled edge notch bend (SENB) samples are tested in three-point bending to quantify the fracture properties. We demonstrate that shell-based IPCs show impressive toughening, particularly at low reinforcement volume fractions. Toughening mechanisms ranging from process zone formation, to crack bridging, crack deflection and toughening from heterogeneity[115]–[118] have been observed and have been attributed to the inherent shell-based interpenetrating architecture, and the uniform zero (or near-zero) mean curvature and negative Gaussian curvature throughout the topology. Among all three shell

topologies investigated, the spinodal shell exhibit the most significant toughening effects, a remarkable feature that we attribute to the complex structure and the stochastic nature of spinodal topologies and its ability to prevent straight crack propagation.

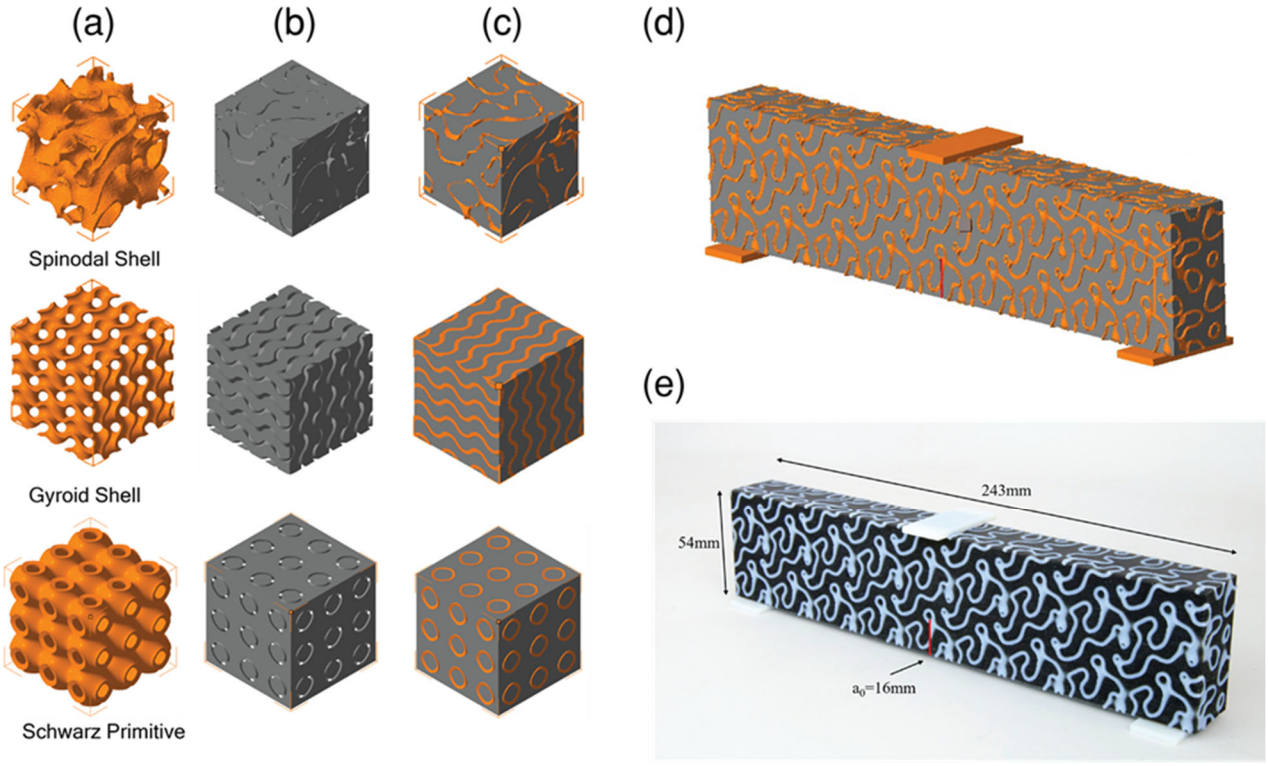

Fig. 26. *IPC topologies under consideration: (a) Reinforcement phase (3×3×3 unit cells with spinodal shell, gyroid shell and Schwartz P shell topologies), (b) matrix phase, (c) assembled interpenetrating phase composite, (d) complete single edge notched bend (SENB) sample model for spinodal shell IPC and (e) 3D printed SENB sample for spinodal shell IPC.*

3.2 Materials and methods

3.2.1 Model generation

CAD files used in manufacturing composite samples in this work were generated with the following steps: (1) A shell of each reinforcement phase topology was generated; (2) The shell

was thickened so that the resulting reinforcement phase reached a desired volume fraction; (3) The matrix phase file was generated by taking the inverse of the reinforcement phase in the same space; (4) Both the reinforcement phase file and the matrix phase file were combined in the control software of the 3D printer to manufacture the IPC composites.

To measure the Young's modulus of the composites (necessary for fracture toughness extraction from the SENB tests), cubic samples with $3 \times 3 \times 3$ unit cells were generated. All fracture toughness experiments were performed in 3-point bending, on samples with $3 \times 6 \times 27$ unit cells, conforming to ASTM standard E1820 [119] . Load spreaders were placed between the rollers and the samples to prevent local indentation.

Spinodal shell: The spinodal shell topology was generated with a two-step process: (1) A 50% dense spinodal solid topology is generated by solving the Cahn–Hilliard evolution equation [41] in space and time over a cubic domain with edge length of N using a finite difference algorithm (see section 2.21 and Appendix A for more details). The characteristic feature size (λ), which is a measure of the domain size of the topology, is controlled by the evolution time *t.* In this work, *t* was chosen so that $\lambda = \frac{1}{3}$N (loosely corresponding to a sample with $3 \times 3 \times 3$ unit cells). (2) The spinodal shell topology is extracted from the interface between the solid and void phases. The volume fraction of reinforcement, V_f, is chosen by assigning the appropriate thickness to the shell, t_s, so that $V_f = t_s A/V$, with *A* the surface area of the shell and *V* the sample volume.

Previous studies have shown that spinodal shell topologies extracted from a 50% dense spinodal solid topology have near-zero mean curvature and negative Gaussian curvature, the defining features of TPMSs. While spinodal shell topologies with non-zero mean curvature can also be

generated, their mechanical properties are generally inferior, and they won't be considered in this study [53].

Schwarz P TPMS and Gyroid TPMS: The Schwarz P surface and the Gyroid surface can be described by the following level-set equations, which approximate the implicit surfaces:

Schwarz P: $\cos(x) + \cos(y) + \cos(z) = 0$ (1)

Gyroid: $\sin(x)\cos(y) + \sin(y)\cos(z) + \cos(x)\sin(z) = 0$ (2)

where (x,y,z) is a coordinate point in three-dimensional Euclidean space. For both geometries, the minimal surfaces corresponding to the above equations were generated using the Minisurf software package, which can be used to generate CAD files for minimal surfaces [106], [120]. As explained in the generation of spinodal shell, the volume fraction of the reinforcement phase, V_f, is chosen by thickening the shell with appropriate thickness, t_s, so that $V_f = t_s A/V$, with A the surface area of the shell and V the sample volume.

3.2.2 Sample fabrication

Fracture toughness samples with the spinodal, the Schwarz P and the Gyroid shell reinforcement topologies were manufactured at 20%, 30% and 40% reinforcement volume fraction. All samples were manufactured with a multi-material 3D printer (Objet260 Connex3, Stratasys), which allows multiple photopolymers to be printed simultaneously. In this work, the reinforcement phase in IPCs was printed with VeroWhitePlus, a glassy photopolymer, while the soft matrix phase was printed with Agilus30, a rubbery polymer. Samples for uniaxial compression tests have a dimension of 27mm x 27mm x 27mm and consist of 3 x 3 x 3 unit cells. All fracture toughness

samples as shown in Fig. 26 have a dimension (not including the load spreaders) of 243mm x 54mm x 27mm, and consist of 27 x 6 x 3 unit cells. A starter notch with length of 16mm and tip with the angle of 30° was designed to promote early crack initiation. All 3D printed samples were left at room temperature for 4 days for curing.

3.2.3 Experimental characterization

All mechanical tests were performed with an Instron 8800 mechanical test frame. The mechanical properties of the constituent materials (VeroWhitePlus and Agilus 30) were already reported in Chapter 2 (see Sec. 2.3). The Young's modulus, E_{xx}, for all IPCs was extracted through uniaxial compression tests, following the ASTM 695–15 standard for compressive properties of rigid polymers [107]. A quasi-static strain rate of .0001 s^{-1} was used in all compression tests. Fracture toughness of all IPCs were determined using singled edge notch bend (SENB) samples following ASTM standard E1820 [119]. While this standard was originally introduced to measure fracture toughness of homogeneous metallic materials, in recent years it has been adopted in fracture toughness studies of many new materials, including cellular materials and composites [104], [121], [122]. The load and the load-line displacement were measured by the Instron test frame, while the crack mouth opening displacement was measured via digital image correlation (DIC). A constant displacement rate of 0.015mm/s was used for all fracture toughness tests and a frame rate of 0.25 FPS is used to take images of the samples during tests for DIC analysis. The J-integral approach was used to capture inelastic contributions to the fracture resistance using the elastic compliance method in ASTM E1820. Compliance measurements from the unloading curves are extracted manually, at intervals Δv= 1 mm for all IPC samples, respectively. Compliance along the load-line was used to calculate the current crack length, and the J-integral was calculated using the

measured applied load and crack mouth opening displacement. The fracture toughness, $K_{J(i)}$, is related to the J-integral by $K_{J(i)} = (J_{(i)}E')^{1/2}$, where E' is the plane strain Young's modulus, $E' = E_S/(1 - \nu^2)$ and ν is the Poisson's ratio. Since the IPC topologies are not necessarily isotropic, the compressive Young's modulus in the direction of the span length, E_{XX}, was used (See Appendix B for details).

3.3 Fracture behavior of shell-based IPCs

Fig. 27a compares the SENB load-displacement curves of the three shell-based topologies, spinodal shell, Schwarz P and Gyroid IPCs, at 30% reinforcement volume fraction. In the initial loading stage, load increases linearly with displacement. After the initial loading stage, all samples exhibit highly nonlinear fracture behaviors. As shown in Fig. 27(b-d), the first load drop is the result of local failure of the reinforcement phase ligament. After the first load drop, the spinodal and Gyroid IPCs the continue to experience increased load before experiencing a second larger load drop. Subsequently, the load remains nearly constant before the final failure event. On the other hand, the load in the Schwarz P IPC slightly decreases after the first load drop, before the final catastrophic load drop. These multi-stage fracture patterns can be explained by the complex and interconnected topologies of the shell-based reinforcement phases. While cracks would naturally grow through the softer matrix phase, the co-continuous nature of both the hard reinforcement phase and the soft matrix phase prevents the crack from propagating within just one phase. Therefore, when the crack tip encounters the hard reinforcement phase, the crack propagation is slowed down. Subsequent crack propagation can occur through the stronger phase or via the interface, as previously observed in [123]. The latter will require significant crack deflection, with related increase in energy cost for crack propagation.

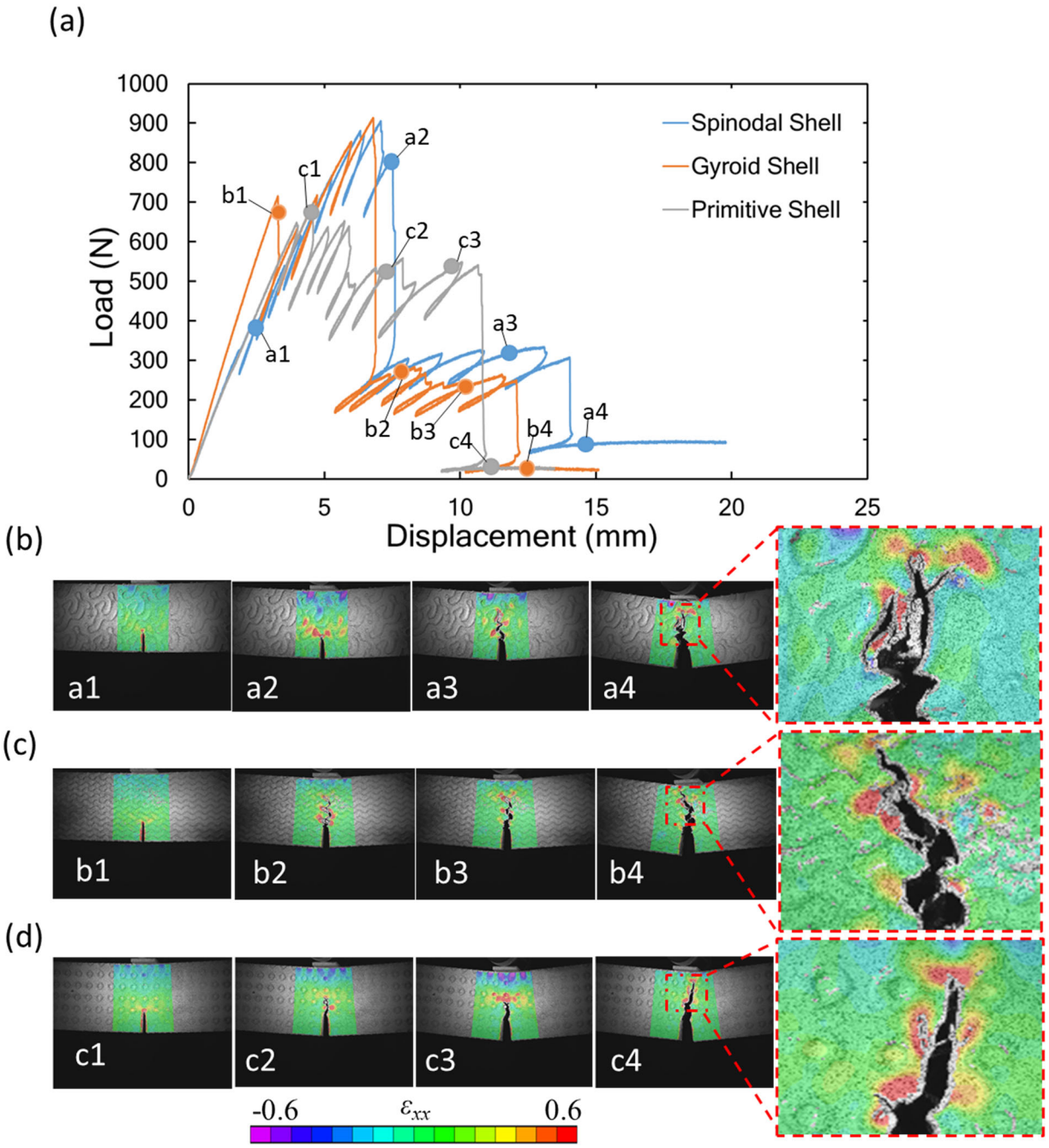

Fig. 27. *Fracture behavior of shell-based IPCs at 30% volume fraction. (a) Load displacement curves of IPCs with spinodal shell, Gyroid and Schwarz P topologies. (c)-(d) Crack propagation patterns and strain contours using digital image correlation(DIC) at various loading displacements marked on the load-displacement curves.*

3.4 Toughening mechanisms

As can be seen in Fig. 27 (b-d), several toughening mechanisms synergistically contribute to the fracture resistance of the shell-based IPCs. As a result, the crack resistance of shell-based IPCs increases as the crack propagates, resulting in improved toughness. To further analyze the fracture behavior of shell-based IPCs in a quantitative manner, R-curves for all materials are extracted and plotted. As shown in Fig. 27 (c-d), all three IPCs show increasing J-integral as cracks propagate. The spinodal shell IPC possesses both the highest absolute value of the final J-integral as well as the most dramatic increase in J-integral. By contrast, the Schwarz P IPC has the lowest absolute value of the final J-integral and least amount of increase. Notably, when converting J-integral into fracture toughness, the fracture toughness of the spinodal shell IPC becomes much closer to that of the Gyroid IPC, because of the higher stiffness of the Gyroid IPC.

Three major toughening mechanisms are synergistically responsible for the impressive fracture behavior of the shell-based IPCs. The first is the formation of a **process zone** in front of and behind the crack tip. The strain contours for all three topologies shown in Fig. 27(b-d) display formation of large areas of process zone in the form of stress concentration in front of the crack tip. This enlarging of plasticity can be attributed to both the uniform distribution of strain from the minimal surface reinforcement phase and the additional support from the matrix phase. As the crack tip passes through the process zone, the strained material behind the crack tip begin to unload elastically and dissipate energy that contribute to the toughening of the IPCs. The second major toughening mechanism is **crack bridging** by the reinforcement phase, whereby the hard polymer stretches between the two faces of the crack behind the crack tip. As clearly shown in Fig. 27b, some ligaments of the reinforcement phase begin to stretch immediately after the crack tip and continue to stretch as the crack propagates until the rupture point. Energy dissipated by the bridging

ligaments contributes to the rise of the R-curves. The third toughening mechanism responsible for the increase of fracture toughness is the extensive **crack deflection** as the crack propagates through the complex geometry. Fig. 27(b-c) clearly show that the crack path deviates from the initial crack tip and grows in an aggressive zig-zag shape. The extensive crack deflection results in highly tortuous crack path which results in increased crack surface and enhanced fracture toughness.

While the process zone formation has been observed for all three topologies on a similar scale, the crack bridging and the crack deflection appear to be significantly more pronounced in the spinodal shell IPC and the Gyroid IPC compared with the Schwarz P IPC, with the spinodal shell IPC showing slightly more extensive toughening. This explains the superior performance of the spinodal shell IPC in terms of J-integral and the similarities between the spinodal shell IPC and the Gyroid IPC in terms of R-curve patterns. The experimental observation is consistent with previously reported numerical results [124]. The significant difference in fracture behavior between the Schwarz P IPC and the spinodal shell and Gyroid IPC can be attributed to distinct stress distributions under tensile and shear loading [124]. It has been shown that for the Gyroid shell topology, because of the complex geometry, multiple higher stress bands are formed and isolated by lower stress regions, preventing a single crack from becoming dominant. On the contrary, the Schwarz P topology has continuous high stress region throughout the entire structure and fails by growth of a single nucleated crack. The further advantage of the spinodal shell IPC stems from the stochastic nature of its topology, which leads to more dramatic and less regular crack deflection as well as more crack bridging behind the crack tip .

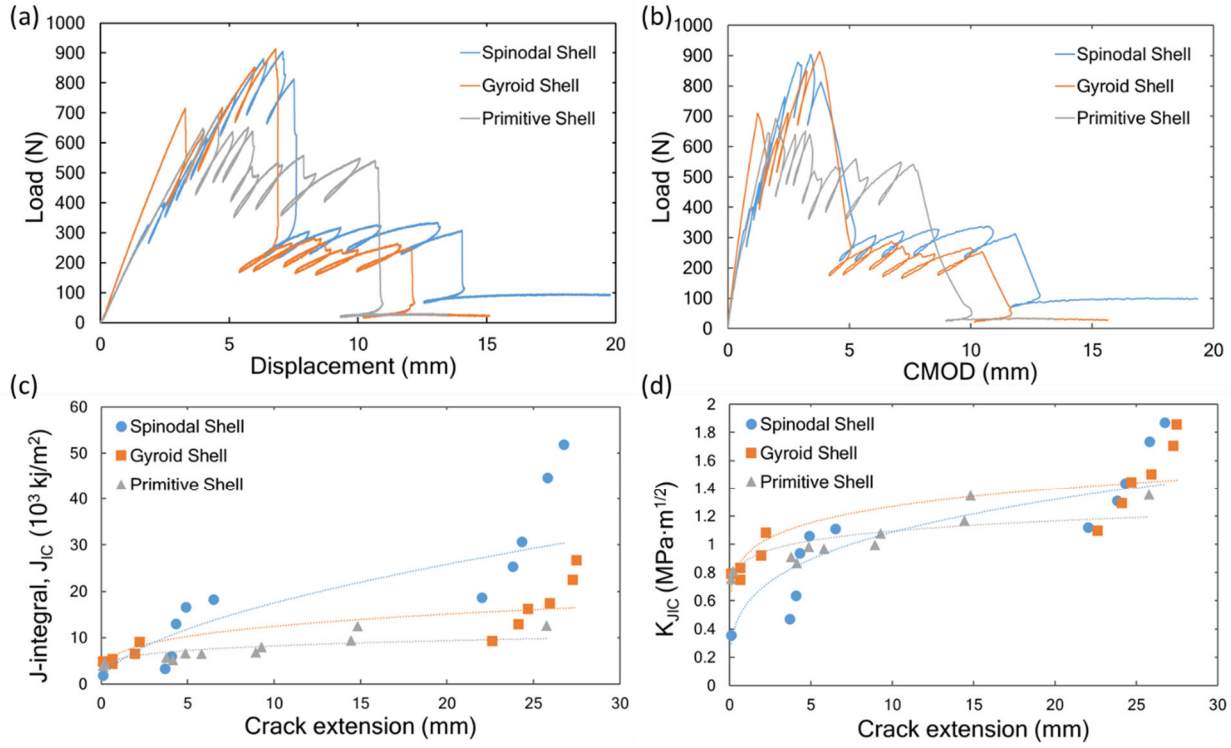

Fig. 28. *Fracture response of shell-based IPCs with spinodal shell, Gyroid shell and Schwarz P topologies. (a) Load-displacement curves. (b) Load as a function of the crack mouth opening (CMOD). (c) J-integral, J_{IC} and (b) fracture toughness K_{JIC} are plotted as a function of crack extension. Dotted lines through the data points are fitted using a power function and added to aid the readers.*

It is worth noting that while the R-curve of the Schwarz P IPC shows a slightly rising shape commonly observed in most traditional monolithic material and composites, both the load-displacement curves and the R-curves of the spinodal shell IPC and Gyroid shell IPC exhibit a stepped shape as shown in Fig. 28. This is the result of the crack repeatedly switching propagation through the hard phase and the soft phase. When the crack tip penetrates a ligament of the hard phase, the sample experiences an instantaneous load drop. Part of the released strain energy is dissipated by the breakage of the hard phase, while the rest of the strain energy drives a rapid crack

propagation, as previously observed [125]. This crack propagation is slowed down by other toughening mechanisms, including process zone formation, crack bridging and crack deflection along the interface, and is eventually stopped when the crack encounters another hard ligament. Since breaking of the hard phase requires extra energy, the R-curve rises sharply (Fig. 28 c-d). In summary, the spinodal shell IPC and the Gyroid IPC are toughened by cycles of (1) rapid dynamic crack growth driven by released energy from breaking of a hard ligament, (2) crack growth slowed by toughening mechanisms, including process zone formation, crack bridging and crack deflection, (3) arrest of crack propagation when the crack encounters the next hard ligament, (4) increase in load and energy until fracture of the next hard layer, after which the next cycle starts.

Although only two such cycles can be observed in samples studied in this work due to sample size limitations imposed by manufacturing technique, it has been found that such step shaped R-curves are commonly observed in heterogeneous materials [115], [126] where crack propagates through alternation of hard and soft phases. The toughening effect of heterogeneity can be classified into two categories: (1) Effect of the spatial material property variation, in this case Young's modulus, in the crack path. This effect has been shown to improve the fracture toughness of a composite compared with a homogeneous material. This is a result of crack arrest when the crack tip is in the weaker phase due to strong decrease in crack driving force after the crack penetrates the stronger phase [116], [117]. (2) Effect of increased fracture surface due to crack propagating in a tortuous path along the interface of the two phases. It has been shown that when propagating in a composite with a hard phase and a soft phase with a complex geometry, the crack tends to follow the contour of the hard phase [123], [126]. The resulting crack path is highly tortuous (Fig. 26 b-c), which leads to very rough crack surface (Fig. 29d) and correspondingly increased fracture toughness[123]. For the shell-based IPCs, the smooth surface and complex structures further

increases the crack path and crack deflection, and therefore amplifying the toughening effect of heterogeneity.

3.5 Effect of reinforcement phase volume fraction

It has been shown here that the inherent architecture of the IPC reinforcement phase has significant influence on the IPC's fracture behavior (as also observed in [121], [123], [127], [128]). Here we investigate the effect of relative density on the fracture toughness. Since the spinodal shell IPC has been demonstrated to exhibit the most significant toughening, as well as having the potential of being scalably manufactured by self-assembly techniques, the discussion will exclusively focus on the spinodal shell IPC. For completeness, the results for the other topologies are reported in Appendix C. Fig. 29a shows the force-displacement curves of spinodal shell IPC SENB specimens at different volume fractions. As the volume fraction of the reinforcement phase increases, both the initial slope and the maximum load increase, resulting in higher stiffness and strength. However, it is worth noting that the samples experience larger load drops as the reinforcement volume fraction increases, a clear sign of increase in brittleness and more catastrophic failure events. At 40% reinforcement volume fraction, the sample exhibits unstable crack growth and loses its entire load bearing capacity after the first major failure event. This suggests that the spinodal shell IPC becomes more brittle as the reinforcement volume fraction increases. This decrease of toughening with increase of hard phase volume fraction is further evidenced by the laser scan images of post-mortem samples at different volume fractions (Fig. 29 c-d). At 20% volume fraction, the crack path clearly follows the contour of the reinforcing spinodal shell topology, leading to more tortuous crack path and greater crack surface with aggressive intrusion and extrusion. At 30% volume fraction, the crack path still shows extensive crack deflection, but

becomes less tortuous. The crack surface is rough as a result of the crack deflection but shows no sign of large intrusion or extrusion. At 40% volume fraction, the crack path is almost a straight line with only one noticeable crack deflection at the site of the first ligament failure. The crack surface becomes much smoother as a result. We attribute this effect to the increase of shell thickness at higher volume fractions. As the reinforcement volume fraction increases, the shell becomes thicker and requires higher load and more energy for the crack to penetrate. When the first major ligament breakage happens, the crack driving force is still very high, which leads to rapid crack growth through the entire sample.

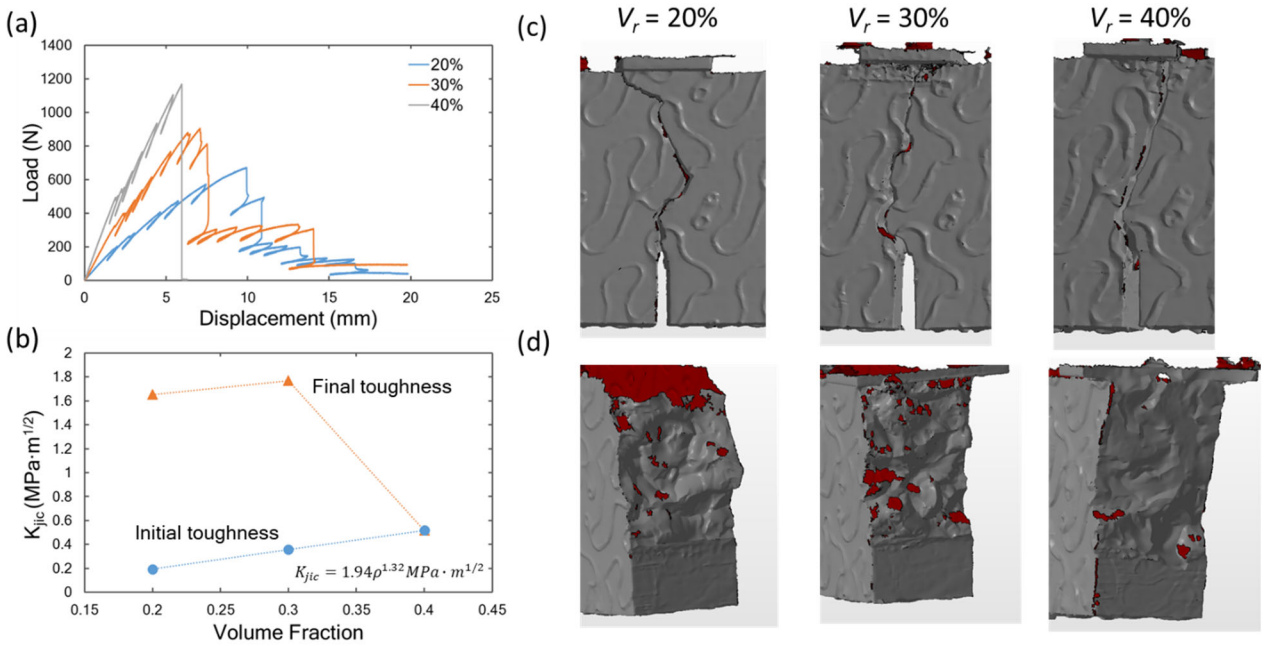

Fig. 29. *The effect of reinforcement volume fraction on the fracture behavior of spinodal shell IPC. (a) Load-displacement lines of spinodal shell IPC at different volume fraction. (b) Calculated initial and final fracture toughness with different volume fractions. Laser scan images of the samples with different reinforcement volume fractions after the test showing (c) the crack path and (d) the crack surface.*

Fig. 29b reports the initial fracture toughness, i.e., the fracture toughness at zero crack extension, and final fracture toughness, i.e., the fracture toughness after the final failure event, for the spinodal shell IPC at different volume fractions. As the volume fraction increases, the spinodal shell IPC exhibits a higher initial fracture toughness. This is because the load is primarily carried by the reinforcement phase. Therefore, composite with a higher reinforcement volume fraction shows higher stiffness and strength. The final fracture toughness also increases as the volume fraction increases, although at a slower pace, indicating decreasing toughening effects. At 40% volume fraction, the final fracture toughness converges with the initial toughness because of the unstable crack growth.

For cellular materials, the relation between the effective elastic properties such as Young's modulus E and the relative density $\bar{\rho}$ can be described by a power law E ~ $\bar{\rho}^n$[2]. Similarly, the scaling law that can be used to describe the relation between the fracture toughness and the reinforcement volume fraction can be written as $K_{jic} = C\bar{\rho}^n$. For the spinodal shell IPC, the scaling coefficient *n* calculated from the experimental data is 1.32, indicating a nearly linear relationship between the fracture toughness of spinodal shell IPC and its reinforcement volume fraction (Fig. 29 b). It is worth noting that, while the multi-material 3D printing technique used in this study resulted in polymer-polymer composites with worse absolute mechanical properties than those of any structural material, the spinodal shell IPC has the potential to be manufactured in a self-assembly manner to produce ceramic-polymer, ceramic-metal, metal-polymer and metal-metal composites that has lightweight matrix and strong reinforcement phase. Therefore, the nearly linear scaling relationship, along with the increased toughening observed at lower volume fraction, suggests the potential of manufacturing composites with high toughness and low density in an

industrial scale through self-assembly. Similar effect of reinforcement volume fraction has been observed for both the Schwarz P and the Gyroid IPC, see Appendix C for details.

3.6 Shell-based IPCs exhibit larger toughening than truss-based IPCs

Despite the increasing research interest in shell-based architected materials in recent years, most past studies on fracture toughness of architected materials focused on truss-based architected materials. Recently, hell-based architected materials with minimal surface topologies, such as triply periodic minimal surfaces (TPMS), have been shown to possess better mechanical properties, including stiffness, strength and toughness, relative to their truss-based counterparts [34], [37]. But to the best of our knowledge, this is the first study that reports on the fracture toughness of shell-based architected materials. Therefore, it is instructive to compare the fracture behaviors of shell-based IPCs with truss-based IPCs. In a recent study, truss-based IPCs were manufactured and tested in three-point bending with similar procedures [121]. By comparing the relative increase of fracture toughness, shell-based IPCs exhibit significantly higher amount of toughening compared with truss-based IPCs (Fig. 30). Shell-based IPCs have also shown much more pronounced toughening mechanisms with extensive crack deflection and highly tortuous crack path by comparing crack images at the final loading stage. We attribute the impressive fracture behavior of shell-based IPCs to their smooth surface and complex topologies.

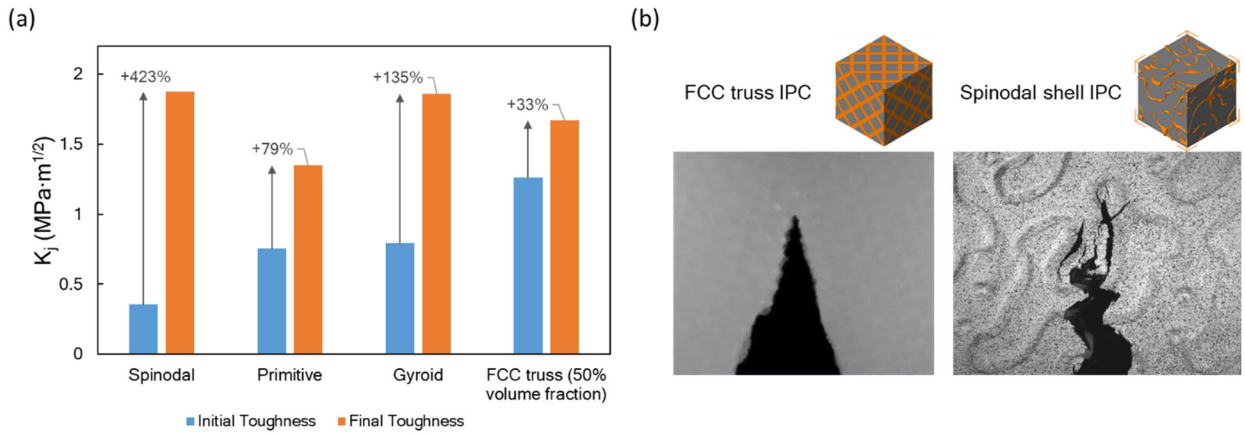

Fig. 30. *Comparison between shell-based IPCs and truss-based IPCs. (a) Comparison of initial fracture toughness, defined as the fracture toughness at zero crack extension, and final toughness, defined as the fracture toughness after the final failure event. Percentage indicates the increase of toughness from the initial loading phase to the final loading phase. (b) Comparison of the crack path image after the final failure event.*

3.7 Conclusions

In summary, through three-point bending fracture tests of 3D printed samples, we demonstrated that shell-based IPCs possess impressive fracture toughness and R-curve, which are the result of synergistic contributions from multiple toughening mechanisms, including process zone formation, crack bridging, crack deflection and toughening from heterogeneity. The spinodal shell IPC has been shown to exhibit the most significant resistance to fracture propagation. We attribute this to the complex and stochastic topology, which facilitates more extensive crack deflection and highly tortuous crack paths. As the reinforcement volume fraction decreases, the initial fracture toughness decreases linearly with the volume fraction, while the toughening effects increase. This behavior, coupled with the spinodal shell IPC's potential for scalable manufacturing via self-

assembly, opens venues to manufacturing advanced lightweight composites with superior fracture toughness at large scales, thus making the spinodal shell composite exceptionally promising for industrial applications.

While the samples in this study are polymer/polymer composite with inferior mechanical properties compared with any structural materials, the significant difference in mechanical properties between the two constituent materials allows the mechanical understanding of this study to be applied to other composites made of superior engineering materials including metal/ceramic composites. Ongoing and future research involves numerical simulation aimed at better understanding of the crack evolution in relation to the reinforcement phase of shell-based IPCs.

Chapter 4 Summary and Conclusions

One of the most effective strategies to obtain superior mechanical properties and low density is to design architected materials combining optimized topologies and constituent materials which exploit size effects at the micro/nano scale. Notable examples of such designs include micro/nano-lattices with stretch-dominated truss-based topologies[4], [6]–[8]. In recent years, shell-based topologies with triply periodic minimal surfaces (TPMS) have drawn increasing research interest and have been shown to possess better mechanical properties than their truss-based counterparts. However, due to their periodic nature, architected materials with such topologies are generally difficult to manufacture in a scalable manner. Architected materials with spinodal topologies are topologically similar to TPMS-based materials and can be manufactured through highly scalable self-assembly processes with a variety of constituent materials. In this thesis, we experimentally investigated the mechanical properties of spinodal shell-based architected materials manufactured through both additive manufacturing and self-assembly approaches, including stiffness, strength and fracture toughness. The key conclusions of this thesis are summarized as follows.

In the first chapter, we performed an experimental investigation on the mechanical properties of cellular materials with spinodal topologies manufactured through both additive manufacturing and self-assembly. Uniaxial compression tests of both spinodal shell and solid topologies manufactured through two-photon polymerization direct laser writing (TPP-DLW) experimentally verified the simulation results, demonstrating that spinodal shell topologies are remarkably efficient and imperfection insensitive. We performed systematic characterization of the mechanical properties of the acrylate-based resin IP-Dip used in TPP-DLW process and looked into the effect of thermal post-curing on its mechanical properties. Nanoindentation of macroscopic graphene pillars with spinodal shell microstructures manufactured through the highly

scalable bicontinuous interfacially jammed emulsion gels (bijels) process revealed a Young's modulus of 30 MPa, one of the highest recorded for sp^2 carbon in a porous structure [129], [130]. The study also demonstrated the amenity of spinodal structures to scalable self-assembly manufacturing.

In the second chapter, we fabricated and mechanically investigated a new type of interpenetrating phase composite (IPC) with spinodal shell reinforcement topology, comparing their mechanical response to that of well-established mechanically efficient periodic IPCs with octet lattice and Schwartz P shell reinforcement topologies. All samples were additively manufactured using multi-material jetting and tested in uniaxial compression to large deformations. We have shown that while all IPCs perform nearly identically in terms of initial stiffness, yield strength and energy absorption, regardless of reinforcement topologies, over a wide range of volume fraction of reinforcement (5-50%), spinodal shell IPCs are far more robust than any other IPCs, exhibiting a much more uniform deformation and gradual failure. This unique feature is attributed to: (1) uniform distribution of stresses and strains in shell topologies, stemming from fairly uniform distribution of negative Gaussian curvature across the entire surface; (2) larger surface area at a given volume fraction of reinforcement, resulting in increased matrix support on the load bearing reinforcing phase; (3) the stochastic nature and complex shape of spinodal topologies, which act as crack barriers and locally inhibit crack propagation and banding.

In the third chapter, we experimentally investigated the fracture toughness of 3D printed IPCs with shell-based reinforcement topologies, including spinodal shell, Schwarz P and Gyroid. Singled edge notch bend (SENB) samples were tested in three-point bending tests to quantify the fracture properties. We demonstrated that shell-based IPCs possess intriguing toughening mechanisms, including process zone formation, crack bridging, crack deflection and toughening from

heterogeneity, especially at lower reinforcement volume fractions. These mechanisms have been attributed to the smooth shell-based interpenetrating architecture, possessing near-zero mean curvature and negative Gaussian curvature. Among all three shell topologies investigated, the spinodal shell exhibit the most significant toughening effects, by virtue of their stochastic architecture.

References

[1] N. A. Fleck, V. S. Deshpande, and M. F. Ashby, "Micro-architectured materials: past, present and future," *Proc. R. Soc. Lond. Math. Phys. Eng. Sci.*, vol. 466, no. 2121, pp. 2495–2516, Sep. 2010, doi: 10.1098/rspa.2010.0215.

[2] L. J. Gibson and M. F. Ashby, *Cellular Solids: Structure and Properties*. Cambridge University Press, 1999.

[3] E. Arzt, "Size effects in materials due to microstructural and dimensional constraints: a comparative review," *Acta Mater.*, vol. 46, no. 16, pp. 5611–5626, Oct. 1998, doi: 10.1016/S1359-6454(98)00231-6.

[4] J. Bauer, A. Schroer, R. Schwaiger, and O. Kraft, "Approaching theoretical strength in glassy carbon nanolattices," *Nat. Mater.*, vol. 15, no. 4, Art. no. 4, Apr. 2016, doi: 10.1038/nmat4561.

[5] T. A. Schaedler *et al.*, "Ultralight Metallic Microlattices," *Science*, vol. 334, no. 6058, pp. 962–965, Nov. 2011, doi: 10.1126/science.1211649.

[6] L. R. Meza, S. Das, and J. R. Greer, "Strong, lightweight, and recoverable three-dimensional ceramic nanolattices," *Science*, vol. 345, no. 6202, pp. 1322–1326, Sep. 2014, doi: 10.1126/science.1255908.

[7] S. N. Khaderi, V. S. Deshpande, and N. A. Fleck, "The stiffness and strength of the gyroid lattice," *Int. J. Solids Struct.*, vol. 51, no. 23, pp. 3866–3877, Nov. 2014, doi: 10.1016/j.ijsolstr.2014.06.024.

[8] S. N. Khaderi *et al.*, "The indentation response of Nickel nano double gyroid lattices," *Extreme Mech. Lett.*, vol. 10, pp. 15–23, Jan. 2017, doi: 10.1016/j.eml.2016.08.006.

[9] D. R. Clarke, "Interpenetrating Phase Composites," *J. Am. Ceram. Soc.*, vol. 75, no. 4, pp. 739–758, 1992, doi: 10.1111/j.1151-2916.1992.tb04138.x.

[10] L. D. Wegner and L. J. Gibson, "The mechanical behaviour of interpenetrating phase composites – I: modelling," *Int. J. Mech. Sci.*, vol. 42, no. 5, pp. 925–942, May 2000, doi: 10.1016/S0020-7403(99)00025-9.

[11] R. Jhaver and H. Tippur, "Processing, compression response and finite element modeling of syntactic foam based interpenetrating phase composite (IPC)," *Mater. Sci. Eng. A*, vol. 499, no. 1, pp. 507–517, Jan. 2009, doi: 10.1016/j.msea.2008.09.042.

[12] D. W. Abueidda, A. S. Dalaq, R. K. Abu Al-Rub, and I. Jasiuk, "Micromechanical finite element predictions of a reduced coefficient of thermal expansion for 3D periodic architectured interpenetrating phase composites," *Compos. Struct.*, vol. 133, pp. 85–97, Dec. 2015, doi: 10.1016/j.compstruct.2015.06.082.

[13] J.-H. Lee, L. Wang, M. C. Boyce, and E. L. Thomas, "Periodic Bicontinuous Composites for High Specific Energy Absorption," *Nano Lett.*, vol. 12, no. 8, pp. 4392–4396, Aug. 2012, doi: 10.1021/nl302234f.

[14] A. Agarwal, I. V. Singh, and B. K. Mishra, "Numerical prediction of elasto-plastic behaviour of interpenetrating phase composites by EFGM," *Compos. Part B Eng.*, vol. 51, pp. 327–336, Aug. 2013, doi: 10.1016/j.compositesb.2013.03.022.

[15] Y. Chen and L. Wang, "Periodic co-continuous acoustic metamaterials with overlapping locally resonant and Bragg band gaps," *Appl. Phys. Lett.*, vol. 105, no. 19, p. 191907, Nov. 2014, doi: 10.1063/1.4902129.

[16] G. Li *et al.*, “Simulation of damage and failure processes of interpenetrating SiC/Al composites subjected to dynamic compressive loading,” *Acta Mater.*, vol. 78, pp. 190–202, Oct. 2014, doi: 10.1016/j.actamat.2014.06.045.
[17] G. Del Frari, S. Shadlou, and L. D. Wegner, “Comparison of the elastic and plastic behaviours of two interpenetrating phase composites with HCP inspired morphologies,” *Int. J. Mech. Sci.*, vol. 186, p. 105891, Nov. 2020, doi: 10.1016/j.ijmecsci.2020.105891.
[18] L. Xie *et al.*, “Enhancement of toughness of SiC through compositing SiC–Al interpenetrating phase composites,” *Nanotechnology*, vol. 31, no. 13, p. 135706, Jan. 2020, doi: 10.1088/1361-6528/ab6468.
[19] M. Kouzeli and D. C. Dunand, “Effect of reinforcement connectivity on the elasto-plastic behavior of aluminum composites containing sub-micron alumina particles,” *Acta Mater.*, vol. 51, no. 20, pp. 6105–6121, Dec. 2003, doi: 10.1016/S1359-6454(03)00431-2.
[20] Y. Chen *et al.*, “Preparation, microstructure and deformation behavior of Zr-based metallic glass/porous SiC interpenetrating phase composites,” *Mater. Sci. Eng. A*, vol. 530, pp. 15–20, Dec. 2011, doi: 10.1016/j.msea.2011.08.063.
[21] Y. Qi, G. Chen, Z. Li, L. Chen, W. Han, and Z. Du, “A novel approach to fabricate ceramic/metal interpenetrating phase composites by ultrasonic-assisted spontaneous infiltration,” *Ceram. Int.*, Sep. 2020, doi: 10.1016/j.ceramint.2020.09.121.
[22] I. V. Okulov, P.-A. Geslin, I. V. Soldatov, H. Ovri, S.-H. Joo, and H. Kato, “Anomalously low modulus of the interpenetrating-phase composite of Fe and Mg obtained by liquid metal dealloying,” *Scr. Mater.*, vol. 163, pp. 133–136, Apr. 2019, doi: 10.1016/j.scriptamat.2019.01.017.
[23] S. Liu, A. Li, and P. Xuan, “Mechanical behavior of aluminum foam/polyurethane interpenetrating phase composites under monotonic and cyclic compression,” *Compos. Part Appl. Sci. Manuf.*, vol. 116, pp. 87–97, Jan. 2019, doi: 10.1016/j.compositesa.2018.10.026.
[24] Y. Zheng *et al.*, “Synthesis and mechanical properties of TiC-Fe interpenetrating phase composites fabricated by infiltration process,” *Ceram. Int.*, vol. 44, no. 17, pp. 21742–21749, Dec. 2018, doi: 10.1016/j.ceramint.2018.08.268.
[25] S. Liu, A. Li, S. He, and P. Xuan, “Cyclic compression behavior and energy dissipation of aluminum foam–polyurethane interpenetrating phase composites,” *Compos. Part Appl. Sci. Manuf.*, vol. 78, pp. 35–41, Nov. 2015, doi: 10.1016/j.compositesa.2015.07.016.
[26] A. V. Okulov, A. S. Volegov, J. Weissmüller, J. Markmann, and I. V. Okulov, “Dealloying-based metal-polymer composites for biomedical applications,” *Scr. Mater.*, vol. 146, pp. 290–294, Mar. 2018, doi: 10.1016/j.scriptamat.2017.12.022.
[27] P. Agrawal and C. T. Sun, “Fracture in metal–ceramic composites,” *Compos. Sci. Technol.*, vol. 64, no. 9, pp. 1167–1178, Jul. 2004, doi: 10.1016/j.compscitech.2003.09.026.
[28] J. Zhu, F. Wang, Y. Wang, B. Zhang, and L. Wang, “Interfacial structure and stability of a co-continuous SiC/Al composite prepared by vacuum-pressure infiltration,” *Ceram. Int.*, vol. 43, no. 8, pp. 6563–6570, Jun. 2017, doi: 10.1016/j.ceramint.2017.02.085.
[29] B. G. Compton and J. A. Lewis, “3D-Printing of Lightweight Cellular Composites,” *Adv. Mater.*, vol. 26, no. 34, pp. 5930–5935, 2014, doi: 10.1002/adma.201401804.
[30] X. Wang, M. Jiang, Z. Zhou, J. Gou, and D. Hui, “3D printing of polymer matrix composites: A review and prospective,” *Compos. Part B Eng.*, vol. 110, pp. 442–458, Feb. 2017, doi: 10.1016/j.compositesb.2016.11.034.

[31] S. Hong *et al.*, "3D Printing of Highly Stretchable and Tough Hydrogels into Complex, Cellularized Structures," *Adv. Mater.*, vol. 27, no. 27, pp. 4035–4040, 2015, doi: 10.1002/adma.201501099.
[32] A. H. Schoen, "Infinite periodic minimal surfaces without self-intersect." NASA Technical Note D-5541, 1970.
[33] S. Rajagopalan and R. A. Robb, "Schwarz meets Schwann: Design and fabrication of biomorphic and durataxic tissue engineering scaffolds," *Med. Image Anal.*, vol. 10, no. 5, pp. 693–712, Oct. 2006, doi: 10.1016/j.media.2006.06.001.
[34] C. Bonatti and D. Mohr, "Mechanical performance of additively-manufactured anisotropic and isotropic smooth shell-lattice materials: Simulations & experiments," *J. Mech. Phys. Solids*, vol. 122, pp. 1–26, Jan. 2019, doi: 10.1016/j.jmps.2018.08.022.
[35] L. Wang, J. Lau, E. L. Thomas, and M. C. Boyce, "Co-Continuous Composite Materials for Stiffness, Strength, and Energy Dissipation," *Adv. Mater.*, vol. 23, no. 13, pp. 1524–1529, Apr. 2011, doi: 10.1002/adma.201003956.
[36] A. S. Dalaq, D. W. Abueidda, and R. K. Abu Al-Rub, "Mechanical properties of 3D printed interpenetrating phase composites with novel architectured 3D solid-sheet reinforcements," *Compos. Part Appl. Sci. Manuf.*, vol. 84, pp. 266–280, May 2016, doi: 10.1016/j.compositesa.2016.02.009.
[37] O. Al‐Ketan, R. K. A. Al‐Rub, and R. Rowshan, "Mechanical Properties of a New Type of Architected Interpenetrating Phase Composite Materials," *Adv. Mater. Technol.*, vol. 2, no. 2, Feb. 2017, doi: 10.1002/admt.201600235.
[38] O. Al-Ketan, M. Adel Assad, and R. K. Abu Al-Rub, "Mechanical properties of periodic interpenetrating phase composites with novel architected microstructures," *Compos. Struct.*, vol. 176, pp. 9–19, Sep. 2017, doi: 10.1016/j.compstruct.2017.05.026.
[39] Torquato S. and Donev A., "Minimal surfaces and multifunctionality," *Proc. R. Soc. Lond. Ser. Math. Phys. Eng. Sci.*, vol. 460, no. 2047, pp. 1849–1856, Jul. 2004, doi: 10.1098/rspa.2003.1269.
[40] S. Torquato, S. Hyun, and A. Donev, "Multifunctional Composites: Optimizing Microstructures for Simultaneous Transport of Heat and Electricity," *Phys. Rev. Lett.*, vol. 89, no. 26, p. 266601, Dec. 2002, doi: 10.1103/PhysRevLett.89.266601.
[41] J. W. Cahn and J. E. Hilliard, "Free Energy of a Nonuniform System. I. Interfacial Free Energy," *J. Chem. Phys.*, vol. 28, no. 2, pp. 258–267, Feb. 1958, doi: 10.1063/1.1744102.
[42] M. Hakamada and M. Mabuchi, "Microstructural evolution in nanoporous gold by thermal and acid treatments," *Mater. Lett.*, vol. 62, no. 3, pp. 483–486, Feb. 2008, doi: 10.1016/j.matlet.2007.05.086.
[43] K. Stratford, R. Adhikari, I. Pagonabarraga, J.-C. Desplat, and M. E. Cates, "Colloidal Jamming at Interfaces: A Route to Fluid-Bicontinuous Gels," *Science*, vol. 309, no. 5744, pp. 2198–2201, Sep. 2005, doi: 10.1126/science.1116589.
[44] M. N. Lee and A. Mohraz, "Bicontinuous Macroporous Materials from Bijel Templates," *Adv. Mater.*, vol. 22, no. 43, pp. 4836–4841, 2010, doi: 10.1002/adma.201001696.
[45] E. Seker, M. L. Reed, and M. R. Begley, "Nanoporous Gold: Fabrication, Characterization, and Applications," *Materials*, vol. 2, no. 4, Art. no. 4, Dec. 2009, doi: 10.3390/ma2042188.
[46] A. Biesiekierski *et al.*, "Extraordinary high strength Ti-Zr-Ta alloys through nanoscaled, dual-cubic spinodal reinforcement," *Acta Biomater.*, vol. 53, pp. 549–558, Apr. 2017, doi: 10.1016/j.actbio.2017.01.085.

[47] F. Findik, “Improvements in spinodal alloys from past to present,” *Mater. Des.*, vol. 42, pp. 131–146, Dec. 2012, doi: 10.1016/j.matdes.2012.05.039.
[48] C. M. Portela *et al.*, “Extreme mechanical resilience of self-assembled nanolabyrinthine materials,” *Proc. Natl. Acad. Sci.*, vol. 117, no. 11, pp. 5686–5693, Mar. 2020, doi: 10.1073/pnas.1916817117.
[49] A. E. Garcia *et al.*, “Scalable synthesis of gyroid-inspired freestanding three-dimensional graphene architectures,” *Nanoscale Adv.*, vol. 1, no. 10, pp. 3870–3882, 2019, doi: 10.1039/C9NA00358D.
[50] J. K. Hohmann, M. Renner, E. H. Waller, and G. von Freymann, “Three-Dimensional µ-Printing: An Enabling Technology,” *Adv. Opt. Mater.*, vol. 3, no. 11, pp. 1488–1507, 2015, doi: 10.1002/adom.201500328.
[51] *Three-Dimensional Microfabrication Using Two-photon Polymerization*. Elsevier, 2016. doi: 10.1016/C2014-0-01016-7.
[52] K.-S. Lee, R. H. Kim, D.-Y. Yang, and S. H. Park, “Advances in 3D nano/microfabrication using two-photon initiated polymerization,” *Prog. Polym. Sci.*, vol. 33, no. 6, pp. 631–681, Jun. 2008, doi: 10.1016/j.progpolymsci.2008.01.001.
[53] M.-T. Hsieh, B. Endo, Y. Zhang, J. Bauer, and L. Valdevit, “The mechanical response of cellular materials with spinodal topologies,” *J. Mech. Phys. Solids*, vol. 125, pp. 401–419, Apr. 2019, doi: 10.1016/j.jmps.2019.01.002.
[54] J. Bauer, A. G. Izard, Y. Zhang, T. Baldacchini, and L. Valdevit, “Programmable Mechanical Properties of Two-Photon Polymerized Materials: From Nanowires to Bulk,” *Adv. Mater. Technol.*, vol. 4, no. 9, p. 1900146, 2019, doi: 10.1002/admt.201900146.
[55] J. Bauer *et al.*, “Thermal post-curing as an efficient strategy to eliminate process parameter sensitivity in the mechanical properties of two-photon polymerized materials,” *Opt. Express*, vol. 28, no. 14, pp. 20362–20371, Jul. 2020, doi: 10.1364/OE.395986.
[56] C. M. Soukoulis and M. Wegener, “Past achievements and future challenges in the development of three-dimensional photonic metamaterials,” *Nat. Photonics*, vol. 5, no. 9, Art. no. 9, Sep. 2011, doi: 10.1038/nphoton.2011.154.
[57] J. Bauer *et al.*, “Additive Manufacturing of Ductile, Ultrastrong Polymer-Derived Nanoceramics,” *Matter*, vol. 1, no. 6, pp. 1547–1556, Dec. 2019, doi: 10.1016/j.matt.2019.09.009.
[58] G. von Freymann *et al.*, “Three-Dimensional Nanostructures for Photonics,” *Adv. Funct. Mater.*, vol. 20, no. 7, pp. 1038–1052, 2010, doi: 10.1002/adfm.200901838.
[59] D. Martella, S. Nocentini, D. Nuzhdin, C. Parmeggiani, and D. S. Wiersma, “Photonic Microhand with Autonomous Action,” *Adv. Mater.*, vol. 29, no. 42, p. 1704047, 2017, doi: 10.1002/adma.201704047.
[60] H. Zeng, P. Wasylczyk, C. Parmeggiani, D. Martella, M. Burresi, and D. S. Wiersma, “Light-Fueled Microscopic Walkers,” *Adv. Mater.*, vol. 27, no. 26, pp. 3883–3887, 2015, doi: 10.1002/adma.201501446.
[61] T.-Y. Huang *et al.*, “3D Printed Microtransporters: Compound Micromachines for Spatiotemporally Controlled Delivery of Therapeutic Agents,” *Adv. Mater.*, vol. 27, no. 42, pp. 6644–6650, 2015, doi: 10.1002/adma.201503095.
[62] S. Tottori, L. Zhang, F. Qiu, K. K. Krawczyk, A. Franco-Obregón, and B. J. Nelson, “Magnetic Helical Micromachines: Fabrication, Controlled Swimming, and Cargo Transport,” *Adv. Mater.*, vol. 24, no. 6, pp. 811–816, 2012, doi: 10.1002/adma.201103818.

[63] A. Marino *et al.*, “A 3D Real-Scale, Biomimetic, and Biohybrid Model of the Blood-Brain Barrier Fabricated through Two-Photon Lithography,” *Small*, vol. 14, no. 6, p. 1702959, 2018, doi: 10.1002/smll.201702959.
[64] F. Klein *et al.*, “Two-Component Polymer Scaffolds for Controlled Three-Dimensional Cell Culture,” *Adv. Mater.*, vol. 23, no. 11, pp. 1341–1345, 2011, doi: 10.1002/adma.201004060.
[65] A. Marino, C. Filippeschi, G. G. Genchi, V. Mattoli, B. Mazzolai, and G. Ciofani, “The Osteoprint: A bioinspired two-photon polymerized 3-D structure for the enhancement of bone-like cell differentiation,” *Acta Biomater.*, vol. 10, no. 10, pp. 4304–4313, Oct. 2014, doi: 10.1016/j.actbio.2014.05.032.
[66] O. Tricinci, T. Terencio, B. Mazzolai, N. M. Pugno, F. Greco, and V. Mattoli, “3D Micropatterned Surface Inspired by Salvinia molesta via Direct Laser Lithography,” *ACS Appl. Mater. Interfaces*, vol. 7, no. 46, pp. 25560–25567, Nov. 2015, doi: 10.1021/acsami.5b07722.
[67] M. Röhrig, M. Thiel, M. Worgull, and H. Hölscher, “3D Direct Laser Writing of Nano- and Microstructured Hierarchical Gecko-Mimicking Surfaces,” *Small*, vol. 8, no. 19, pp. 3009–3015, 2012, doi: 10.1002/smll.201200308.
[68] B.-K. Hsiung *et al.*, “Tarantula-Inspired Noniridescent Photonics with Long-Range Order,” *Adv. Opt. Mater.*, vol. 5, no. 2, p. 1600599, 2017, doi: 10.1002/adom.201600599.
[69] T. Gissibl, S. Thiele, A. Herkommer, and H. Giessen, “Two-photon direct laser writing of ultracompact multi-lens objectives,” *Nat. Photonics*, vol. 10, no. 8, Art. no. 8, Aug. 2016, doi: 10.1038/nphoton.2016.121.
[70] Z. Xie *et al.*, “Demonstration of a 3D Radar-Like SERS Sensor Micro- and Nanofabricated on an Optical Fiber,” *Adv. Opt. Mater.*, vol. 3, no. 9, pp. 1232–1239, 2015, doi: 10.1002/adom.201500041.
[71] M. Malinauskas *et al.*, “Femtosecond laser polymerization of hybrid/integrated micro-optical elements and their characterization,” *J. Opt.*, vol. 12, no. 12, p. 124010, Nov. 2010, doi: 10.1088/2040-8978/12/12/124010.
[72] N. Lindenmann *et al.*, “Photonic wire bonding: a novel concept for chip-scale interconnects,” *Opt. Express*, vol. 20, no. 16, pp. 17667–17677, Jul. 2012, doi: 10.1364/OE.20.017667.
[73] M. Schumann, T. Bückmann, N. Gruhler, M. Wegener, and W. Pernice, “Hybrid 2D–3D optical devices for integrated optics by direct laser writing,” *Light Sci. Appl.*, vol. 3, no. 6, Art. no. 6, Jun. 2014, doi: 10.1038/lsa.2014.56.
[74] Z. Bayindir *et al.*, “Polymer microcantilevers fabricated via multiphoton absorption polymerization,” *Appl. Phys. Lett.*, vol. 86, no. 6, p. 064105, Feb. 2005, doi: 10.1063/1.1863414.
[75] L. J. Jiang *et al.*, “Two-photon polymerization: investigation of chemical and mechanical properties of resins using Raman microspectroscopy,” *Opt. Lett.*, vol. 39, no. 10, pp. 3034–3037, May 2014, doi: 10.1364/OL.39.003034.
[76] S. Nakanishi, S. Shoji, S. Kawata, and H.-B. Sun, “Giant elasticity of photopolymer nanowires,” *Appl. Phys. Lett.*, vol. 91, no. 6, p. 063112, Aug. 2007, doi: 10.1063/1.2767995.
[77] E. D. Lemma *et al.*, “Mechanical Properties Tunability of Three-Dimensional Polymeric Structures in Two-Photon Lithography,” *IEEE Trans. Nanotechnol.*, vol. 16, no. 1, pp. 23–31, Jan. 2017, doi: 10.1109/TNANO.2016.2625820.

[78] J. S. Oakdale, J. Ye, W. L. Smith, and J. Biener, "Post-print UV curing method for improving the mechanical properties of prototypes derived from two-photon lithography," *Opt. Express*, vol. 24, no. 24, pp. 27077–27086, Nov. 2016, doi: 10.1364/OE.24.027077.
[79] L. H. Nguyen, M. Straub, and M. Gu, "Acrylate-Based Photopolymer for Two-Photon Microfabrication and Photonic Applications," *Adv. Funct. Mater.*, vol. 15, no. 2, pp. 209–216, 2005, doi: 10.1002/adfm.200400212.
[80] C. Decker, "Photoinitiated curing of multifunctional monomers," *Acta Polym.*, vol. 45, no. 5, pp. 333–347, 1994, doi: 10.1002/actp.1994.010450501.
[81] W. H. Teh, U. Dürig, U. Drechsler, C. G. Smith, and H.-J. Güntherodt, "Effect of low numerical-aperture femtosecond two-photon absorption on (SU-8) resist for ultrahigh-aspect-ratio microstereolithography," *J. Appl. Phys.*, vol. 97, no. 5, p. 054907, Feb. 2005, doi: 10.1063/1.1856214.
[82] A. Ovsianikov *et al.*, "Laser Photofabrication of Cell-Containing Hydrogel Constructs," *Langmuir*, vol. 30, no. 13, pp. 3787–3794, Apr. 2014, doi: 10.1021/la402346z.
[83] A. Ovsianikov *et al.*, "Ultra-Low Shrinkage Hybrid Photosensitive Material for Two-Photon Polymerization Microfabrication," *ACS Nano*, vol. 2, no. 11, pp. 2257–2262, Nov. 2008, doi: 10.1021/nn800451w.
[84] B. Kaehr *et al.*, "Direct-Write Fabrication of Functional Protein Matrixes Using a Low-Cost Q-Switched Laser," *Anal. Chem.*, vol. 78, no. 9, pp. 3198–3202, May 2006, doi: 10.1021/ac052267s.
[85] C. A. Coenjarts and C. K. Ober, "Two-Photon Three-Dimensional Microfabrication of Poly(Dimethylsiloxane) Elastomers," *Chem. Mater.*, vol. 16, no. 26, pp. 5556–5558, Dec. 2004, doi: 10.1021/cm048717z.
[86] T. Baldacchini *et al.*, "Acrylic-based resin with favorable properties for three-dimensional two-photon polymerization," *J. Appl. Phys.*, vol. 95, no. 11, pp. 6072–6076, May 2004, doi: 10.1063/1.1728296.
[87] C. Quan, M. Soroush, M. C. Grady, J. E. Hansen, and W. J. Simonsick, "High-Temperature Homopolymerization of Ethyl Acrylate and n-Butyl Acrylate: Polymer Characterization," *Macromolecules*, vol. 38, no. 18, pp. 7619–7628, Sep. 2005, doi: 10.1021/ma047528z.
[88] M. C. Grady, W. J. Simonsick, and R. A. Hutchinson, "Studies of higher temperature polymerization of n-butyl methacrylate and n-butyl acrylate," *Macromol. Symp.*, vol. 182, no. 1, pp. 149–168, 2002, doi: 10.1002/1521-3900(200206)182:1<149::AID-MASY149>3.0.CO;2-D.
[89] S. Srinivasan, A. M. Rappe, and M. Soroush, "Chapter 4 - Theoretical Insights Into Thermal Self-Initiation Reactions of Acrylates," in *Computational Quantum Chemistry*, M. Soroush, Ed. Elsevier, 2019, pp. 99–134. doi: 10.1016/B978-0-12-815983-5.00004-0.
[90] M. Schmid, D. Ludescher, and H. Giessen, "Optical properties of photoresists for femtosecond 3D printing: refractive index, extinction, luminescence-dose dependence, aging, heat treatment and comparison between 1-photon and 2-photon exposure," *Opt. Mater. Express*, vol. 9, no. 12, pp. 4564–4577, Dec. 2019, doi: 10.1364/OME.9.004564.
[91] J. W. Hutchinson and J. M. T. Thompson, "Imperfections and energy barriers in shell buckling," *Int. J. Solids Struct.*, vol. 148–149, pp. 157–168, Sep. 2018, doi: 10.1016/j.ijsolstr.2018.01.030.
[92] X. Zheng *et al.*, "Ultralight, ultrastiff mechanical metamaterials," *Science*, vol. 344, no. 6190, pp. 1373–1377, Jun. 2014, doi: 10.1126/science.1252291.

[93] S. C. Han, J. W. Lee, and K. Kang, “A New Type of Low Density Material: Shellular,” *Adv. Mater.*, vol. 27, no. 37, pp. 5506–5511, 2015, doi: 10.1002/adma.201501546.
[94] S. C. Han, J. M. Choi, G. Liu, and K. Kang, “A Microscopic Shell Structure with Schwarz’s D -Surface,” *Sci. Rep.*, vol. 7, no. 1, Art. no. 1, Oct. 2017, doi: 10.1038/s41598-017-13618-3.
[95] M.-T. Hsieh, B. Endo, Y. Zhang, J. Bauer, and L. Valdevit, “The mechanical response of cellular materials with spinodal topologies,” *J. Mech. Phys. Solids*, vol. 125, pp. 401–419, Apr. 2019, doi: 10.1016/j.jmps.2019.01.002.
[96] K. J. Maloney, C. S. Roper, A. J. Jacobsen, W. B. Carter, L. Valdevit, and T. A. Schaedler, “Microlattices as architected thin films: Analysis of mechanical properties and high strain elastic recovery,” *APL Mater.*, vol. 1, no. 2, p. 022106, Aug. 2013, doi: 10.1063/1.4818168.
[97] Y. Li, J. Chen, L. Huang, C. Li, J.-D. Hong, and G. Shi, “Highly Compressible Macroporous Graphene Monoliths via an Improved Hydrothermal Process,” *Adv. Mater.*, vol. 26, no. 28, pp. 4789–4793, 2014, doi: 10.1002/adma.201400657.
[98] A. Nieto, B. Boesl, and A. Agarwal, “Multi-scale intrinsic deformation mechanisms of 3D graphene foam,” *Carbon*, vol. 85, pp. 299–308, Apr. 2015, doi: 10.1016/j.carbon.2015.01.003.
[99] H. Sun, Z. Xu, and C. Gao, “Multifunctional, Ultra-Flyweight, Synergistically Assembled Carbon Aerogels,” *Adv. Mater.*, vol. 25, no. 18, pp. 2554–2560, 2013, doi: 10.1002/adma.201204576.
[100] L. Lv *et al.*, “Solution-Processed Ultraelastic and Strong Air-Bubbled Graphene Foams,” *Small*, vol. 12, no. 24, pp. 3229–3234, 2016, doi: 10.1002/smll.201600509.
[101] A. E. Garcia *et al.*, “Scalable synthesis of gyroid-inspired freestanding three-dimensional graphene architectures,” *Nanoscale Adv.*, vol. 1, no. 10, pp. 3870–3882, Oct. 2019, doi: 10.1039/C9NA00358D.
[102] V. S. Deshpande, N. A. Fleck, and M. F. Ashby, “Effective properties of the octet-truss lattice material,” *J. Mech. Phys. Solids*, vol. 49, no. 8, pp. 1747–1769, Aug. 2001, doi: 10.1016/S0022-5096(01)00010-2.
[103] D. Mohr, “Mechanism-based multi-surface plasticity model for ideal truss lattice materials,” *Int. J. Solids Struct.*, vol. 42, no. 11, pp. 3235–3260, Jun. 2005, doi: 10.1016/j.ijsolstr.2004.10.032.
[104] M. R. O’Masta, L. Dong, L. St-Pierre, H. N. G. Wadley, and V. S. Deshpande, “The fracture toughness of octet-truss lattices,” *J. Mech. Phys. Solids*, vol. 98, pp. 271–289, Jan. 2017, doi: 10.1016/j.jmps.2016.09.009.
[105] X. Zheng, Z. Fu, K. Du, C. Wang, and Y. Yi, “Minimal surface designs for porous materials: from microstructures to mechanical properties,” *J. Mater. Sci.*, vol. 53, no. 14, pp. 10194–10208, Jul. 2018, doi: 10.1007/s10853-018-2285-5.
[106] M.-T. Hsieh and L. Valdevit, “Minisurf – A minimal surface generator for finite element modeling and additive manufacturing,” *Softw. Impacts*, 2020, doi: https://doi.org/10.1016/j.simpa.2020.100026.
[107] D20 Committee, “Test Method for Compressive Properties of Rigid Plastics,” ASTM International. doi: 10.1520/D0695-15.
[108] D. Bell and T. Siegmund, “3D-printed polymers exhibit a strength size effect,” *Addit. Manuf.*, vol. 21, pp. 658–665, May 2018, doi: 10.1016/j.addma.2018.04.013.

[109] L. S. Sutherland and C. Guedes Soares, "The use of quasi-static testing to obtain the low-velocity impact damage resistance of marine GRP laminates," *Compos. Part B Eng.*, vol. 43, no. 3, pp. 1459–1467, Apr. 2012, doi: 10.1016/j.compositesb.2012.01.002.
[110] A. G. Evans, M. Y. He, V. S. Deshpande, J. W. Hutchinson, A. J. Jacobsen, and W. B. Carter, "Concepts for enhanced energy absorption using hollow micro-lattices," *Int. J. Impact Eng.*, vol. 37, no. 9, pp. 947–959, Sep. 2010, doi: 10.1016/j.ijimpeng.2010.03.007.
[111] A. G. Izard, J. Bauer, C. Crook, V. Turlo, and L. Valdevit, "Ultrahigh Energy Absorption Multifunctional Spinodal Nanoarchitectures," *Small*, vol. 15, no. 45, p. 1903834, 2019, doi: 10.1002/smll.201903834.
[112] C. Crook *et al.*, "Plate-nanolattices at the theoretical limit of stiffness and strength," *Nat. Commun.*, vol. 11, no. 1, Art. no. 1, Mar. 2020, doi: 10.1038/s41467-020-15434-2.
[113] J. Bauer *et al.*, "Additive Manufacturing of Ductile, Ultrastrong Polymer-Derived Nanoceramics," *Matter*, vol. 1, no. 6, pp. 1547–1556, Dec. 2019, doi: 10.1016/j.matt.2019.09.009.
[114] Y. Zhang, M.-T. Hsieh, and L. Valdevit, "Mechanical performance of 3D printed interpenetrating phase composites with spinodal topologies," *Compos. Struct.*, vol. 263, p. 113693, May 2021, doi: 10.1016/j.compstruct.2021.113693.
[115] M. Z. Hossain, C.-J. Hsueh, B. Bourdin, and K. Bhattacharya, "Effective toughness of heterogeneous media," *J. Mech. Phys. Solids*, vol. 71, pp. 15–32, Nov. 2014, doi: 10.1016/j.jmps.2014.06.002.
[116] O. Kolednik, J. Predan, F. D. Fischer, and P. Fratzl, "Improvements of strength and fracture resistance by spatial material property variations," *Acta Mater.*, vol. 68, pp. 279–294, Apr. 2014, doi: 10.1016/j.actamat.2014.01.034.
[117] R. Daniel *et al.*, "Fracture toughness enhancement of brittle nanostructured materials by spatial heterogeneity: A micromechanical proof for CrN/Cr and TiN/SiOx multilayers," *Mater. Des.*, vol. 104, pp. 227–234, Aug. 2016, doi: 10.1016/j.matdes.2016.05.029.
[118] Z. Jia and L. Wang, "3D printing of biomimetic composites with improved fracture toughness," *Acta Mater.*, vol. 173, pp. 61–73, Jul. 2019, doi: 10.1016/j.actamat.2019.04.052.
[119] "ASTM Compass." https://compass.astm.org/EDIT/html_annot.cgi?E1820+20b (accessed Jun. 06, 2021).
[120] M.-T. Hsieh and L. Valdevit, "Update (2.0) to MiniSurf—A minimal surface generator for finite element modeling and additive manufacturing," *Softw. Impacts*, vol. 6, p. 100035, Nov. 2020, doi: 10.1016/j.simpa.2020.100035.
[121] T. Li, Y. Chen, and L. Wang, "Enhanced fracture toughness in architected interpenetrating phase composites by 3D printing," *Compos. Sci. Technol.*, vol. 167, pp. 251–259, Oct. 2018, doi: 10.1016/j.compscitech.2018.08.009.
[122] L. D. Wegner and L. J. Gibson, "The fracture toughness behaviour of interpenetrating phase composites," *Int. J. Mech. Sci.*, vol. 43, no. 8, pp. 1771–1791, Aug. 2001, doi: 10.1016/S0020-7403(01)00016-9.
[123] J. Lemesle, C. Hubert, and M. Bigerelle, "Numerical Study of the Toughness of Complex Metal Matrix Composite Topologies," *Appl. Sci.*, vol. 10, no. 18, Art. no. 18, Jan. 2020, doi: 10.3390/app10186250.
[124] G. S. Jung and M. J. Buehler, "Multiscale Mechanics of Triply Periodic Minimal Surfaces of Three-Dimensional Graphene Foams," *Nano Lett.*, vol. 18, no. 8, pp. 4845–4853, Aug. 2018, doi: 10.1021/acs.nanolett.8b01431.

[125] Z. P. Bazant and J. Planas, *Fracture and Size Effect in Concrete and Other Quasibrittle Materials*. CRC Press, 1997.
[126] Z. Jia and L. Wang, "3D printing of biomimetic composites with improved fracture toughness," *Acta Mater.*, vol. 173, pp. 61–73, Jul. 2019, doi: 10.1016/j.actamat.2019.04.052.
[127] T. Etter, J. Kuebler, T. Frey, P. Schulz, J. F. Löffler, and P. J. Uggowitzer, "Strength and fracture toughness of interpenetrating graphite/aluminium composites produced by the indirect squeeze casting process," *Mater. Sci. Eng. A*, vol. 386, no. 1, pp. 61–67, Nov. 2004, doi: 10.1016/j.msea.2004.06.066.
[128] M. X. Gao, Y. Pan, F. J. Oliveira, J. L. Baptista, and J. M. Vieira, "Interpenetrating microstructure and fracture mechanism of NiAl/TiC composites by pressureless melt infiltration," *Mater. Lett.*, vol. 58, no. 11, pp. 1761–1765, Apr. 2004, doi: 10.1016/j.matlet.2003.10.060.
[129] H. Kashani, Y. Ito, J. Han, P. Liu, and M. Chen, "Extraordinary tensile strength and ductility of scalable nanoporous graphene," *Sci. Adv.*, vol. 5, no. 2, p. eaat6951, Feb. 2019, doi: 10.1126/sciadv.aat6951.
[130] R. M. Hensleigh *et al.*, "Additive manufacturing of complex micro-architected graphene aerogels," *Mater. Horiz.*, vol. 5, no. 6, pp. 1035–1041, Oct. 2018, doi: 10.1039/C8MH00668G.

Appendix A. Generation of spinodal topologies

The generation of spinodal topologies follows an approach discussed in detail in [53], and summarized here for completeness. Spinodal decomposition can be described by the Cahn-Hillard evolution equation [41]:

$$\frac{\partial u}{\partial t} = \Delta[\frac{df(u)}{du} - \theta^2 \Delta u] \quad \text{(A1)}$$

where $u(x,y,z,t)$ is the concentration of the two phases A and B at a coordinate (x,y,z) ($-1 \leq u \leq 1$, with $u = -1$ indicating only phase A, or void space, and $u = 1$ indicating only phase B, or solid material), t is the decomposition time, $f(u) = \frac{1}{4}(u^2 - 1)^2$ is a double-well free energy function, θ is the width of the interface between the two phases and Δ is the Laplacian operator. Equation (S1) is solved numerically with a finite difference scheme over a cubic volume with edge length N = 100, which is discretized into a lattice of mesh size, ℓ=N/100=1. Let u_{ijk}^m denote the discrete value of the phase field variable $u(i,j,k,m\tau)$ at nodal point (i,j,k), with τ the integration time step, chosen to be sufficiently small to achieve convergence (τ =0.005 was used here), and m the time step. After discretization with a finite difference scheme, equation (S1) can be written as:

$$\frac{u_{ijk}^{m+1} - u_{ijk}^m}{\tau} = \Delta[(u_{ijk}^m)^3 - u_{ijk}^m - \theta^2 \Delta u_{ijk}^m] \quad \text{(A2)}$$

where θ is the thickness of the interface between the two phases and Δ is the Laplacian operator. The following boundary conditions are applied to solve equation (S2):

$$u(i,j,k,m\tau) = u(i+L,j,k,m\tau) \quad \text{(A3.1)}$$

$$u(i,j,k,m\tau) = u(i,j+L,k,m\tau) \quad \text{(A3.2)}$$

$u(i,j,k,m\tau)=u(i,j,k+L,m\tau)$ (A3.3)

A randomly generated initial condition, $u(i,j,k,0) = u_0(i,j,k,0) \in [-5,5] \times 10^{-4} \neq 0$, was used as a perturbation to exit unstable equilibium and start the decomposition kinetics. As the solution progresses, the system phase separates at early times, and subsequently continues to coarsen; during the coarsening phase, the curvature of the interface between solid and void decreases and the size of the single-phase domains increases. A cutoff u_c^m is defined to separate phase A from phase B, with the phase at a point (i,j,k) and a time $t = m\tau$ defined as:

$$G_{ijk}^m = H(u_{ijk}^m - u_c^m) \quad \text{(A4)}$$

where $H(\cdot)$ represents the Heaviside function. To achieve a 50% volume fraction (V) of phase A, the cutoff u_c^m is adjusted so that u_{ijk}^m satisfied the distribution given by:

$$G_c^m = \frac{1}{N^3}\Sigma_{i=1}^N\Sigma_{j=1}^N\Sigma_{k=1}^N G_{ijk}^m = \frac{1}{N^3}\Sigma_{i=1}^N\Sigma_{j=1}^N\Sigma_{k=1}^N H\left(u_{ijk}^m - u_c^m\right) = V \quad \text{(A5)}$$

Here the decomposition time that controls the characteristic feature size (λ) has been set to provide λ = 1/3 N.

The spinodal shell topologies are subsequently derived by extracting the surface from spinodal solid cellular topologies with volume fraction, V=50%, resulting in a shell topology with negative Gaussian curvature and near-zero mean curvature throughout the domain. While shell-topologies with non-zero mean curvature can be derived from spinodal solid topologies with $V \neq 50\%$, previous studies have demonstrated that near-zero mean curvature topologies provide the best overall mechanical performance for spinodal shell-based cellular materials [53].

Appendix B. Extraction of fracture toughness

The *J*-integral approach outlined in ASTM E1820, 2013 is employed to evaluate the fracture toughness. At a point corresponding to *v* and *P* on the specimen force versus displacement record, the *J*-integral is calculated at the onset of every unloading cycle (given by the index *i*) performed in the loading regime. The value of *J* at an instant (*i*) in the loading regime is then given by the summation of an elastic component, J_{el}, and a plastic component, J_{pl}, as follows:

$$J_{(i)} = J_{el(i)} + J_{pl(i)} \tag{A6}$$

The elastic component J_{el} follows from

$$J_{el(i)} = K_{(i)}^2 / E_{XX} \tag{A7}$$

where the E_{XX} is the measured value of Young's modulus in the *X* direction. The value of $K_{(i)}$ at each unloading event is given as

$$K_{(i)} = \left[\frac{P_i S}{B W^{3/2}} \right] f(a_i / W) \tag{A8}$$

The calibration factor $f(a_i / W)$ is given by

$$f(a_i / W) = 3\left(\frac{a_i}{W}\right)^{1/2} \frac{[1.99 - \left(\frac{a_i}{W}\right)\left(1 - \frac{a_i}{W}\right)(2.15 - 3.93\frac{a_i}{W} + 2.7\left(\frac{a_i}{W}\right)^2]}{2(1+2\frac{a_i}{W})(1-\frac{a_i}{W})^{3/2}} \tag{A9}$$

where $a_{(i)}$ is the current crack length. This crack length is estimated using the relation

$$a_{(i)} = W(0.999748 - 3.9504u + 2.9821u^2 - 3.21408u^3 + 51.51564u^4 - 113.031u^5)$$

(S10)

where the factor u is related to the compliance via

$$u = 1/[(\frac{BWE_{XX}C_{\delta(i)}}{S/4})^{1/2} + 1]$$

(S11)

where $C_{\delta(i)} = (\frac{d\delta}{dP})_{(i)}$ is the compliance estimated from the crack mouth opening displacement at the onset of unloading.

The plastic component of J is estimated using the deformation J definition via

$$J_{pl(i)} = \left[J_{pl(i-1)} + \left(\frac{\eta_{pl}}{b_{(i-1)}} \right) \left(\frac{A_{pl(i)} - A_{pl(i-1)}}{B} \right) \right] \left[1 - \gamma_{pl} (\frac{a_{(i)} - a_{(i-1)}}{b_{(i-1)}} \right] \quad \text{(A12)}$$

where $\eta_{pl} = 1.9$, $\gamma_{pl} = 0.9$ based on the Eq. A1.8 in ASTM E1820, $b_{(i-1)}$ is the length of the uncracked ligament at the previous unloading event via $b_{(i-1)} = B - a_{(i-1)}$. $A_{pl(i)}$ is the area under the plastic load versus load-line displacement measurement. We estimate $A_{pl(i)}$ using

$$A_{pl(i)} = A_{pl(i-1)} + (P_{(i)} + P_{(i-1)})(v_{pl(i)} - v_{pl(i-1)})/2 \quad \text{(A13)}$$

where $v_{pl(i)} = v_{(i)} - \left(P_{(i)} C_{v(i)} \right)$ is the plastic part of the load-line displacement and $C_{v(i)} = \left(\frac{dv}{dP} \right)_{(i)}$ is the experimental compliance corresponding to the current crack length, $a_{(i)}$.

The fracture toughness at the unloading instant (i), $K_{J(i)}$, is then calculated from the *J*-integral using the relation $K_{J(i)} = (J_{(i)} E_{XX})^{1/2}$.

Here, the fracture toughness at the crack initiation, K_{JIC} is calculated as

$$K_{JIC} = [(\frac{P_0 S}{B W^{3/2}})^2 f^2(a_0 / W) + \frac{\eta_{pl} A_{pl(0)}}{B b_0}]^{1/2} \quad \text{(A14)}$$

where P_0 is the force at the crack initiation and a_0 is the precrack length which is the initial length of the notch.